Title
Dynamics of a Submesoscale Surface Ocean Density Front

Author
Abramczyk, Marshall

Publication Date
2012

Peer reviewed|Thesis/dissertation

UNIVERSITY OF CALIFORNIA

Los Angeles

Dynamics of a Submesoscale Surface Ocean Density Front

A thesis submitted in partial satisfaction

of the requirements for the degree Master of Science

in Atmospheric and Oceanic Sciences

by

Marshall Abramczyk

2013

ABSTRACT OF THE THESIS

Dynamics of a Submesoscale Surface Ocean Density Front

by

Marshall Abramczyk

Master of Science in Atmospheric and Oceanic Sciences

University of California, Los Angeles, 2013

Professor Jochen Stutz, Chair

Small-scale ocean flows have increasingly ageostrophic dynamics that are important for the ocean energy budget and biogeochemical cycles. Numerical models indicate that the ageostrophic flow and vertical velocities associated with frontogenesis are a dominant mechanism of surface to interior ocean material transport. The increasingly unbalanced flow may also provide a pathway to downscale energy from the mesoscale to microscale.

In situ observations of these flows are challenging due to the characteristics of the flow, such as small spatial scales and short lifetimes of hours to days. To observe the physical properties, generation, and evolution of these features, a new experimental method was developed at UCLA that incorporates simultaneous sampling by remote sensing and *in situ* instruments onboard satellites, aircraft, and vessels.

On April 14, 2011, a small-scale frontal feature confined to the upper 10 m of the water column was measured near Catalina Island, California. The front had a maximum horizontal temperature gradient of 0.0031℃ m^{-1} and slope of 0.0146. To our knowledge, this is the first

time such high resolution and comprehensive *in situ* observations have been made of submesoscale features.

The thesis of Marshall Abramczyk is approved.

Burkard Baschek

Curtis Deutsch

Jochen Stutz, Committee Chair

University of California, Los Angeles

2013

TABLE OF CONTENTS

LIST OF FIGURES

LIST OF TABLES

CHAPTER 1

Introduction

Ocean fronts are common features of the global ocean, spanning all length scales from synoptic of *O*(1000) km through the submesoscale of *O*(0.1-10) km at both the surface and ocean interior. Frontal time scales range from years at the larger scales and hours to days at small scales. The shared characteristics of ocean and atmospheric fronts have long been recognized and the current ocean front research owes much to the study of atmospheric fronts [*Hoskins and Bretherton*, 1972; *Hoskins*, 1975; *Hoskins*, 1982].

An ocean front is an area of elevated gradients of hydrographic properties in excess of their respective background gradients [*Federov*, 1987; *Tomczak and Godfrey*, 2003]. Ocean fronts are commonly described by density (ρ), which is a function of salinity(S), temperature (T), and pressure (p) as defined in the equation of state (eq. 1.1) [*Stewart*, 2008].

$$\rho = \rho(S, T, p) \tag{1.1}$$

With respect to density, two distinct types of fronts exist; (1) density fronts and (2) density-compensated fronts [*Federov*, 1987; *Tomczak and Godfrey*, 2003]. Density fronts have horizontal density gradients with vertically tilted isopycnals that intersect a horizontal reference line. The frontal interface at the maximum of the horizontal density gradient separates dense and light water. With density compensated fronts, the across-front changes in salinity and temperature have opposite contributions to density, resulting in no horizontal density gradient while independent, horizontal gradients in salinity and temperature are maintained [*Tomczak and Godfrey*, 2003].

This thesis focuses on density fronts at the surface ocean with distinct sea surface temperature (SST) gradients (temperature as a proxy for density). With density fronts, the along-front direction is defined as normal to the horizontal density gradient with length scales comparable to the mode dependent deformation radius. The across-front direction is parallel to the horizontal density gradient with scales smaller than the corresponding deformation radius of the along-front direction [*Hoskins and Bretherton*, 1972]. At density fronts, there exist across-front changes in stratification, vorticity, buoyancy, and vertical velocity [*Hoskins and Bretherton*, 1972; *Spall*, 1995]. A detailed description of front length scales and circulation follows in sections 1.1-1.3 and 2.

The surface mixed layer is strongly influenced by atmospheric forcings, such as wind and surface heating/cooling that alter the stratification of the surface ocean. Wind forced mixing homogenizes the surface mixed layer and decreases the stratification, leading to a deepening of the mixed layer. This forcing is responsible for the introduction and spatial redistribution of both momentum and material in the mixed layer [*Spall*, 1995; *Klein and Lapeyre*, 2009].

Modeling and observational evidence support that surface density fronts, or features with horizontal density gradients (ex. circular eddies, or filaments) are also capable of modulating the surface mixed layer and causing mixing across the seasonal thermocline in the absence of atmospheric forcing [model studies: *Bleck et al*., 1988; *Spall*, 1995; *Haine and Marshall*, 1998; *Mahadevan and Archer* 2000; *Lévy et al*., 2001; *Lapeyre and Klein* 2006a-b; *Capet et al*., 2008; *Capet et al*., 2008a-c; *Klein et al*., 2008; *in situ* observations: *Pollard and Regier*, 1990; *Pollard and Regier*, 1992; *McGillicuddy et al.*, 2007]. With the exclusion of wintertime convection, the primary mechanism of mixing between the surface and interior ocean at density features is frontogenesis [*Spall*, 1995; *Lapeyre and Klein*, 2006a; *Capet et al*., 2008b]. Frontogenesis

(section 2) occurs when a larger scale strain field strengthens the horizontal density gradient causing an ageostrophic circulation with vertical velocities to develop [*Hoskins and Bretherton*, 1972; *Hoskins*, 1975; *Hoskins*, 1982]. The vertical velocities from frontogenesis at mesoscale and submesoscale density features are an order of magnitude larger than those from wind forcing (Ekman pumping), thereby contributing more to the flux of material from the surface to interior ocean [*Bleck et al*., 1988; *Haine and Marshall*, 1998; *Spall*, 1995; *Mahadevan and Archer*, 2000; *Klein and Lapeyre*, 2009].

The vertical redistribution of tracers, gases, and nutrients has important implications for processes such as weather forecasting with coupled atmosphere-ocean global climate models, carbon/aerosol sequestration, and nutrient introduction to the euphotic zone [*Spall*, 1995; *Mahadevan and Archer*, 2000; *Lévy et al*., 2001; *Lapeyre and Klein*, 2006b*; McGillicuddy et al*., 2007]. Although fronts are localized regions of enhanced vertical velocities and ocean mixing, their ubiquitous nature lends credence to their large cumulative contribution of vertical material exchange and modulation of the surface ocean [*Klein and Lapeyre*, 2009].

Mesoscale circulations of *O*(20-100) km are well documented by numerical models and *in situ* observations, resulting in comprehensive knowledge of their contributions to ocean dynamics and tracer/material redistribution [*Pollard and Regier*, 1990; *Pollard and Regier*, 1992; *Spall*, 1995*; McGillicuddy et al*., 2007]. Recent studies also indicate that submesoscale flows of *O*(0.1-10) km (microscale < submesoscale < mesoscale) may also provide substantial and key contributions to ocean dynamics due to their intermediary scale that combines properties of the mesoscale and microscale [*Lévy et al*., 2001; *Muller et al*., 2005; *Lapeyre and Klein*, 2006a-b; *Mahadevan and Tandon*, 2006; *Capet et al*., 2008a-c; *Klein et al*., 2008; *Le Traon et al*., 2008; *Klein and Lapeyre*, 2009; *McWilliams*, 2010]. *In situ* observations of submesoscale

features lag that of mesoscale features due to encumbering characteristics of the submesoscale, including small scales, short lifetimes, and advection by mesoscale features [*Mahadevan and Tandon*, 2006; *Capet et al*., 2008a-c; *Klein and Lapeyre*, 2009]. Further observations are required to determine the overall impact/influence of submesoscale dynamics on the global ocean and atmosphere.

To overcome the challenges in observing submesoscale flows, a multi-faceted experiment method was devised at the University of California at Los Angeles (UCLA) that includes aerial remote sensing and *in situ* platforms capable of making high spatial-temporal resolution measurements. The experimental method is a new frontier for submesoscale observations that is designed to provide valuable insight into physical properties and the dynamics that govern the generation and evolution of a submesoscale feature. The experimental method detailed in this thesis is the first iteration of a developing method that is the cumulative result of many scientists and long-term preparation. It will become apparent during the analysis that submesoscale circulation is difficult to extract from the data. Accordingly, the focus will be on the assessment of the method and suggestions for improvement. More insight into submesoscale dynamics will follow as the experimental method is refined.

Section 1.1 is an introduction to mesoscale features that have flows characteristic of balanced dynamics. This will provide a general foundation for the submesoscale that exhibits some degree of balanced dynamics and a reference point for any departure from balanced dynamics. Section 1.2 introduces the submesoscale and section 1.3 discusses submesoscale relevance for the ocean energy budget and nutrient injection. Section 1.3 alludes to the importance of frontogenesis, the dynamics of which are addressed in section 2. Section 3 describes internal

gravity waves commonly observed during *in situ* observations that are a strong signal in our measurements. The remaining sections detail the submesoscale experiment conducted by UCLA and supporting agencies with experimental methods, results, and conclusions in sections 4, 5, and 6 respectively.

1.1 The Mesoscale

Mesoscale features have horizontal length scales given by the first baroclinic deformation radius, commonly referred to as the internal deformation radius (R_i, eq. 1.4 at mode *n=1*) [*McWilliams*, 2006]. The general deformation radius equation (eq. 1.2) equals the gravity wave speed (c_n) at mode *n* divided by the Coriolis frequency (*f*). At mode 1, the gravity wave speed (eq. 1.3) is given by the Brunt Väisälä frequency (*N*) and the scale height of the flow (*H*). The deformation radius is then equation 1.4

$$R_n = \frac{c_n}{f} \tag{1.2}$$

$$c_1 = NH \tag{1.3}$$

$$R_i = \frac{NH}{f} \tag{1.4}$$

The baroclinic deformation radius specifies when rotational effects are as important as buoyancy effects. R_i is of O(20-100) km for a midlatitude (45°N) mesoscale front with $N \approx 0.02$ s^{-1}, H of O(1000-5000) m, and $f \approx 10^{-4}$ s^{-1}. Characteristic horizontal velocities are of O(0.1) m s^{-1} and vertical velocities of $O(10^{-5}\text{-}10^{-4})$ m s^{-1} [*Thomas et al*., 2008]. Due to the large horizontal to vertical scale ratio and weak vertical velocities, mesoscale fronts behave as anisotropic, two dimensional (2D) flows [*Muller et al*., 2005]. Due to their anisotropic nature, mesoscale features

are generally considered barotropic (i.e. no vertical velocity shear) and each fluid layer is treated independently [*Thomas et al*., 2008].

Quasigeostrophic theory (QG) as detailed by Pedlosky (1987) adequately describes the large scale and slow dynamics ($\frac{mesoscale\ frequency}{f} \rightarrow 0$) of mesoscale flows [*Pedlosky*, 1987; *McWilliams*, 2006]. For QG theory to be applicable, the flow must have small Rossby (*Ro*, eq. 1.5) and Froude (*Fr*, eq. 1.6) numbers (*Ro* and $Fr \ll 1$).

$$Ro = \frac{|\mathbf{u} \cdot \boldsymbol{\nabla}\mathbf{u}|}{\left|f\hat{\mathbf{k}} \times \mathbf{u}\right|} \tag{1.5}$$

$$Fr = \frac{V}{NH} \tag{1.6}$$

The Rossby number defines the relative importance of the advection of velocity ($\boldsymbol{u}$), $|\mathbf{u} \cdot \boldsymbol{\nabla}\mathbf{u}|$, to the strength of the Coriolis force, $\left|f\hat{\mathbf{k}} \times \mathbf{u}\right|$. At low values, the Coriolis force is dominant, but at larger *Ro* values, the advective forces (nonlinear) become more significant. Following the $Ro \rightarrow 0$ limit, the inertial and nonlinear terms of the non-dimensionalized Navier Stokes momentum equation (eq. 1.7) are neglected [*McWilliams*, 2006].

$$\epsilon \frac{D\mathbf{u}}{Dt} + f\hat{\mathbf{z}} \times \mathbf{u} = -\boldsymbol{\nabla}p + \epsilon\mathbf{F} \tag{1.7}$$

In equation 1.7, $\epsilon = Ro$, $\frac{D\mathbf{u}}{Dt}$ is the full time derivative ($\frac{D}{Dt} = \frac{\partial}{\partial t} + \mathbf{u} \cdot \boldsymbol{\nabla}$) of horizontal velocity, $f\hat{\mathbf{z}} \times \mathbf{u}$ is the Coriolis force**,** $\boldsymbol{\nabla}p$ is the pressure gradient, and **F** represents all nonlinear forces [*McWilliams*, 2006]**.** At small *Ro*, the Coriolis force is balanced by the pressure gradient force and the flow is termed geostrophically balanced.

The Froude number (eq. 1.6) is given by the horizontal velocity (*V*), buoyancy frequency (*N*), and depth of the flow (*H*). The Froude number describes the rate of the horizontal velocity to the speed of a gravity wave - i.e. the relative strengths of inertial to gravitational forces respectively. At low values the fluid is hydrostatically balanced in the vertical, with stronger stratification and resistance to vertical perturbations. In hydrostatic balance (eq. 1.8), the column weight of water (ρg) is balanced by the vertical pressure difference ($\frac{\partial p}{\partial z}$).

$$\frac{\partial p}{\partial z} + \rho g = 0 \tag{1.8}$$

Ro is approximated (eq. 1.9) as

$$Ro \sim \frac{VV/L}{2\Omega V} = \frac{V}{2\Omega L} \tag{1.9}$$

where *V* is the horizontal velocity, $f = 2\Omega$ is the Coriolis frequency (Ω = rate of earth's rotation [2π rad d^{-1}] ≈ 0.73 x 10^{-4} s^{-1}), and *L* is the length scale of the flow. With a horizontal velocity of ≤ 0.5 m s^{-1}, Coriolis frequency of $O(10^{-4})$ s^{-1}, and an internal deformation radius of *O*(20-100) km, *Ro* is then ≤ 0.1 and *Fr* is ≈ 0.01 (*H* = 1000 M). The QG approximations of geostrophic balance in the horizontal and hydrostatic balance in the vertical are then valid for mesoscale flows in the limit that $Ro, Fr \rightarrow 0$ [*McWilliams*, 2006].

The geostrophic zonal and meridional component velocities (hereinafter denoted by subscript g), u_g and v_g respectively, of the QG momentum equation (eq. 1.7) reduce to

$$u_g = -\frac{1}{\rho f}\frac{\partial p}{\partial y} \tag{1.10}$$

$$v_g = \frac{1}{\rho f}\frac{\partial p}{\partial x} \tag{1.11}$$

The component horizontal geostrophic velocities are proportional to the strength of the horizontal gradient of pressure, $\frac{\partial p}{\partial x}$ and $\frac{\partial p}{\partial y}$. To express equation 1.10 and 1.11 in terms of density, hydrostatic balance (eq. 1.8) and the incompressibility of seawater (eq. 1.12) are assumed.

$$\rho = \rho_0 + \delta\rho \text{ where } \frac{\delta\rho}{\rho_0} \ll 1 \tag{1.12}$$

From equation 1.12, the density change ($\delta\rho$) about the reference density (ρ_0) is assumed to be small ($\frac{\delta\rho}{\rho_0} \ll 1$). Allowing for vertical velocity shear in the first mode of the deformation radius equation, taking the vertical derivative ($\frac{\partial}{\partial z}$) of the u_g and v_g momentum equations (eq 1.10 and 1.11) results in more general thermal wind balance equations (eq. 1.13 and 1.14) [*Stewart*, 2008].

$$\frac{\partial u_g}{\partial z} = \frac{g}{f\rho_0}\frac{\partial \rho}{\partial y} \tag{1.13}$$

$$\frac{\partial v_g}{\partial z} = -\frac{g}{f\rho_0}\frac{\partial \rho}{\partial x} \tag{1.14}$$

At a front with sloping isopycnals and a decreasing horizontal density gradient away from the frontal interface ($\frac{\partial \rho}{\partial x}$ or $\frac{\partial \rho}{\partial y} < 0$), there is an along-front jet at the maximum of the horizontal density gradient that increases in strength towards the surface from a subsurface level of no motion (fig. 1.1). Dense water is to the left of the surface current direction of motion [*Hoskins and Bretherton*, 1972; *Hoskins*, 1975; *Hoskins*, 1982].

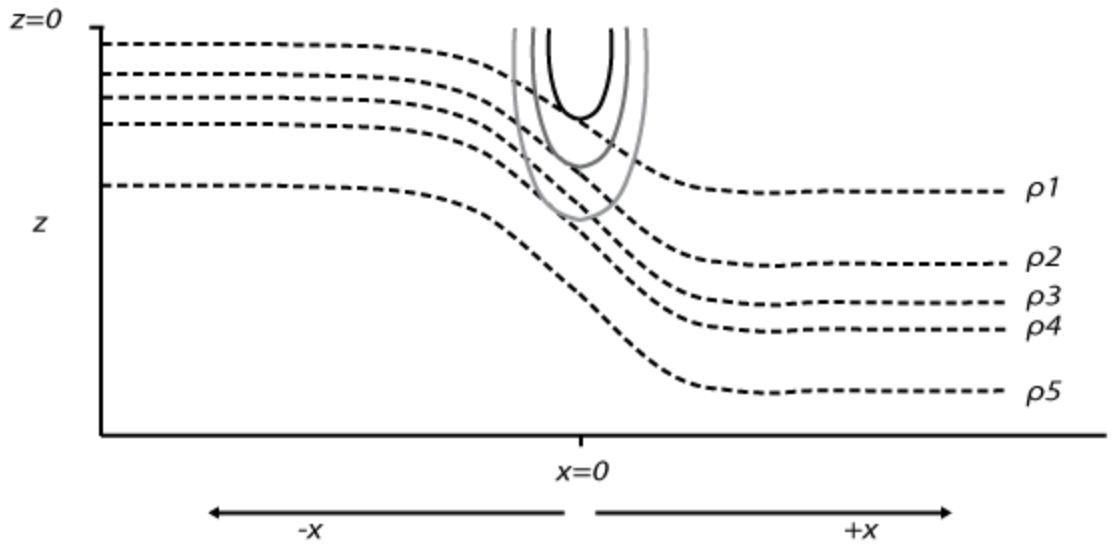

Figure 1.1: Surface density front with geostrophic jet. The dashed lines are isopycnals where $\rho 5 > \rho 4 > \rho 3 > \rho 2 > \rho 1$. The geostrophic jet is shown by the grey - black solid lines, where darker shades of grey (to black) are increasing jet strength. The geostrophic jet is directed into the page with dense water to the left of the jet direction of motion following thermal wind balance (eq. 1.13 and 1.14).

It is known that QG theory provides robust descriptions of flows satisfying small *Ro* and *Fr* limits, but often QG theory qualitatively describes flows where *Ro* and *Fr* are large [*Hoskins*, 1975; *Hoskins*, 1982]. Since the submesoscale often has a significant degree of geostrophic and hydrostatic balance, the dynamics here will be relevant for comparisons between the mesoscale and submesoscale flows. Mesoscale observations and QG theory also provide *a priori* knowledge of frontal dynamics and are fundamental in the design of the experiment method. The equations detailed here will be used in the consequent analysis of a submesoscale front.

1.2 The Submesoscale

Submesoscale flows have horizontal scales less than the first baroclinic deformation radius of the mesoscale with lengths of O(0.1-10) km and vertical scales of O(10) m. Submesoscale flows have time scales ranging from hours to days and are advected by mesoscale feature horizontal

velocities [*Capet et al*., 2008a]. Submesoscale and smaller scale flows are increasingly direction independent (isotropic in 3 dimensional (3D) space), though not fully 3D flows [*Muller et al*., 2005]. Vertical velocities of $O(10^{-3})$ m s^{-1} are an order of magnitude larger than those for mesoscale flows [*Thomas et al*., 2008].

A primary generation mechanism of submesoscale features is straining by mesoscale deformation fields that induce frontogenesis (section 2), creating sharp density fronts [*Capet et al*., 2008b-c]. Frontogenesis supplies the submesoscale with energy by converting mesoscale potential energy to submesoscale kinetic energy (KE) through buoyancy flux [*Capet et al*., 2008b-c]. Other mechanisms such as mixed layer instabilities and reverse energy cascades from turbulence also exist [*McWilliams and Molemaker*, 2004; *Muller et al*., 2005; *Thomas et al*., 2008*; McWilliams*, 2010].

The submesoscale regime serves as an intermediary between the balanced dynamics of the mesoscale and 3D turbulence of the microscale [*McWilliams*, 2010]. Rotational and stratification effects are still important at the submesoscale, but as *Ro* and *Fr* approach unity or greater due to the smaller scales and often sharper density gradients, the nonlinear terms neglected at the mesoscale must be incorporated to adequately describe dynamics [*McWilliams*, 2010]. In a departure from geostrophic balance, flow is increasingly ageostrophic (hereinafter denoted with subscript a). Even weak ageostrophic flow is shown to develop different circulation patterns and consequences for ocean dynamics at the submesoscale (detailed in section 1.3 and 2) [*Wang*, 1993; *Capet et al*., 2008b]. To what extent submesoscale flows depart from balanced dynamics and their contribution to ocean circulation is an open question that the submesoscale *in situ* experiments hope to address.

1.3 Why The Submesoscale

Past modeling and observational studies have adopted a long standing mesoscale-centric approach. This approach is the result of two primary influences:

1. Mesoscale flows (particularly eddies) represent a dominant portion of the ocean energy [*Capet et al*., 2008a]. Low resolution models supported vertical velocities at the center of mesoscale flows and not along submesoscale extensions that are subgrid [*McGillicuddy et al*., 2007; *Capet et al*., 2008a-c; *Klein and Lapeyre*, 2009]. Consequently, submesoscale filaments, eddies, and fronts were considered passive features resulting from mesoscale straining/mixing with little energy and no dynamics (ex. no vertical velocities) [*Klein and Lapeyre*, 2009; *McWilliams*, 2010].
2. The length and time scales of submesoscale features are inhibitive to observations. Submesoscale features are generally subgrid scales for remote sensing satellites and common *in situ* research platforms, such as drifters, floats, and large research vessels. This favored mesoscale observations [*Mahadevan and Tandon*, 2006].

The combination of factors 1 and 2 have contributed to a presently under sampled submesoscale regime with respect to *in situ* measurements [*Mahadevan and Tandon*, 2006; *Klein and Lapeyre*, 2009].

Recently, there have been several numerical modeling studies from an ocean energy and biology viewpoint that employ high resolution domains and mathematical schemes capable of resolving intricate 3D flows at all wavenumbers of the submesoscale [energy: *McWilliams and Molemaker*, 2004; *Muller et al*., 2005; *Capet et al*., 2008; *Capet et al*. 2008a-c; biology: *Mahadevan and Archer*, 2000; L*évy et al*., 2001; *Lapeyre and Klein*, 2006a-b; *Mahadevan and*

Tandon, 2006; *Nagai et al*. 2006; Kle*in et al*., 2008; *Klein and Lapeyre*, 2009]. The investigations indicate that the submesoscale is in fact a dynamically relevant scale with strong vertical velocities that significantly affect the incomplete energy and nutrient budgets.

1.3.1 Energy Viewpoint

Mesoscale flows represent a dominant portion of the ocean energy because the energy transmitted to ocean flows by atmospheric forcings is accumulated at the first baroclinic deformation radius [*Capet et al*., 2008c; *McWilliams*, 2010]. QG dynamics of mesoscale flows does not support a further downscale of energy to dissipation at microscales [*McWilliams*, 2010]. An analysis of the horizontal wave number spectra of mesoscale flows shows a spectral slope of -3 for KE and potential enstrophy, which is congruent with geostrophic turbulence values established by Charney in QG theory [*Charney*, 1971; *Capet et al*., 2008c]. The -3 spectral slopes dictate an inverse cascade of KE accumulated at the mesoscale to larger scales, and a forward enstrophy cascade to smaller scales [*Charney*, 1971; *Capet et al*., 2008c; *Klein et al*., 2008]. The unknown mechanism to downscale KE to dissipation at 3D turbulence scales presents a gap of several orders of magnitude in which the energy conversion is poorly understood [*McWilliams*, 2010].

Through the aforementioned modeling studies is evidence being gathered that the submesoscale may provide the missing link in the downscale of energy [*Capet et al*., 2008a-c; *Klein et al*., 2008]. Increasing domain resolution has shown an increase in KE at submesoscale wavenumbers with no mesoscale KE increase, substantiating an energetic submesoscale regime [*Capet et al*., 2008c; *Klein et al*., 2008]. The modeling studies also show a shallowing of the KE slope to -2 [*Capet et al*., 2008a; *McWilliams*, 2010]. The departure of the KE spectrum from

established geostrophic turbulence values is further supported by satellite observations with increased image resolutions [*Le Traon et al*., 2008]. The forward energy cascade is attributed to ageostrophic dynamics that are weak, albeit essential to the forward flux [*Capet et al*., 2008c].

1.3.2 Biology Viewpoint

Previous estimates of nutrients supplied to the euphotic zone attributed to winter time convection underestimated observed levels of new production by half [*McGillicuddy et al.*, 2003; *McGillicuddy et al.*, 2007]. Mesoscale eddy resolving models led to a significant increase in nutrient injection, but did not complete the budget [*McGillicuddy et al.*, 2003; *McGillicuddy et al.*, 2007]. Lévy et al. (2001) and Mahadevan et al. (2000) found that higher resolution models led to an increase in nutrient injection due to the inclusion of submesoscale features and their associated vertical velocities that were previously not resolved [*Mahadevan and Archer*, 2000; *Lévy et al*., 2001]. They concluded that the high surface variability of tracers (nutrients and temperature/density) is not the result of mesoscale stirring creating submesoscale size features with no dynamics (as in point 1 above), but rather, submesoscale size surface variability results from vertical velocities associated with the submesoscale features [*Mahadevan and Archer*, 2000; *Lévy et al*., 2001; *Glover et al*., 2008].

Lapeyre and Klein (2006b) confirm the increased nutrient flux, noting that submesoscale features (filaments in their studies) represented weaker density and temperature anomalies, but had significant vertical contributions of tracers (nutrients) to the surface ocean [*Lapeyre and Klein*, 2006b]. The flux was strongly positive for nutrient injection and weak for removal due to the large vertical gradient where the interior ocean nutrient concentrations are high and the surface concentrations are near zero [*Lapeyre and Klein*, 2006b]. Material with zero

concentration (at the surface) cannot be transported to create negative concentrations [*Lapeyre and Klein*, 2006b]

The vertical velocities at submesoscale features are attributed to frontogenesis [*Mahadevan and Archer*, 2000; *Lévy et al*., 2001; *Lapeyre and Klein*, 2006b]. The nutrient injection estimates from submesoscale features doubled the total nutrient injection to the surface (with respect to nitrate) and may close the nutrient budget [Lape*yre and Klein*, 2006b].

The energy and biology studies all bypass the previous notions that only mesoscale features are capable of energy exchange and the vertical transport of material. The studies indicate that submesoscale features on the edge of mesoscale features have larger, albeit more concentrated vertical velocities even if the flows themselves may be less energetic, or have weaker temperature (density) gradients [*Lapeyre and Klein*, 2006b]. Furthermore, submesoscale dynamics are dominant in the surface region, whereas, mesoscale dynamics are dominant in the ocean interior [*Capet et al*., 2008; *Klein et al*., 2008]. This is important for the aforementioned contributions to air-sea gas exchange, weather forecasting, and nutrient injection, all of which require the air-sea interface and/or shallow depths (euphotic zone). The studies also point to frontogenesis and ageostrophic circulation as contributing to the vertical exchange of material and conversion of energy [*Lévy et al*., 2001; *Lapeyre and Klein* 2006a-b; *Mahadevan and Tandon*, 2006; *Capet et al*., 2008; *Capet et al*., 2008a-c]. They further note the lack of *in situ* measurements resulting from the past mesoscale-centric paradigm and support the need for high resolution observational studies [*Lévy et al*., 2001; *Lapeyre and Klein* 2006a-b; *Mahadevan and Tandon*, 2006; *Klein and Lapeyre*, 2009].

CHAPTER 2

Frontogenesis

As previously discussed, the main mechanism responsible for the modulation of the surface mixed layer and vertical material/buoyancy redistribution is frontogenesis.

A submesoscale feature in the presence of a barotropic, mesoscale deformation field will experience a strengthening of the horizontal density gradient [*Hoskins and Bretherton*, 1972; *Hoskins*, 1975; *Hoskins*, 1982]. This occurs due to the horizontal strain (eq. 2.1) of the deformation field that acts to deform the initial shape of a parcel independent of a volume change [*McWilliams*, 2006].

$$S = \sqrt{\left(u_x - v_y\right)^2 + \left(v_x - u_y\right)^2} \tag{2.1}$$

The strain rate is given by the derivatives with respect to x and y (subscript *x* and *y*) of the zonal and meridional velocity components, *u* and *v* respectively [*McWilliams*, 2006].

The barotropic nature (depth independent) of the deformation field does not increase the vertical velocity shear and the thermal wind balance of the front is disrupted (eq. 1.13 and 1.14) [*Hoskins and Bretherton*, 1972]. To restore geostrophic balance, a secondary ageostrophic circulation develops that decreases the horizontal density gradient (decreases the buoyancy gradient) and increases the vertical velocity shear [*Hoskins and Bretherton*, 1972; *Hoskins*, 1982].

$$\frac{Dv_g}{Dt} + fu_a = 0 \tag{2.2}$$

The acceleration of the along-front flow (which increases shear) is proportional to the across-front ageostrophic flow (eq.2.2). $\frac{Dv_g}{Dt}$ is the full time derivative of the along-front geostrophic velocity (v_g) that includes ageostrophic across-front (u_a) and vertical (w_a) components (eq 2.3) due to *Ro* ≥ 1 of submesoscale flows [*Hoskins*, 1982; *McWilliams*, 2006].

$$\frac{D}{Dt} = \frac{\partial}{\partial t} + v \cdot \nabla = \frac{\partial}{dt} + u_a \frac{\partial}{\partial x} + v_g \frac{\partial}{\partial y} + w_a \frac{\partial}{\partial z} \tag{2.3}$$

Following a parcel embedded in the deformation field as it moves towards the frontal interface, the parcel encounters an increase (dense side) or decrease (light side) in absolute vorticity due to the addition of positive (dense side), or negative (light side) relative vorticity associated with the frontal jet (fig. 2.1A, B) [*Hoskins and Bretherton*, 1972; *Hoskins*, 1975; *Hoskins*, 1982; *Pollard and Regier*, 1992; *Spall*, 1995]. To conserve potential vorticity (eq. 2.4) the thickness of the isopycnals must change.

$$\frac{dq}{dt} = \frac{d}{dt}\left(\frac{f + \zeta}{h}\right) = 0 \tag{2.4}$$

The potential vorticity (q) is given by the planetary and relative vorticity, f and ζ respectively, and the isopycnal thickness (h) [*Spall*, 1995]. On the dense side, the isopycnal spacing increases to account for the addition of positive absolute vorticity (absolute vorticity is $f + \zeta$), resulting in downwelling (fig. 2.1C, D). On the light side of the front, isopycnal spacing decreases as the absolute vorticity is reduced, resulting in upwelling (fig. 2.1C, D).

Since w ≅ 0 at the surface, a surface flow from light to dense and a subsurface flow from dense to light results to conserve mass balance (fig 2.1C) [*Hoskins and Bretherton*, 1972; *Pollard and Regier*, 1992; *Spall*, 1995]. The ageostrophic surface circulation from light to dense

is in the negative direction, so the along-front geostrophic jet increases in accordance with equation 2.2. The subsurface ageostrophic circulation from dense to light is in the positive direction, thereby decreasing the jet strength (eq. 2.2).

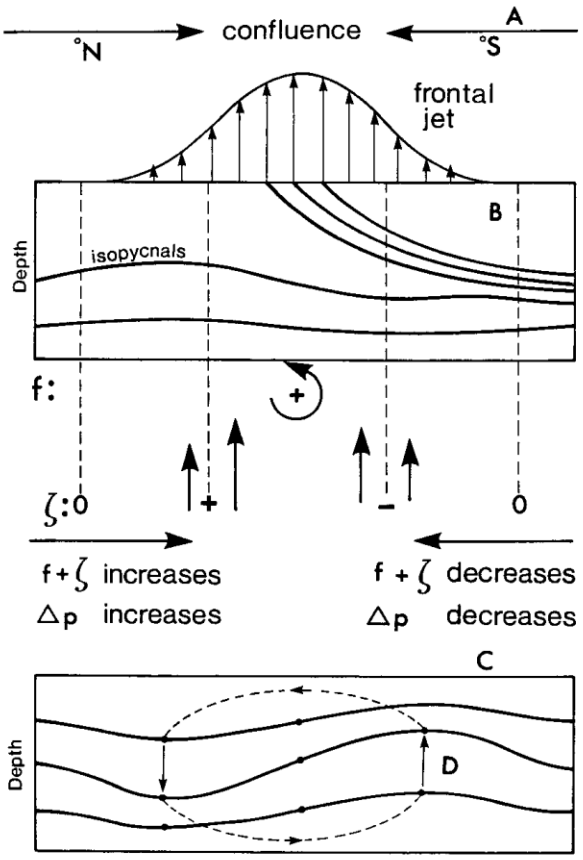

Figure 2.1: Density front (B) in the presence of a confluent deformation field (A). The absolute vorticity changes (B) as a parcel moves into the frontal jet. To conserve potential vorticity, an ageostrophic secondary circulation results (C, D). Image from Pollard and Regier 1992 – Vorticity and vertical circulation at an ocean front.

Converting the left hand side of the thermal wind equations (eq. 1.13 and 1.14) to buoyancy (*b*),

$$b = -\frac{\rho'}{\rho_o} g \tag{2.5}$$

where ρ' is the density anomaly from the reference density (ρ_o), there is a buoyancy gradient ($\frac{db}{dx}$) pointing to the warm side. Downward velocities on the dense side and upwelling on the light side decreases the gradient strength – the restratification effect [*Hoskins*, 1982].

However, the rate of restratification is slower than the intensification of the horizontal density gradient. The convergence of the deformation field and ageostrophic circulation from light to dense side strengthens the horizontal density gradient, producing a sharp front on the cold side (frontogenesis), while a divergent surface flow on the warm side produces a broader front [*Spall*, 1995].

In the submesoscale regime, the departure from balance results in asymmetrical vortices with a dominant cyclonic structure that arises due to stronger ageostrophic circulation [*Hoskins*, 1975; *Hoskins*, 1982; *Wang*, 1993; *Spall*, 1995; *McWilliams and Molemaker*, 2004; *Mahadevan and Tandon* 2006]. The vertical velocities are proportional to the deformation rate and have maximum velocities subsurface (w ≅ 0 at the surface) [*Wang*, 1993; *Lapeyre and Klein*, 2006a; *Capet et al*., 2008a; *Thomas et al*., 2008]. Vertical velocities on the cold side are concentrated and intense, with values approaching 100 m day^{-1} [*Wang*, 1993].

In comparison, mesoscale features have broader regions of downwelling with smaller vertical velocities [*Spall*, 1995] Following the QG limit as $Ro \to 0$, mesoscale features are also axisymmetric [*McWilliams*, 2006]. QG dynamics does not predict vertical velocities because it does not include ageostrophic circulation [*McWilliams*, 2006].

CHAPTER 3

Internal Gravity Waves

Internal gravity waves are common phenomena observed during *in situ* measurements [*Pollard and Regier*, 1992]. The distortion of vertical density distribution by internal gravity waves constitutes a signal that must be removed for accurate calculations of dynamics independent of the waves. This is true for calculating subsurface geostrophic velocities based on the integration of the vertical shear of horizontal velocity derived from the horizontal density field (eq. 1.13 and 1.14).

Mesoscale *in situ* studies remove internal gravity wave distortions with low pass filters because the mesoscale features are spatially larger and evolve on slower time scales than the internal gravity wave motions (except for tidal frequencies) [*Pollard and Regier*, 1992]. Since submesoscale dynamics evolve on similar time scales to internal gravity waves, they now share a frequency band. Smoothing on the order of kilometers as done in mesoscale observations is impractical for submesoscale features that are of comparable length scales to the smoothing kernel width. The amount of horizontal smoothing must decrease, essentially increasing the filter pass bandwidth and reducing the filtering of internal gravity waves. Unavoidably, filtering of internal gravity waves reduces the strength of submesoscale dynamics that are evolving on a comparable time scale.

Internal gravity waves exist in a stably stratified ocean and propagate along interfaces between two fluid layers of different density.

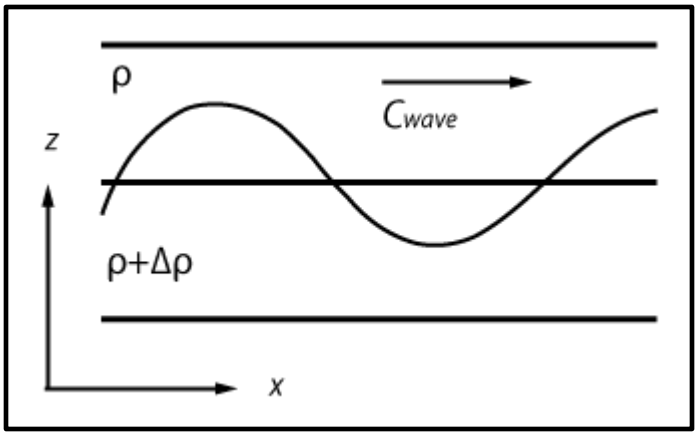

Figure 3.1: Propagation of an internal gravity wave along the interface between two fluids of different density, $\boldsymbol{\rho}$ and $\boldsymbol{\rho} + \Delta\boldsymbol{\rho}$. $\Delta\boldsymbol{\rho}$ is the change in density between depths (*z*). The x axis is parallel to the isopycnals. *Cwave* is the propagation velocity and direction of the wave.

If a parcel at rest is vertically displaced in an adiabatic manner to a new depth, then the parcel will experience a buoyancy force acting to return the parcel to its initial position. At the displaced depth, the buoyancy force (F_B, eq. 3.1) is the difference of the parcel weight ($Vg\rho'$) and the surrounding water at the new depth ($Vg\rho_2$), where *V* is the volume of the water parcel [*Stewart*, 2008].

$$F_B = gV(\rho_2 - \rho') \tag{3.1}$$

The change in density of the parcel (ρ') and water (ρ_2) due to the change in depth (δz) is given by equations 3.2 and 3.3 [*Stewart*, 2008].

$$\rho_2 = \rho + \left(\frac{d\rho}{dz}\right)_{water} \delta z \tag{3.2}$$

$$\rho' = \rho + \left(\frac{d\rho}{dz}\right)_{parcel} \delta z \tag{3.3}$$

When the buoyancy force accelerates the displaced parcel back to its rest position, the parcel overshoots the rest position and then oscillates about the rest position as the buoyancy force

changes. The buoyancy frequency, or Brunt Väisälä Frequency (*N*) describes the oscillation frequency (eq. 3.4), where g is gravity, ρ is density, and $\frac{d\rho}{dz}$ is the change in density with depth. The complete proof can be found in an *Introduction to Physical Oceanography* by Stewart [*Stewart*, 2008].

$$N = \sqrt{-\frac{g}{\rho}\frac{d\rho}{dz}} \tag{3.4}$$

$$N^2 > 0 \; Stable$$

$$N^2 = 0 \; Neutral \; Stability$$

$$N^2 < 0 \; Unstable$$

When N^2 is positive, the ocean is stably stratified and a parcel will oscillate about its rest position when perturbed. Large values indicate stronger stratification and higher oscillation frequencies. High *N* values exist at the pycnocline due to large vertical density gradients. At negative values, the solution represents an exponentially growing function and an initial perturbation/displacement will continue to grow [*McWilliams*, 2006].

Propagating gravity waves at the sea surface displace the sea surface and isopycnals uniformly such that $\frac{\eta}{h} \approx 1$, where η is the sea surface displacement and *h* is the displacement of the density interface [*Hautala et al*., 2005]. The isobars remain parallel to the isopycnals presenting a barotropic condition with no effect on the density profile and therefore a constant velocity profile with depth. Internal gravity waves moving along the pycnocline represent a baroclinic condition. The sea surface displacement is much smaller than the interface displacement, following $\frac{\eta}{h} \approx \frac{g'}{g}$ [*Hautala et al*., 2005]. The reduced gravity (g') term, $g' = g\frac{\Delta\rho}{\rho_o}$,

results from small changes in density ($\Delta\rho$) between two fluid layers compared to the reference density (ρ_o) [*McWilliams*, 2006]. Since the displacement of the sea surface and the density interface are not equal, the vertical density profile and velocity change with depth because the isobars and isopycnals are no longer parallel.

Internal gravity waves propagating on the pycnocline have the highest frequency and shortest period ($Period = \frac{2\pi}{N}$) due to the largest vertical density gradients. Internal gravity waves on the pycnocline will also affect the temperature/density variance to a large degree because a small perturbation in a region of large gradients has a large effect on the field.

Internal gravity waves are excited by tides, perturbations to the ocean, including current flow interaction with topography (ex. mountain lee waves), geostrophic adjustment, and ocean response to external forcings [*McWilliams*, 2006]. The submesoscale experiment that is the focus of this thesis occurred in a measurement zone that includes the Santa Monica Bight to Catalina Island. This region is characterized by strong currents of the California Current system (fig. 4.1), complex bottom topography, and periodic wind events. The region also has a pronounced pycnocline necessary for internal gravity waves. Understandably, internal gravity waves constituted a dominant signal in our measurements.

CHAPTER 4

Experimental Method

In section 1.3 it is discussed how submesoscale features are under sampled with respect to *in situ* observations. The length and time scales are inhibitive to sampling by common research platforms that lack the capability to perform high temporal-spatial resolution measurements of $O(< 1)$ km and O(minutes). Led by Burkard Baschek and Jeroen Molemaker at UCLA, a sampling method has been developed to provide high temporal-spatial resolution measurements of submesoscale fronts, eddies, and filaments.

4.1 Experimental Method

The sampling approach combines satellite, aircraft, and *in situ* instruments to observe submesoscale features with SST signatures. Initially, synthetic aperture radar (SAR) equipped satellite and aircraft observe the target region to locate regions of elevated submesoscale activity. SAR images are downloaded to land based operating stations and coordinates are relayed to the other patrolling aircraft and research vessels. The aircraft arrive first and begin mapping the sea surface with infrared (IR) cameras to further isolate submesoscale features and produce 2D georeferenced SST maps at a higher frequency than the SAR platforms. The aircraft coordinate their surface investigation with aircraft radio frequencies. This allows a larger domain to be searched and then narrowed when a submesoscale feature is found. Once a feature is located, the aircraft simultaneously map the feature and transmit georeferenced maps to supporting research vessels in quasi-real time by radio internet communications. The vessels upload the maps into a chart plotting program and deploy to the measurement location. The maneuverable, high speed

vessels arrive onsite and begin high resolution sampling. The vessels deploy surface Lagrangian drifters and multiple *in situ* instruments to provide surface and subsurface measurements of temperature, pressure, and salinity. The aircraft continually map the feature, providing updated position data to increase measurement accuracy.

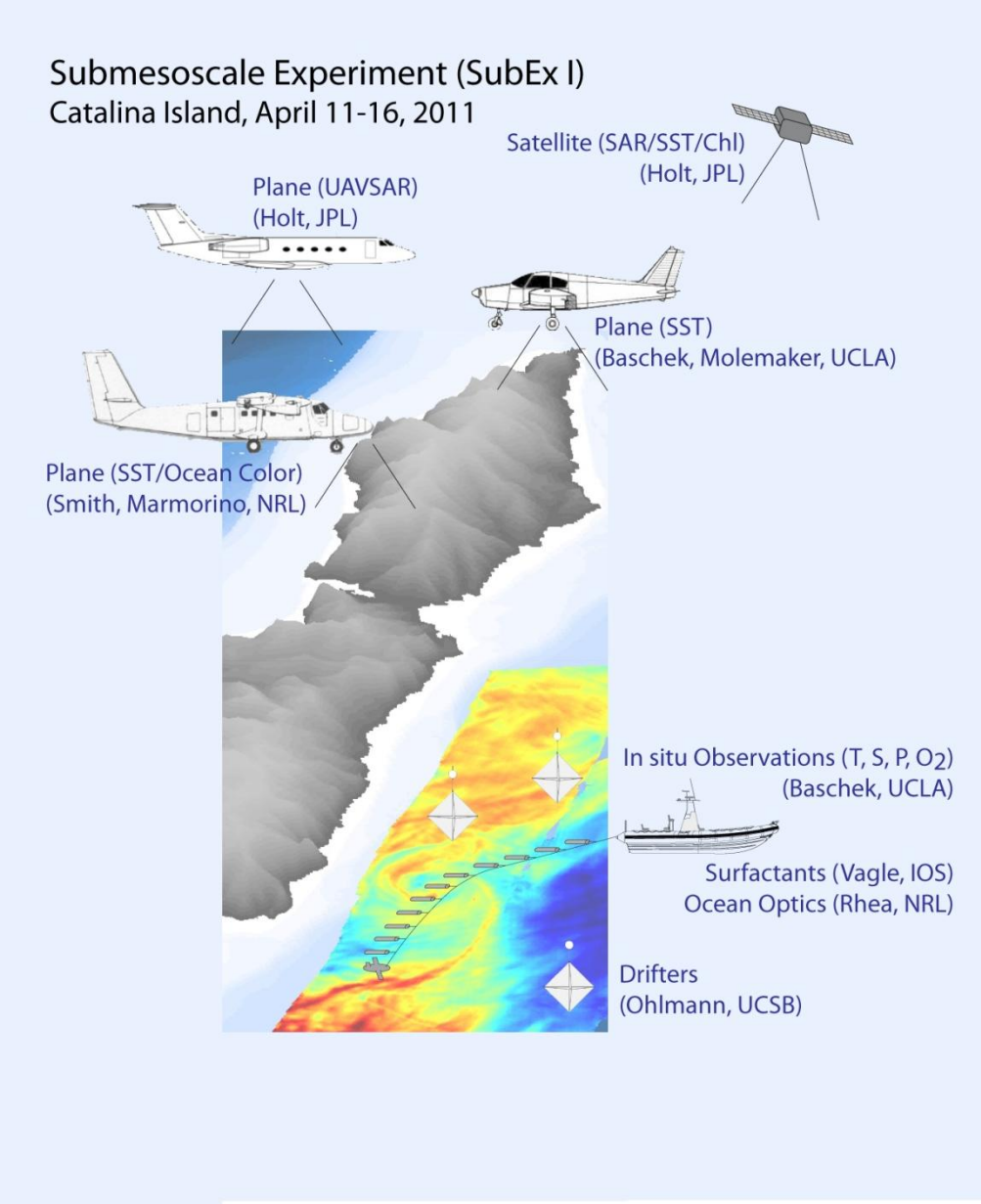

Figure 4.1: Experiment infrastructure and participating scientists [Burkard Baschek, personal communication].

The primary goal is to establish a temporal-spatial evolution of the submesoscale feature and establish correlations between hydrographic properties. This will aid in understanding submesoscale dynamics and the cumulative influence on the ocean energy budget, biology, and general circulation.

The submesoscale experiment series detailed in this thesis consists of daily measurements during a weeklong period from April 10-16, 2011 (hereinafter *SubEx*). *SubEx* is part of a larger NASA funded project with Co-Principal Investigators Burkard Baschek, Jeroen Molemaker, and Benjamin Holt on observations of submesoscale features, including fronts, eddies, and filaments.

Scientists from UCLA hosted and led the field experiments with participating agencies and scientists from the Jet Propulsion Laboratory (JPL), Naval Research Laboratory (NRL), Institute of Ocean Sciences (IOS), and University of California at Santa Barbara (UCSB).

4.2 Experiment Location

The main region of study during *SubEx* was the Southern California Bight; principally the Santa Monica Basin, San Pedro Basin, and the waters near Santa Catalina Island (fig. 4.1, hereinafter Catalina Island) [*Hickey*, 1992]. Land based limits of the research domain include Palos Verdes, Catalina Island, and Point Dume (Malibu, CA).

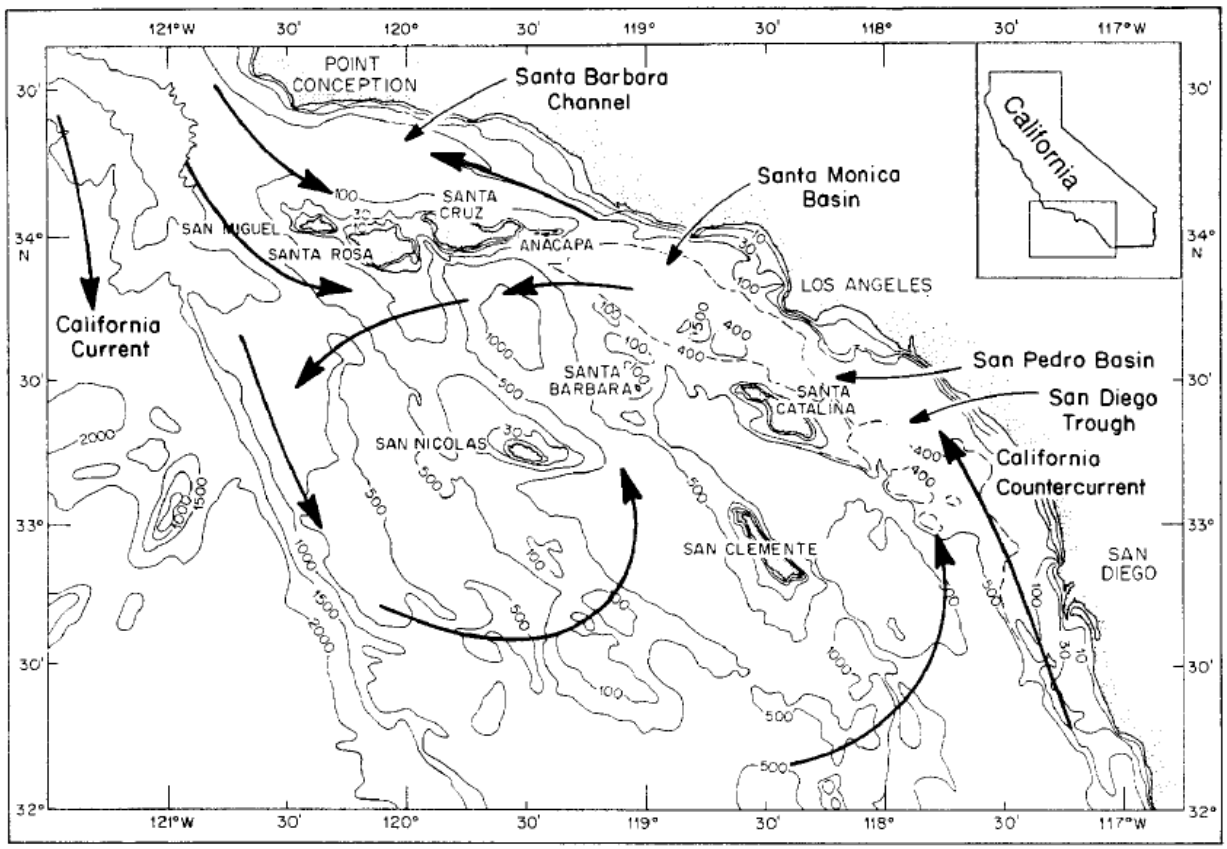

Figure 4.2: Bathymetry and general circulation for Southern California. Image from Hickey, B.M. 1992 – Circulation over the Santa Monica-San Pedro basin and shelf.

Submesoscale activity has been previously documented from SAR and SST imagery [*DiGiacomo and Holt,* 2001; *Holt,* 2004]. Current shear and strain necessary for the formation of submesoscale features are supplied by the interacting currents of the California Current System and the current interactions with topography (fig. 4.2).

The region's close proximity to available resources and favorable weather with predominately clear skies necessary for aerial measurements make it an ideal measurement location. Aircraft and vessels can be onsite to any location within the domain in 30-45 minutes. This allows for longer measurement durations and multiple measurement periods in a day.

4.3 Measurement Platforms

The sampling platforms are divided into two parts: (1) aerial platforms with remote sensing instruments, and (2) *in situ* platforms. The aerial remote sensing consisted of SAR, infrared (IR), and visible light imaging. SAR imagery was obtained from satellites and aircraft, while the visible and infrared observations were conducted by two aircraft:

1. Naval Research Laboratory aircraft (hereinafter *NRL Aircraft*) with several IR optics
2. A UCLA aircraft (hereinafter *UCLA Aircraft*) with long wave IR optics and visible light digital camera.

The i*n situ* measurements were performed by the cabin cruiser *Never Satisfied* which deployed drifters and the UCLA Zodiac which performed subsurface measurements (hereinafter *UCLA Zodiac*).

The analysis includes data from the *UCLA Aircraft* IR mapping, drifter deployment by the *Never Satisfied*, and *in situ* measurements by the *UCLA Zodiac*. The SAR and NRL observations provided complimentary, but non critical data to producing a qualitative description of the submesoscale dynamics. The platforms are detailed in the experimental method to provide an overview of the resources employed and because they were instrumental in locating the submesoscale features.

4.3.1 Synthetic Aperture Radar (SAR)

The accumulation of buoyant surfactants of biogenic, or geological origin at convergence zones (downwelling) acts to suppress the sea surface roughness by decreasing the friction coefficient at the air sea interface and increasing water tension [*Holt*, 2004]. SAR measures backscatter

intensity based on sea surface roughness, which is then indicative of the flow field [*DiGiacomo and Holt*, 2001; *Holt*, 2004]. Studies also show that features detected by SAR imagery have IR detectable SST signatures and will therefore be supplemental to the IR SST images provided by the *NRL* and *UCLA Aircraft* [*DiGiacomo and Holt*, 2001; *Holt*, 2004].

To increase surface coverage, SAR imagery was obtained from 3 orbiting satellites: European Space Agency's Envisat ASAR and ERS-2 SAR, and Jaxa's ALOS Palsar. The satellite overpasses are limited to every few days, but provide spatial resolution of *O*(25-100) m [*Holt*, 2004]. The *SubEx* trials were planned to coincide with maximum SAR coverage. JPL also operated a Gulfstream jet equipped with SAR. The maps are transferred to land based operating stations and used to locate active regions for further investigation.

Figure 4.3: SAR georeferenced map of mosaiced images from 04.15.2011 provided by the JPL operated Gulfstream jet. The *.kmz extension files are compatible with Google earth maps, or other map programs.

4.3.2 *NRL Aircraft* and IR SST Mapping

The NRL lab group of George Marmorino and Geoffrey Smith performed observations from a twin engine turboprop DHC-6 Twin Otter aircraft. The instrument suite contained several IR imagers of different wavelengths as detailed in table 4.1.

Instrument	Wavelength (μm)	Mechanics	Pixels
CASI-1500 VNIR	0.38 – 1.05 (VNIR)	nadir looking pushbroom	1500 cross-track
microSHINE VNIR	0.38-1.0 (VNIR)	nadir looking pushbroom	450 cross-track
FLIR SC6000	1.0-5.0 (Mid wave)	gimbal mount	640x480
Merlin-Mid	1.5-5.5 (Mid wave)	nadir mount	320x256
QWIP	7.5 – 13.0	gimbal mount	640x512

Table 4.1: Instrument model, type, and capabilities onboard the *NRL Aircraft*. The imagers measured between 0.38-1.05 micrometers (μm) for very near IR (VNIR), 1.0-5.0 μm for mid-wave IR, and 7.5-13.0 μm for long-wave IR. FOV is field of view. Instruments are accurate to ± 2℃, or ± 2% of the reading.

The *NRL Aircraft* communicated directly with the *UCLA Aircraft* though aircraft radio frequencies.

4.3.3 *UCLA Aircraft* and IR SST Mapping

The *UCLA Aircraft* is a Piper Cherokee operated from Santa Monica Airport by Proteus Air. Much of the hardware to software interface is a result of work by Jeroen Molemaker. A FLIR A325 long wave IR (7.5-13 μm) camera recorded 320x240 pixel SST images at 60 Hz. Images were saved at 3.75 Hz. The IR camera is coupled to an Arecont AC5100 visible light digital

camera to detect visible surface fields, such as surfactant accumulations, and to differentiate anomalous IR measurements in the presence of clouds or vessels.

The FLIR A325 is accurate to ± 2% of the reading and performs periodic recalibrations to reduce temperature drift as the sensor temperature fluctuates. The orientation of the instrument package is fixed relative to an onboard Xsens MTi-G Altitude and Heading Reference System. The MTi-G provides position (via global positioning system (GPS)) and 3D orientation data with tilt, altitude, and position precision of 0.4°, 20 m, and 3 m respectively.

Using a 45° angle lens at a measurement altitude of 3000 m (10000 ft), a flight track (overpass) measures a 2.5 km (≈1.6 mile) SST swath. An aircraft cruising speed of 200 km hr^{-1} (108 knots) and a total flight duration of 4 hours allows for a 10x20 km area to be mapped approximately every 30 minutes consecutively for 2-3 hours, providing between 4-7 SST maps per flight and upwards of 10-15 per day.

The SST images are mosaiced together on a latitude/longitude or Universal Transverse Mercator (UTM) grid by an in-house mapping program. The data are corrected for atmospheric temperature and humidity. The raw data has 10 m resolution at the measurement altitude. When combined with the MTi-G-GPS compass information and cruising speed, the georeferenced SST maps have a spatial and temporal resolution of *O*(25-50) m and of *O*(10-15) minutes respectively per 20 km track.

The georeferenced SST maps are automatically transferred to the *UCLA Zodiac* through a radio internet link. Communication is also possible with a marine radio installed on the aircraft. Both have a line of sight range of 25 miles.

4.3.4 *Never Satisfied* and Lagrangian Surface Drifter Deployment

The *Never Satisfied* deployed 14 surface Lagrangian drifters; 9 Microstar drifters operated by Carter Ohlmann of UCSB (hereinafter *Drifters* or drifters 1-9) and 5 drifters developed in-house by Svein Vagle of IOS (hereinafter *IOS Drifters*).

The Microstar drifters are designed by the Pacific Gyre Corporation for coastal environments and repeat retrieval/deployment cycles from a small research vessel [*Ohlmann and Sybrandy*, 2002; *Ohlmann et al., 2005*]. They have a subsurface collapsible nylon drogue centered at 1 m depth with a drag-area ratio greater than 40 [*Niiler et al*., 1992]. A tethered surface float contains power, GPS unit, and communications unit (cellular) [*Ohlmann et al*., 2005]. Experiments show the drifter slip to be 0.1% of the wind speed and oriented in the opposite direction of the surface wave propagation - i.e. 180° out of phase [*Niiler et al*., 1992]. GPS position accurate to 5 m is transmitted every 10 minutes to an internet based server [Ohlmann et al., 2005]. The position data are retrieved from the internet, or by Iridium (satellite) receiver onboard the vessel. This allows for the *Drifters* to be retrieved and deployed repeatedly in the vicinity of the front. The short interval recording frequency is ideal for submesoscale flows and should result in adequate spatial-temporal descriptions of the flow [*Ohlmann et al*., 2005].

The *IOS Drifters* were deployed in unison with the *Drifters*. The *IOS Drifters* were equipped with submersible RBR TR-1050 temperature sensors at 0.1 m depth. These sensors have an accuracy of ± 0.002 ℃ and < 3 second time constant. One *IOS Drifter* was equipped with a 1.2 MHz Acoustic Doppler Current Profiler (ADCP) and 4 RBR TR-1050s at 0.275 m, 1.1 m, 1.45 m, and 1.8 m depths. Position was recorded by internal GPS and transmitted in similar fashion as the *Drifters* (cellular network).

Depending on deployment, the drifter data can be used to determine surface currents, strain, divergence/convergence near the front, and vorticity of the flow.

4.3.5 *UCLA Zodiac* and Subsurface *In Situ* Observations

The *UCLA Zodiac* is a lightweight, 27 foot zodiac capable of top speeds near 45 knots. The vessel speed and maneuverability make it an ideal platform for submesoscale research.

The zodiac is equipped with a Sea-Bird Electronics (SBE) 45 MicroTSG (thermosalinograph), meteorological station, and Towed Instrument Array (detailed below). Position is determined with a Hemisphere V110 2D-GPS.

The SBE 45 has an accuracy of ± 0.002℃ and ± 0.005 Practical Salinity Units (PSU). In the SBE 45 flow system, a debubbler is placed upstream of the SBE 45 and a self-priming pump downstream to prevent bubble introduction to the flow system. The SBE 45 (hereinafter *surface sampler*) provided near surface measurements at approximately 0.2 m depth.

To measure submesoscale features with sharp density features of *O*(5-50) m, a Towed Instrument Array (TIA) was developed by Burkard Baschek at UCLA. The TIA is composed of multiple instruments attached to 5mm spectra line at predetermined positions. The string is deployed with an aluminum 610 BOTwing depressor weight (11 kg dry weight and 122 cm wingspan) at the end to maintain constant depth during underway transects with continuous sampling by the instruments. The horizontal and vertical resolution are dependent on tow speed and instrument spacing. Under standard tow conditions at speeds near 4 m s^{-1} and instrument spacing of 0.5 to 7 m, the horizontal and vertical resolutions are ≤ 4 m (at 1 Hz sampling) and <

7 m respectively. The vertical instrument spacing can be manipulated to have higher resolution (in the vertical) measurements near the surface.

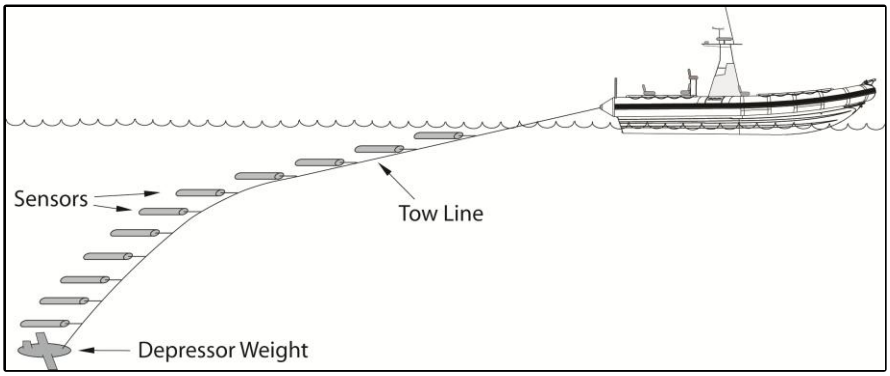

Figure 4.4: *UCLA Zodiac* with towed instrument array. Instruments are spaced along the spectra line with a BOTwing depressor weight [Burkard Baschek, personal communication].

Speed variations changed both the lift and drag proportionately, providing near constant measurement depths [Burkard Baschek, personal communication].

The instruments deployed along the TIA are RBR temperature, pressure, and CTD sensors. The RBR XR-620 CTD sampled at 6 Hz with temperature, pressure, salinity, and oxygen accuracies of 2 mK, 37 cm, 1 μS cm^{-1}, and 2% respectively. Also included were RBR TDR 2050P pressure and temperature sensors, RBR TR-1060P temperature sensors, and RBR DR-1050 pressure sensors. The accuracies of these latter instruments with respect to temperature and pressure is 2 mK and 37 cm respectively. The tow line on April 14, 2011 was 100 m long, with 9 instruments measuring the upper 40 m of the water column. The *surface sampler* (0.2 m depth) is also included in the TIA measurements.

Sensor	Pressure [dbar] (1m ≈ 1dbar)	Variance of Pressure
SBE 45	0.2	0
2	1.3	0.001
3	1.5	0.006
4	2.6	0.01
5	3.5	0.02
6	8.8	0.1
7	10.3	0.2
8	18.8	0.2
9	27.6	0.3
10	37.9	0.3

Table 4.2: Sensor depth variance (tracer for depth fluctuation).

The mean of each instrument's pressure data indicate the instrument's mean depth (table 4.2). The variance of the depth is a tracer for depth error (note: not corrected for actual pressure signals related to submesoscale phenomena). Small changes in the angle of attack will have the largest effect on vertical displacement as distance along the TIA increases, but error remains < 0.5 m.

The TIA was used to make measurements of the surface front in succession at speeds up to 5 m s^{-1}. Periodic temperature and salinity profiles (upcast/downcast) were made at deployment and retrieval when the weight of the BOTwing orients the TIA vertically.

CHAPTER 5

Results

As previously noted, the scale and resolution of measurements expected from the *SubEx* experimental method is a new frontier in submesoscale measurements. The experimental method represents two years of instrument, software, and communication network development by myself, and substantially more time by Burkard Baschek and Jeroen Molemaker who both formed the foundation of the research method. As *SubEx* is part of ongoing research, the results will focus on the deployment and analysis method to isolate areas in need of improvement so the next series of measurements are more successful. This by no means suggests that *SubEx* was unsuccessful, just that in the presence of an internal gravity wave signal that "contaminates" our data, the experimental method must be adapted to overcome this issue. A better understanding of submesoscale dynamics (from an *in situ* perspective) will ultimately follow when the measurement method is refined.

The results and conclusions are based on a submesoscale surface density front measured in the vicinity of Catalina Island on April 14, 2011 from 1100-1400 Pacific Daylight Time (PDT; hereinafter all times are PDT in 24 hour format unless stated otherwise). The analysis includes data from the *UCLA Aircraft* IR SST mapping, *Never Satisfied Drifter* deployment, and *UCLA Zodiac in situ* TIA measurements.

5.1 Satellite Images and Aircraft Mapping

Moderate Resolution Imaging Spectroradiometer (MODIS) SST images were downloaded each morning prior to deployment to isolate regions with submesoscale activity. MODIS SST images

with 1 km resolution are a product of coupling top of the atmosphere IR radiation measurements from NASA's Terra and Aqua satellites with *in situ* SST measurements [available at *http://www.sccoos.org* and *http://www.rapidfire.sci.gsfc.nasa.gov*]. Terra and Aqua satellites have opposing tracks that overpass a region once per day. The overpasses on the 13th and 14th of April occurred at 1800 and 1845 Coordinated Universal Time (UTC; PDT is UTC-7 hours) respectively. The images downloaded on April 14 (circa 0500) are therefore taken at minimum 18 hours earlier (fig. 5.1).

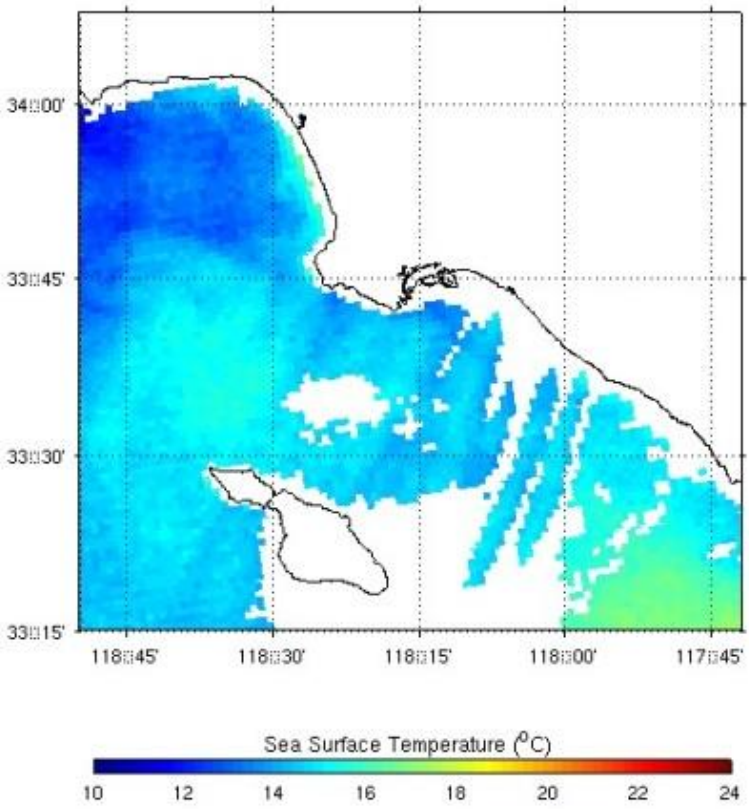

Figure 5.1: MODIS SST image downloaded from http://www.sccoos.org/ on April 14, 2011 at ≈ 0500, prior to measurements. Image is likely from Terra/Aqua overpass on April 13 at 1800 UTC [available at *http://www.rapidfire.sci.gsfc.nasa.gov*].

In figure 5.1 there are no discernible submesoscale fronts near Catalina Island. At 1 km resolution, the across-front direction is subgrid, but the along-front direction is not. SST fronts should be visible, but as "smoothed" gradients, rather than sharp features representative of the submesoscale. Near 22.45°N ,118.45°W there is a weak SST curved front.

There are also submesoscale conglomerations of surface chlorophyll (fig 5.2). Elevated chlorophyll concentrations are found in near shore regions and a localized region at the west end of Catalina Island. Figure 5.2 was downloaded at the same time as figure 5.1 and SST spatial coverage indicates congruent times (1800 UTC on April 13, 2011).

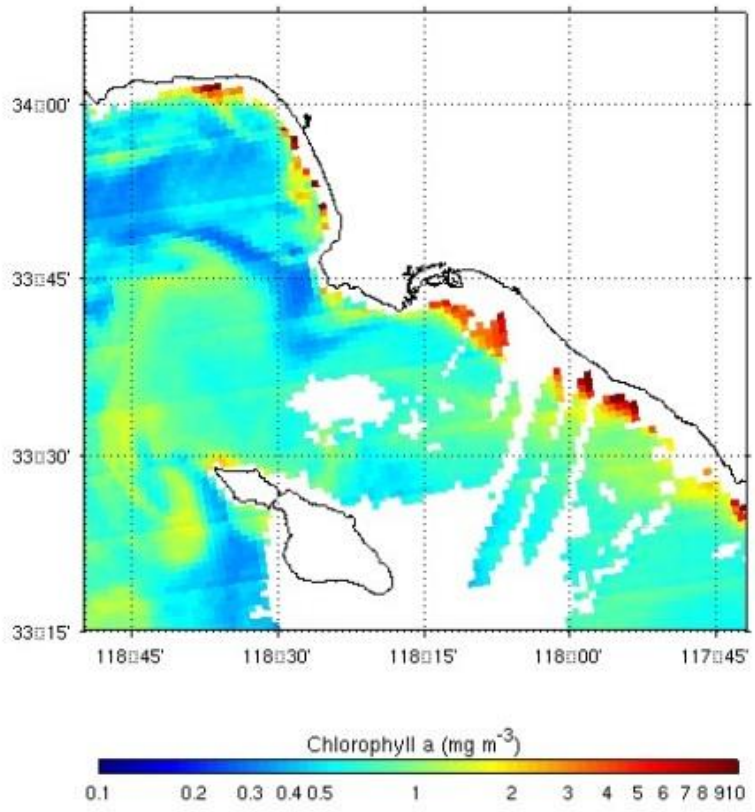

Figure 5.2: MODIS chlorophyll image downloaded from http://www.sccoos.org/ on April 14, 2011 at ≈ 0500 prior to measurements. Image is likely from terra/aqua overpass on April 13 at 1800 UTC, congruent with figure 5.1 [available at *http://www.rapidfire.sci.gsfc.nasa.gov*].

The elevated chlorophyll concentration suggests that the measurement region may have submesoscale features with upwelling velocities introducing nutrients to the euphotic zone. The orbit frequency is short enough to capture the chlorophyll signal from plankton with lifetimes of *O*(days). The region may have common upwelling occurrences from submesoscale features, but the SST signatures of the submesoscale features decays at rates faster than the satellite sampling frequency. More observations are needed to discern if these elevated chlorophyll regions are from submesoscale features, or wind forced Ekman upwelling events. It is possible that a coastal Ekman upwelling event occurred and the water mass was advected offshore and stirred.

These two measurements (SST and Chlorophyll) provide insight into the dynamics and observational limitations of different platforms. Although 1 km resolution, the MODIS SST images do not show Catalina Island as an active submesoscale regime. Chlorophyll concentrations do indicate broad/weak submesoscale activity in more regions, but supplementary observations are necessary to differentiate between frontogenesis, or Ekman events as the mechanism for vertical nutrient flux.

In comparison to the MODIS data, an analysis of *SubEx* data will show that these regions have frequent submesoscale features that exhibit sharp SST gradients.

Infrared mapping by the *UCLA Aircraft* produced 4 images of the SST front (fig. 5.3). The time spanned by these images is 153 minutes, with mapping durations of 34, 33, 35, and 37 minutes for each complete map of ≈ 150 km^2.

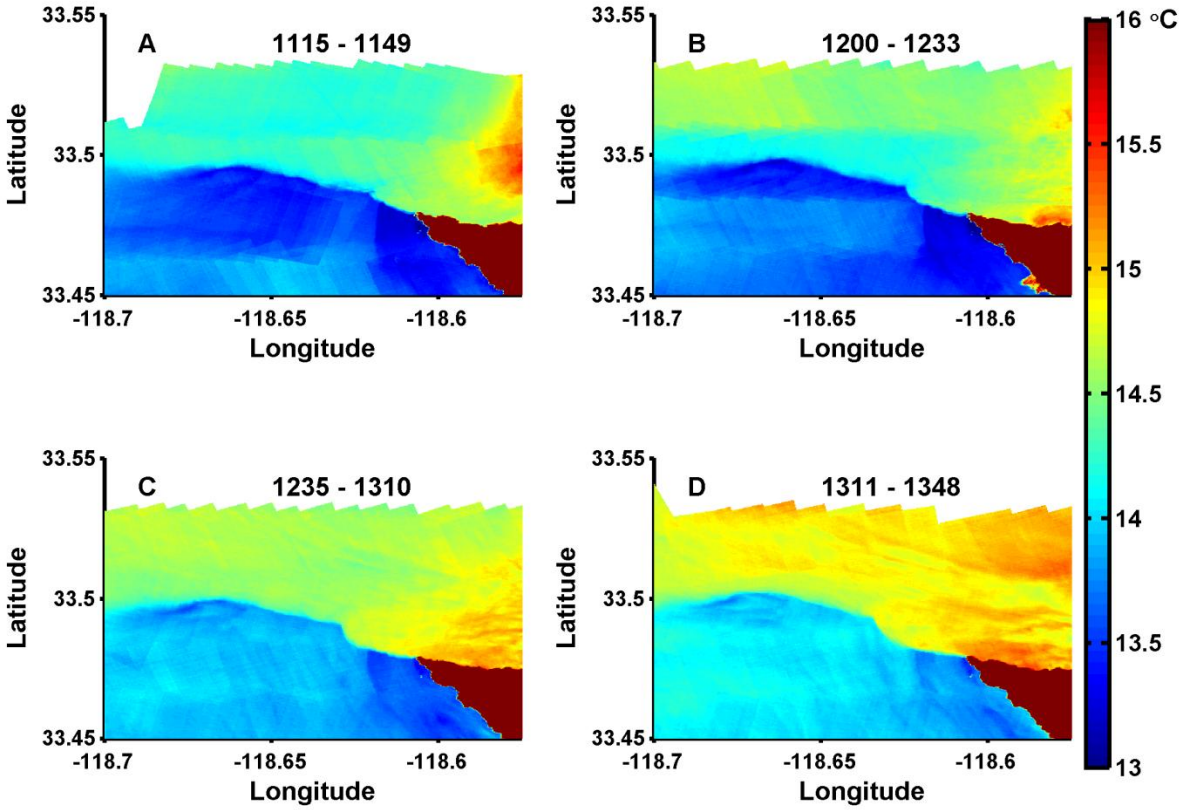

Figure 5.3: 4 images (A-D) of the SST front on April 14 from the *UCLA Aircraft* IR SST mapping. The mapping domains are reduced to ≈ 100 km^2. Subplot titles are the times of the first and last image of the mapping.

The front position was automatically determined at the maximum of the absolute horizontal temperature gradient ($|\nabla T|$), where $\frac{dT}{dx}$ and $\frac{dT}{dy}$ are the temperature gradients in the zonal and meridional directions respectively (eq. 5.1; gradient method). The raw image was smoothed with a 2D Gaussian kernel filter to reduce false gradients introduced from the mapping of the raw images (fig. 5.4).

$$|\nabla T| = \sqrt{\left(\frac{dT}{dx}\right)^2 + \left(\frac{dT}{dy}\right)^2} \tag{5.1}$$

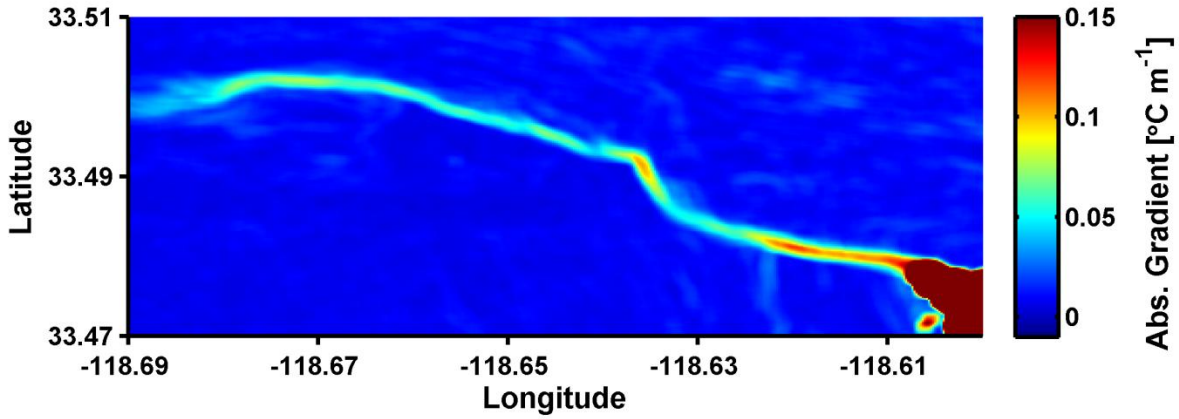

Figure 5.4: 2D Gaussian smoothed SST gradient. Abs. gradient, is the absolute value of the temperature gradient from equation 5.1.

The front positions from the gradient method were compared to positions derived from isotherms. The isotherm method has predictable results, but was not used due to a warming trend in the SST images. Adjusting the isotherm value between images to account for image to image mean temperature change would induce systematic error as the front advection produces a biased mean temperature value as the domain proportionality of warm to cold area changes in accordance with the front advection. Most importantly, the dynamics are not governed by temperature values, only gradients.

The front latitude/longitude positions (determined with the gradient method) were linearly interpolated to a 1 minute time vector using times corresponding to when the raw IR SST image was taken of the front in direct vicinity of the surface drifters. The times are then 1143, 1223, 1300, and 1340.

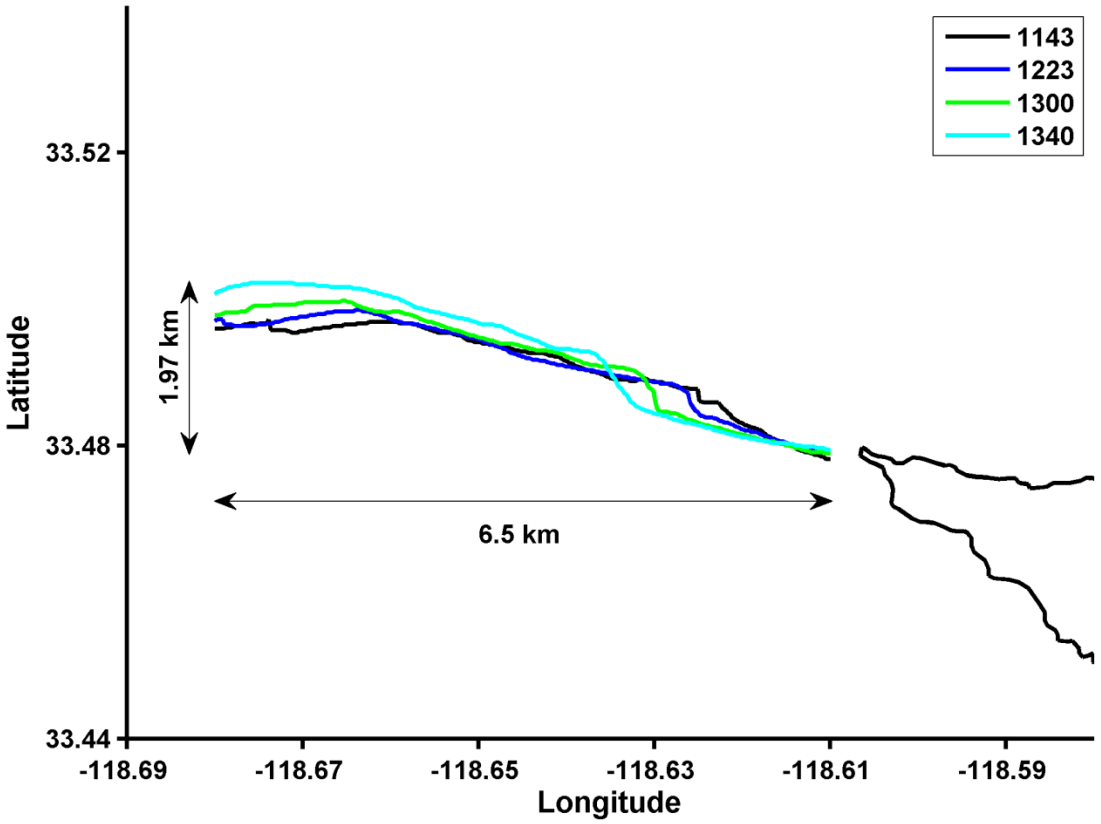

Figure 5.5: Front position at times 1143, 1223, 1300, and 1340. Position is determined by the gradient method (fig 5.4, eq. 5.1).

The interpolation produces a higher resolution evolutionary sequence of the front with time increments comparable to the recording frequency of the surface drifters and TIA instruments. The IR SST mapping sets the time domain for all consequent analysis.

One caveat to the interpolation method is that it assumes the parcel displacement is only along lines of constant longitude - i.e. north, or south. Since the front is primarily advected to the north, the associated errors are negligible (fig 5.5). A southwesterly intrusion near 118.62°W is an exception, but this region is not used in calculations, therefore any associated error is nullified.

The SST front extends approximately 6.50 km to the west and 1.97 km to the north the west end of Catalina Island (commonly referred to as "Land's End" or "West End"). These limits are set by a weak temperature gradient west of 118.7°W and insufficient IR SST coverage. This does not imply there are no relevant dynamics, only that we have reached the edge our measurement domain (fig 5.3).

There are cold waters to the south side of the frontal interface. A discussion of the changes in temperature measured by the IR cameras will be addressed following the *in situ* measurement analysis. The IR cameras do not directly measure sea surface temperature, therefore an absolute temperature measurement is required to calibrate/confirm the temperature values. The absolute measurements are supplied by the *surface sampler* and TIA.

The front advection was calculated based on the mean latitudinal displacement over the duration of the measurements (≈ 2 hours). The two primary directions of advection, north and south, were split at 118.635°W (fig. 5.5). West (east) of 118.635°W the front moves north (south) at an average 6 cm s^{-1} (4 cm s^{-1}). These values are estimates of the front advection based only on IR SST images.

Two km resolution surface currents from the Coastal Ocean Dynamics Applications Radar (CODAR) system at times 1100, 1200, and 1300 support the calculated front movement [available at *http://www.sccoos.org*]. The CODAR coverage of surface currents is limited, but does indicate an ≈ 6 cm s^{-1} southwesterly surface current within 2 km of West End. There is a northerly current 4 km offshore at ≈ 10 to 12 cm s^{-1}. The front displacement calculated from IR SST images is qualitatively consistent with the CODAR surface currents.

The large scale, general circulation of the California Current System (fig 4.1) is also in good agreement with surface currents derived from IR SST images. The flow on the northern flank of Catalina Island is an area of positive relative vorticity formed by the velocity shear due to friction at the coastal boundary at West End. The velocity shear may induce a cyclonic current at West End, deflecting the front to the south. This is met by the northward eddying current on the southern flank of Catalina Island, distorting the front as seen in figures 5.3 and 5.5.

The *UCLA Aircraft* IR SST measurements successfully detect submesoscale features when similar platforms do not. Clearly, the necessary temporal-spatial resolution must be greater than 1 day and 1km respectively. The *UCLA Aircraft* IR SST images have a temporal-spatial resolution of *O*(10-50) m and of *O*(0.5) hours that capture fine scale front displacements of *O*(10-50) m for bends/intrusions and mean front displacement of *O*(100-200) m. The IR SST derived surface currents compare favorably with CODAR, general circulation, and as we will see, Lagrangian surface drifters. However, a prominent weakness of the aerial platforms (*UCLA Aircraft* and Satellites) is their inability to substantiate subsurface dynamic.

5.2 TIA *In situ* Measurements – Transect Data

The *UCLA Zodiac* made 19 transects of the front. The total duration of measurements was 2.53 hours after excluding vessel turns (2-3 min per) and TIA deployment/retrieval (5-10/10-15 min per). In this time the vessel measured along 34.7 km at a mean velocity of 3.8 m s^{-1}.

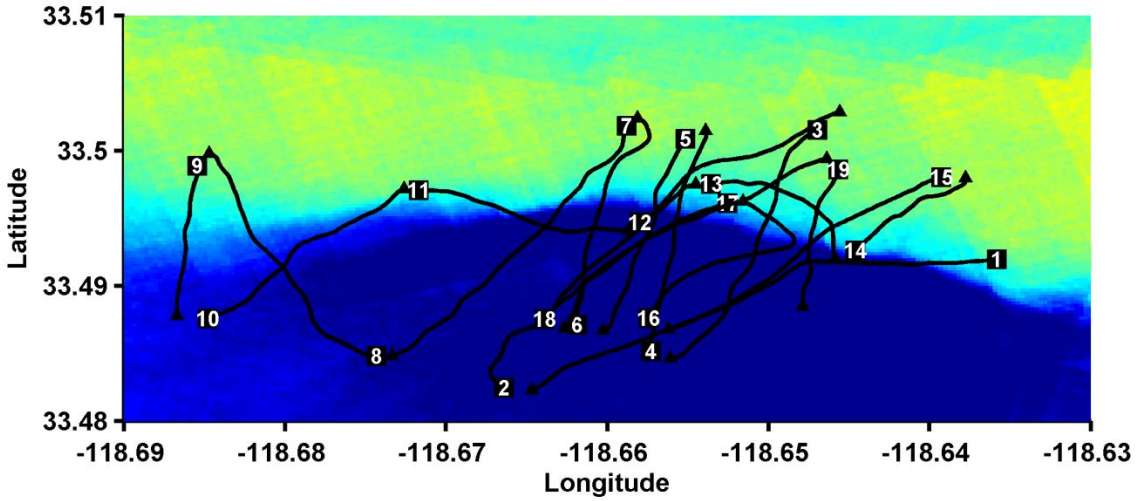

Figure 5.6: *UCLA Zodiac* transects on April 14, 2011. Black, numbered squares indicate the transect start position. Black triangles indicate the end of a transect. The 19 transects are consecutively numbered according to measurement order.

The 2D transects (horizontal distance and depth) contain pressure, temperature, and salinity measurements detailed in section 4.3.5. The salinity values had high frequency fluctuations on the order of 1 PSU attributed to instrument deployment error on April 14. The salinity measurements on April 15 and 16 had generally more stable and realistic salinity values. On these days, the changes in salinity had negligible contributions to changes in density and therefore salinity can be omitted to the first order in density calculations (temperature is now a proxy for density). Density was calculated with a mean salinity value of 33.2 PSU.

Of the 19 transects, transects 1-7, 15, 18 and 19 cross the front. Transects 3-7, 15, 18, and 19 overlap in time with the *UCLA Aircraft* IR SST maps. The *in situ* data has been corrected to account for the variable time shift of instruments proportional to depth/distance along string. For a 100 m tow-string, with an approximate 30° angle to the surface, the total horizontal displacement of the deepest instrument relative to the vessel position is ≈ 86 m. At the mean tow speed of 3.8 m s^{-1} there is a time shift from 0-22 seconds.

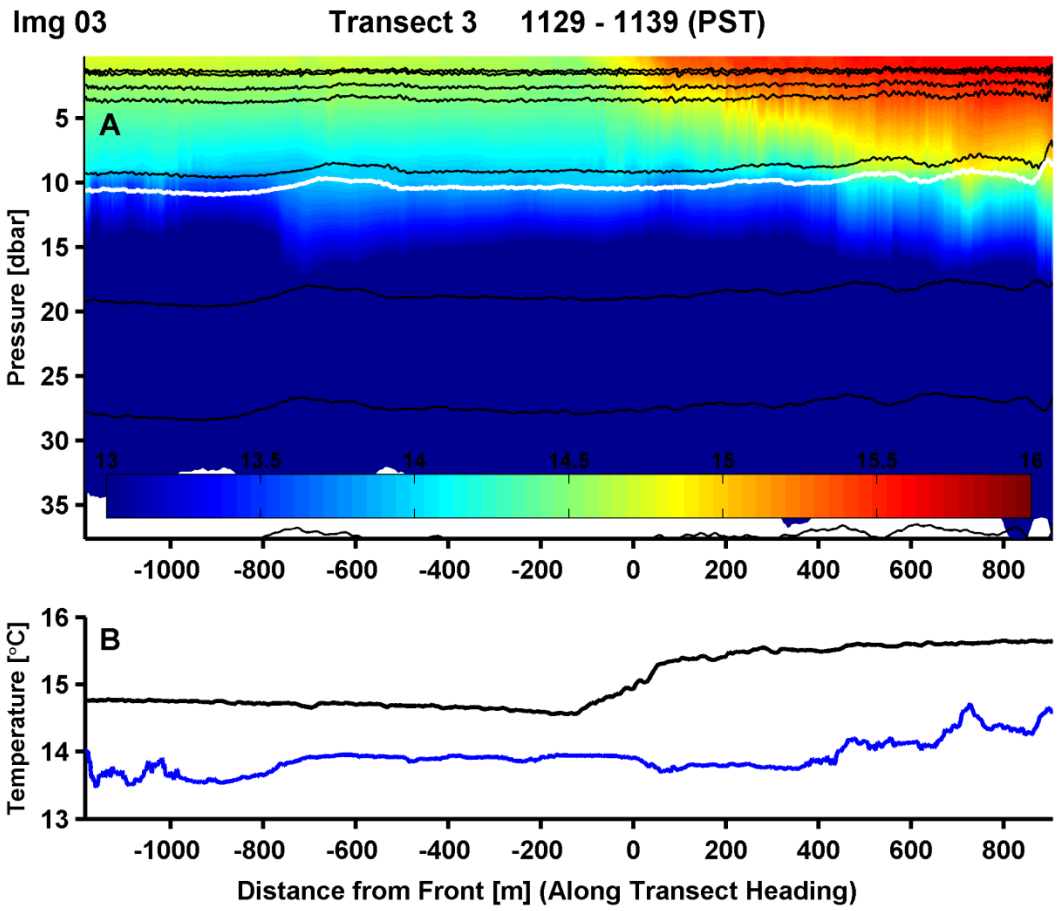

Figure 5.7: *In situ* data from transect 3. A) The interpolated 2D temperature field with black lines indicating instrument pressure (depth). The white line is the CTD depth. B) The temperature at 0.2 m and ≈ 10.3 m depth in black and blue respectively. Distance is a function of transect heading with 0 m indicating the point at which the vessel crosses the front. Negative values indicate the cold side of the front.

Figure 5.7 is a typical *in situ* measurement of the front (see Appendix A for remaining transects). The data are plotted as a function of distance along the transect. The *in situ* front positions were found using a threshold $\frac{dT}{dx}$ = 0.008°C m^{-1} (threshold value on unfiltered data).

The *in situ* temperature field was smoothed using a low pass Gaussian filter along pressure (depth) levels to reduce instrument noise and the surface wave signal on pressure. The filter width is approximately 80 m, or along 20 points (at 1 Hz sampling and vessel speed of 3.8 m s^{-1}).

The smoothed temperature field was then interpolated to fixed depth levels from 0.5 – 39.5 m. A second Gaussian low pass filter was applied to reduce the internal gravity wave signature at each depth level. The second filter equated to approximately 500 m smoothing, or 165 points. The strength of both Gaussian filters scales as the inverse of the squared filter width.

The front has a sharp density interface with a maximum gradient of 0.0031℃ m^{-1} at the surface. The mean frontal slope is 0.0146. The maximal of the mean vertical temperature gradient (0.282 ℃ m^{-1}) occurs at 10 m depth, indicating the thermocline depth.

5.3 SST Calibration

In situ measurements are absolute temperature measurements, while IR SST measurements record the relative temperature of the surface "skin" layer. The emitted longwave radiation intensity is converted to a temperature reading. The skin layer constitutes the upper few millimeters of the water column and is generally of O(0.1-1.5)℃ cooler than the subsurface, "bulk" temperature [*Veron et al*., 2008]. IR camera studies show that at higher wind speeds the skin to bulk temperature difference decreases. This is attributed to the increased turbulence and ventilation of the skin layer [*Veron et al*., 2008]. The camera measurements are also affected by changes in atmospheric variables, such as heating, or increase/decrease of the path length.

Since the IR camera temperature measurements are indirect and subject to bias due to atmospheric effects, the relative temperature values must be calibrated using *in situ* observed temperatures. To perform the calibration, the IR SST and the *in situ* data must be consistent with respect to front position and gradients.

The temperature data from the *in situ* and IR SST observations were interpolated in space and compared - i.e. the location of the transect temperature measurements are compared to the corresponding IR SST at the same location. This will nullify any cold/warm bias of the mean. The combinations are shown in table 5.1 and figure 5.8 (see Appendix B for remaining combinations).

Transect	Corresponding SST Map (fig 5.3)	Transect Mean Temperature [℃]	SST map Mean Temperature [℃]	Absolute Difference [℃]
3	A	15.06	13.74	1.32
4	A	14.93	13.65	1.28
5	A	14.98	13.66	1.32
6	A	15.00	13.73	1.27
7	B	15.01	13.58	1.43
15	C	15.25	14.12	1.13
18	C D	15.15	14.07 14.11	1.08 1.04
19	D	15.21	14.15	1.06

Table 5.1: Surface temperature from *in situ* transects and IR SST images.

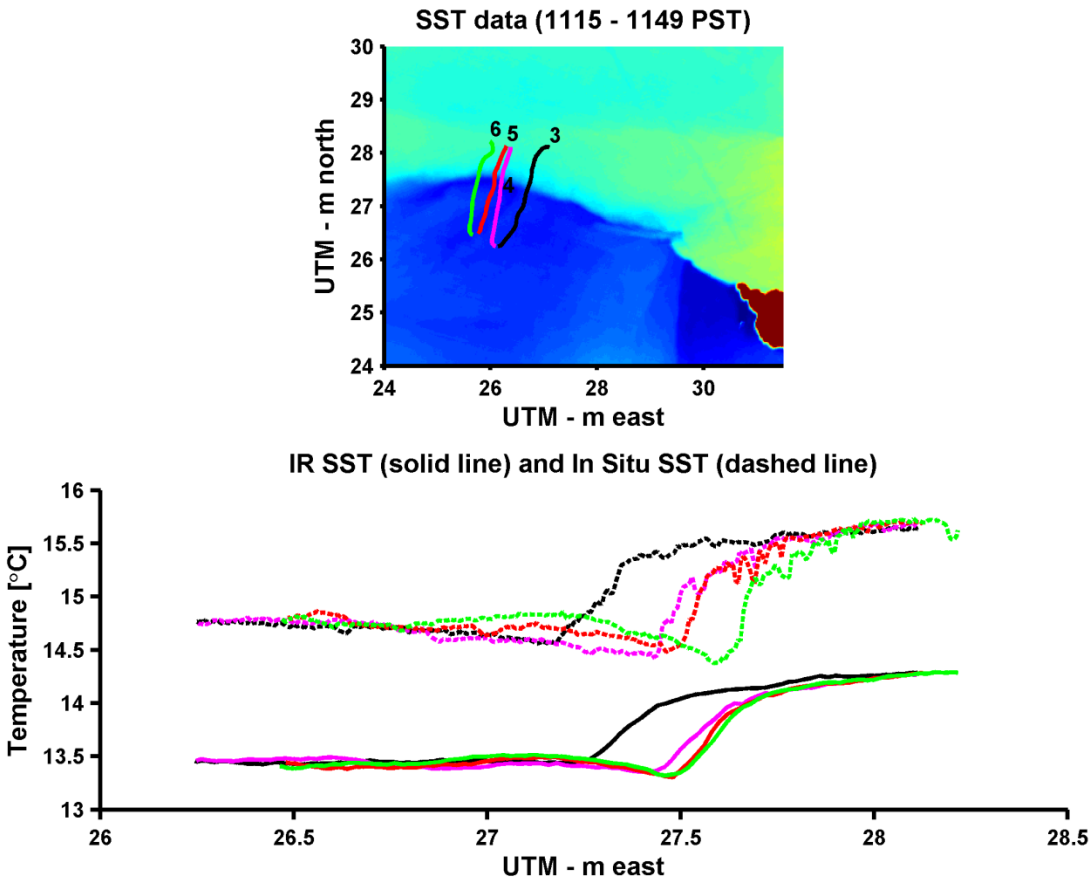

Figure 5.8: A) Time constrained *in situ* transects overlaid on IR SST image. B) Dashed lines are *in situ* temperature and solid lines are IR SST. The line colors are consistent between image A and B.

The position of the front and the temperature change recorded by the IR cameras and *in situ* instruments are consistent during the measurements. Slight differences of the front position (figure 5.8 B, green lines) are due to time differences between the SST image and transect times. In figure 5.8 the SST mapping ends at 1149, while transect 6 began at 1156. Transect 6 is still compared on the SST map because it is the closest image in time. The *in situ* temperatures are consistently cooler by a mean value of 1.21℃ with minimal variance of 0.02. From figure 5.3 and the calculations in table 5.1, the increasing temperature trend experienced during the measurements is captured by both platforms.

The common temperature trends of the skin layer (IR SST) and the bulk layer (represented here by the 0.2 m *surface sampler*) suggests that the surface renewal of the skin layer with subsurface water is sufficient, such that the relative temperature gradients reflect the absolute temperature gradients. Also, the atmospheric variations that affect the relative temperature readings are either minimal, constant valued, significantly reduced by the mapping program, or some combination thereof. The consistency between the two platforms allows for the coupling of IR SST and *in situ* temperature fields.

5.4 Lagrangian Drifter Data

The 9 *Drifters* were deployed in a 3x3 grid configuration covering a 2x2 km domain with ≈ 900 m grid spacing (fig. 5.9 A). The drifters are numbered according to figure 5.9 panel A and hereinafter referred to by numbers 1-9. Drifter 1 was deployed on the warm side of the front and drifters 2 and 3 near the frontal interface on the cold side (figure 5.9 A). Drifters 4-9 represent a consistent background deformation flow due to the limited distortion of the initial grid spacing (fig. 5.9 A-I).

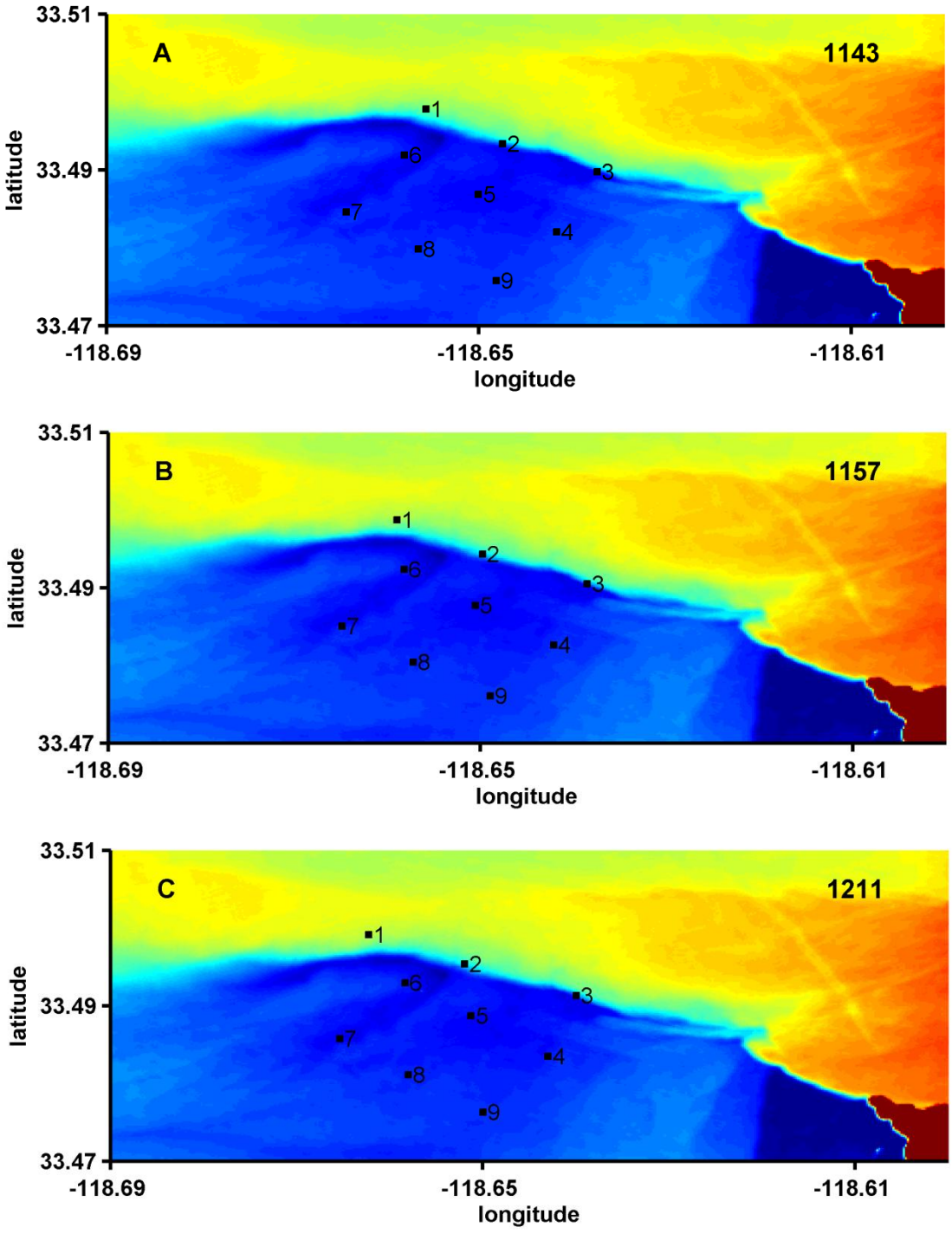
A
1143
B
1157
C
1211
1
2
3
4
5
6
7
8
9
33.51
33.49
33.47
latitude
-118.69
-118.65
-118.61
longitude

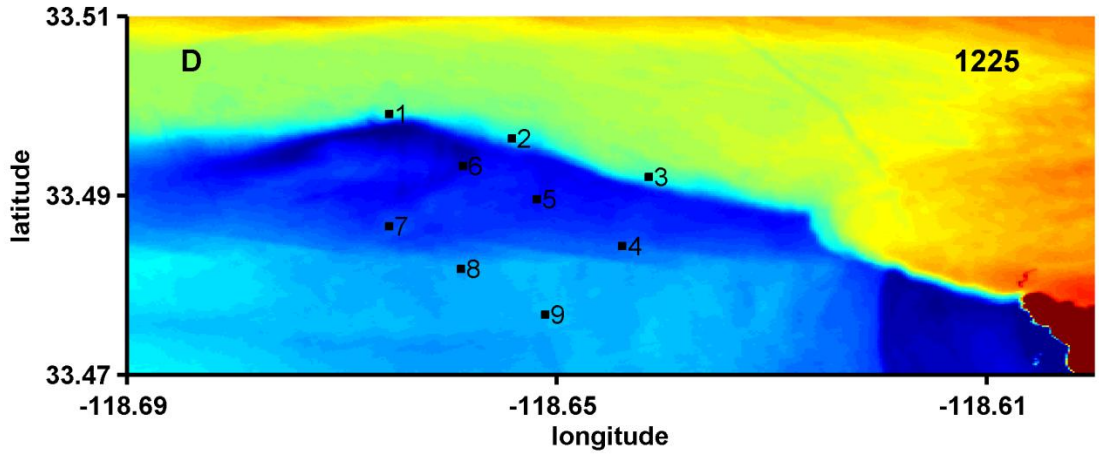
D
1225
1
2
3
4
5
6
7
8
9
33.51
33.49
33.47
latitude
-118.69
-118.65
-118.61
longitude

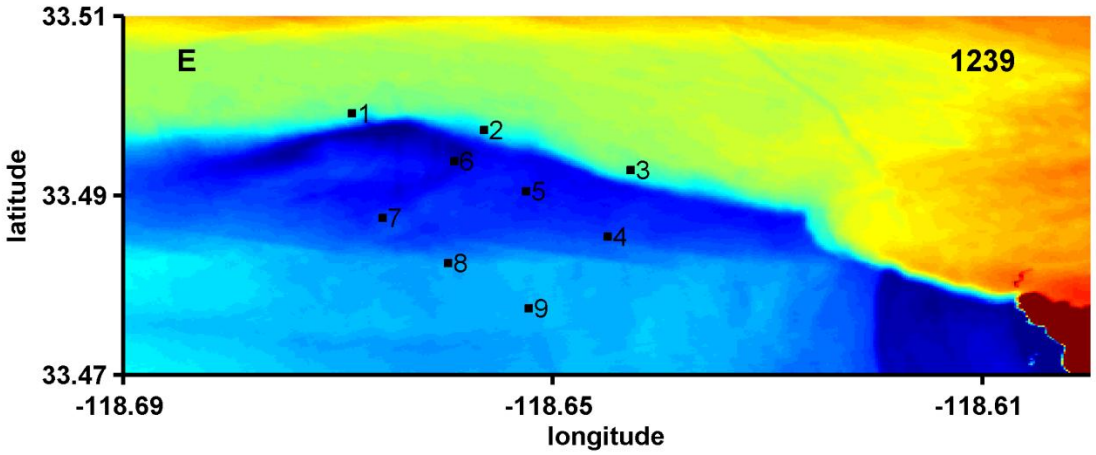
E
1239
1
2
3
4
5
6
7
8
9
33.51
33.49
33.47
latitude
-118.69
-118.65
-118.61
longitude

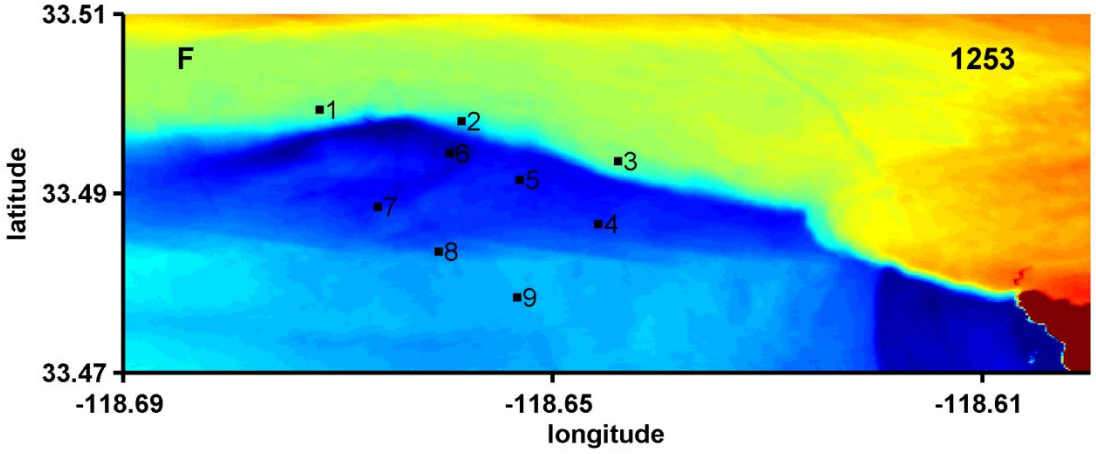
F
1253
1
2
3
4
5
6
7
8
9
33.51
33.49
33.47
latitude
-118.69
-118.65
-118.61
longitude

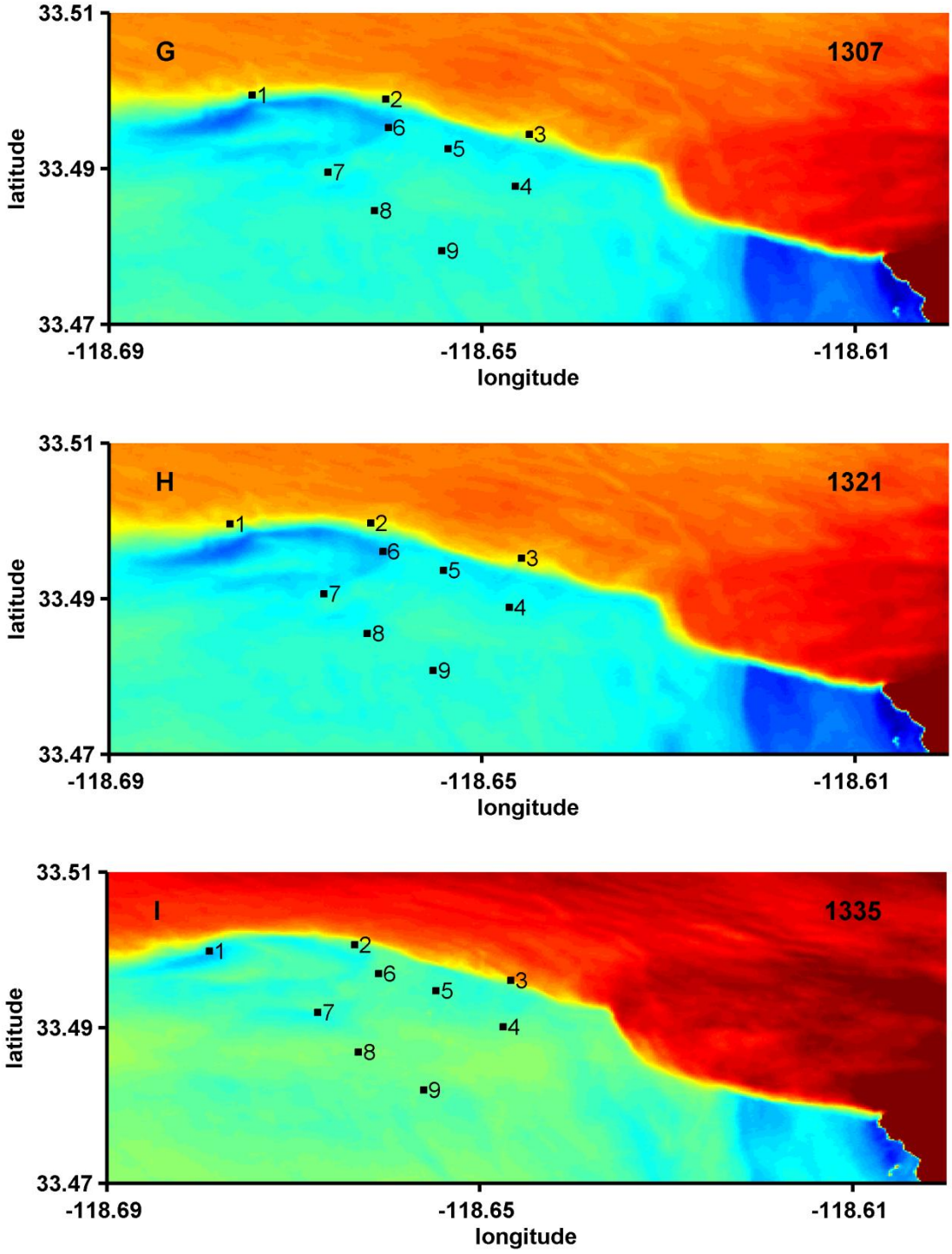

Figure 5.9: Drifter positions overlaid on corresponding IR SST image. The upper right number of each image is the time the drifter positions were taken. *Y* axis is latitude and *x* axis is longitude.

The time evolution of the front and drifter movement in figure 5.9 confirms the presence of confluent flow at the front. Drifter 1 approaches the front from the warm side, while drifters 2 and 3 approach from the cold side (fig 5.9 A-I). Once drifters 1-3 are entrained at the frontal interface, they remain predominately at the maximum of the temperature gradient. Further analysis of the drifter data (deployment was > 20 hours) shows a collapsing of the initial grid pattern into a line (indicative of confluent flow). In figure 5.9, the background SST are displayed to help visualize the location of the front relative to the drifters. The SST images are not updated at the same frequency as the drifter data. In panels A, D, F and G, and I the IR SST image is within 10 minutes of the drifter position.

The first image to definitively support that drifters 1-3 are at the maximum of the temperature gradient is at 1300 (definitive implying from raw data, not interpolated fields). Prior to 1300, drifters 1-3 are still converging on the front. At time 1300 and forward, the drifters are all on the cold side of the frontal interface ("cold side bias" – see Appendix C). At 1340 (the next coincidence of raw IR SST and drifter data) the cold side bias still exists (fig. 5.9 I and Appendix C). Drifter 2 is along the front and drifter 3 has moved to the warm side in a cold water intrusion, therefore still exhibiting a cold side bias. Interestingly, Drifter 1 is no longer entrained at the strong SST front, but instead along a secondary crescent shaped front (fig. 5.9, secondary front beginning at D). The cold crescent is not the maximum of the temperature gradient, but represents a localized region of an enhanced temperature gradient. The entrainment of drifter 1 along this front supports a secondary confluent/convergent flow behaving similar to the strong SST front.

A numerical modeling investigation of a surface density front confirms the cold side bias [Jeroen Molemaker, personal communication]. Drifters in the model align on the cold side of the front (fig. 5.10 and 5.11). This behavior is not witnessed on the warm side of the front.

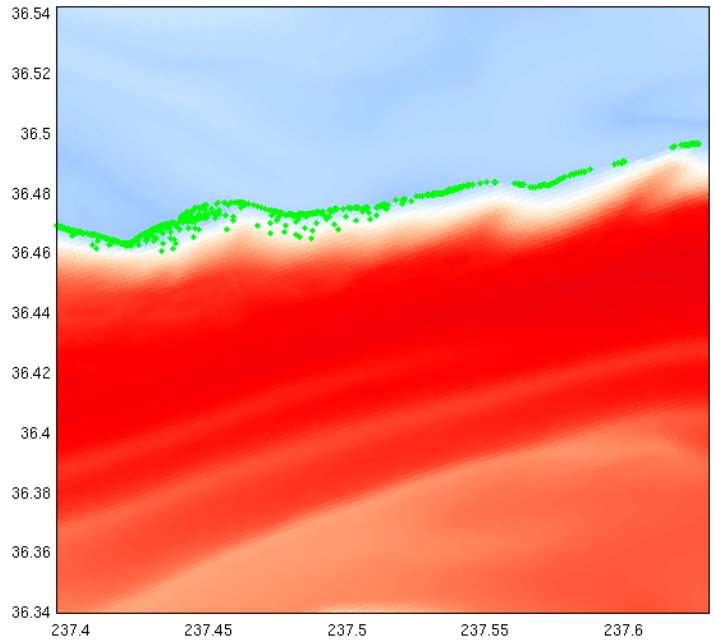

Figure 5.10: Image of surface temperature field. Blue is dense water and red is light water. The drifters are in green [Jeroen Molemaker, personal communication].

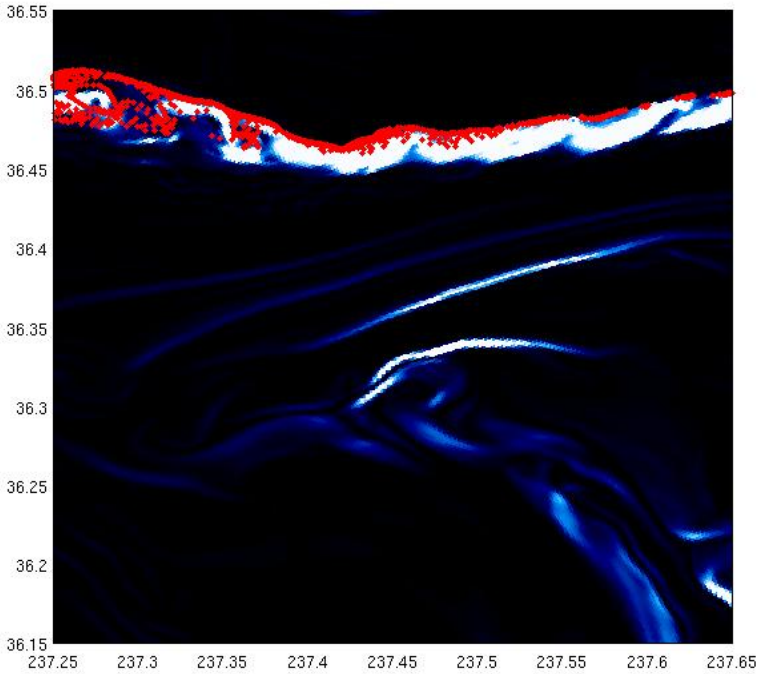

Figure 5.11: Absolute value of the temperature gradient (eq. 5.1) of the temperature field in figure 5.10. Drifters are in red. This confirms that drifters are on the cold side. The domain is larger than figure 5.10 [Jeroen Molemaker, personal communication].

The cold crescent may also influence drifters 6 and 7. Drifters 4-9 show little deformation of their initial grid spacing, but towards the end of the analysis time, the area bounded by drifters 5, 6 and 7 is compressed. The compression indicates a possible velocity change for drifters 6 and 7 relative to drifters 5, 8, and 9. This occurs when drifter 6 and 7 are at the edge of the cold crescent. Drifter 6 and 7 acceleration in the across-front direction (≈ north) of the primary front could explain the compression of the drifter spacing, as drifter 5 still moves towards the cold crescent (≈ northeast).

The observations of drifters 1, 6 and 7 in the presence of the cold crescent suggests that smaller scale, localized temperature gradients are also regions of convergence and capable of modifying the surface flow relative to the background deformation field. The generation of the secondary front is unknown. The prominence of the cold crescent supports that vertical

velocities are either refreshing the surface layer with dense/cold water (upwelling), or deepening the mixed layer (downwelling). Both of these effects would require more energy to heat the mixed layer bounded by the cold crescent to the temperature of the surrounding water..

To confirm the visually identified drifter movement from figure 5.9, including the northerly front advection, the drifter velocities were calculated from latitude/longitude coordinates by the first difference method. Drifter slip due to wind was not included in calculations (no wind data recorded). The drifter field was interpolated to a higher spatial resolution grid with *dx* of 186 m and *dy* of 222 m.

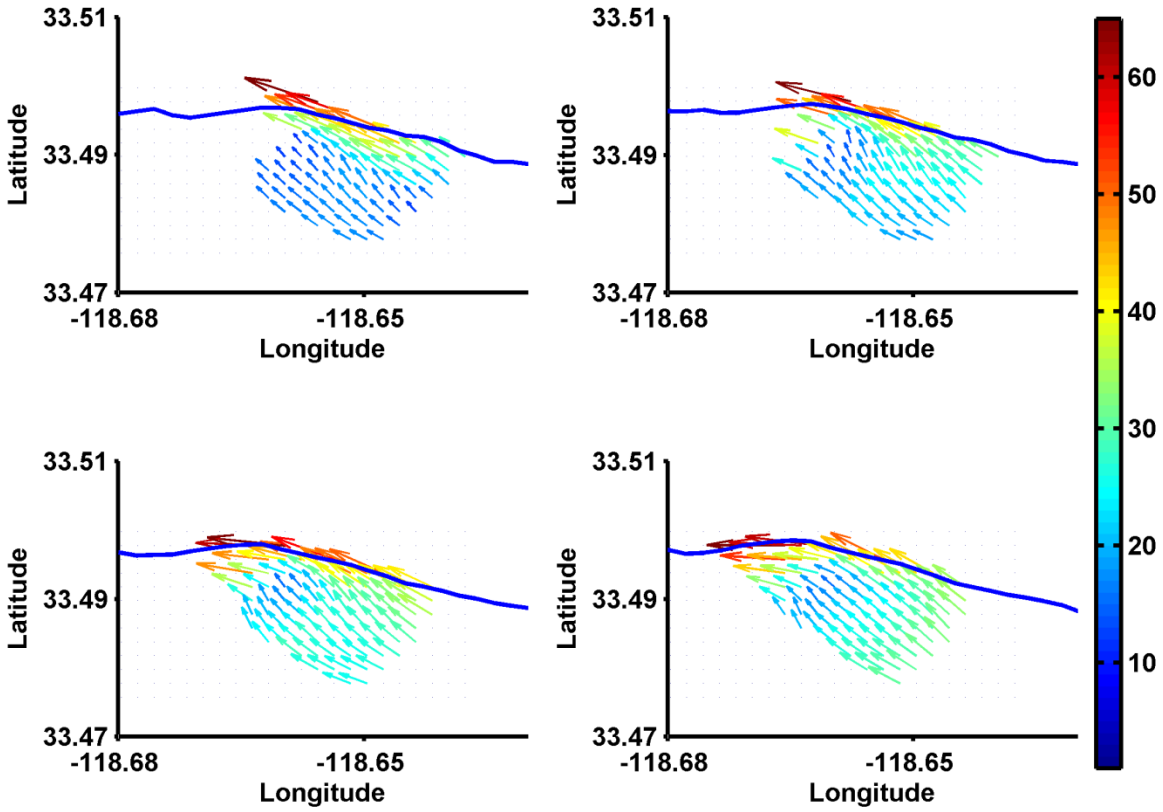

Figure 5.12: High resolution surface current field computed from the 9 drifter velocities. Image times are 1143, 1158, 1213, and 1228. Colorbar is in cm s^{-1}.

Near the front, there are elevated velocities > 50 cm s^{-1} directed primarily along the front in the down-front direction, indicating a near front intensified jet. The velocities progressively weaken away from the front approaching a near constant velocity with minimal accelerations (background deformation field). Drifter velocities have a maximal error of ± 2 cm s^{-1} due to position error. The mean zonal velocity of drifter 4-9 is 10 ± 2 cm s^{-1}, which confirms and sets the maximum rate for the northerly advection of the front as in figure 5.5.

To determine the extent of the along-front jet and surface flow relative to the front, the velocities computed from latitude and longitude coordinates are translated to a different coordinate system that accounts for front curvature and advection.

5.5 Coordinate system

To account for the front curvature, all along-front and across-front motion is taken relative to the instantaneous slope of the front at the position on the front nearest the measurement location. A line from the measurement location to the nearest position on the front is hereinafter the *minimum distance line*, or *MDL*. The *MDL* is normal to the front (similar to the radius line from the center of a circle to the edge). Motion parallel to an *MDL* is across-front motion designated by $\boldsymbol{u}$, with negative motion against the surface buoyancy gradient - i.e. negative motion is from light to dense water at the surface.

For along-front motion, the velocity vector computed from latitude/longitude coordinates is projected to a line normal to the *MDL*. Along-front motion is designated by $\boldsymbol{v}$, where down-front motion in the direction of the jet at the frontal interface is the positive v direction –i.e. dense water to the left and light water to the right of the direction of motion.

The 3D position is given by x, y, and z being the across-front, along-front, and depth axis respectively. The dense side of the front corresponds to $-x$ with the front being 0. The y coordinate is 0 at the west end of Catalina Island (considered the origin of the front) and increasingly positive moving down-front away from Catalina Island. The negative y direction is excluded. Depth (z) is from 0 m at the surface to negative values at depth.

Due to the slight curvature of the front, this coordinate system is similar to the curvilinear coordinate system presented by Hoskins and Bretherton (1972) for their analysis of a near straight front [*Hoskins and Bretherton*, 1972]. The main difference is that the coordinate system in this thesis moves with the front and is accurate in the presence of small, but sharp distortions of the front.

5.5.1 Along-front Velocities Derived From Drifter Data

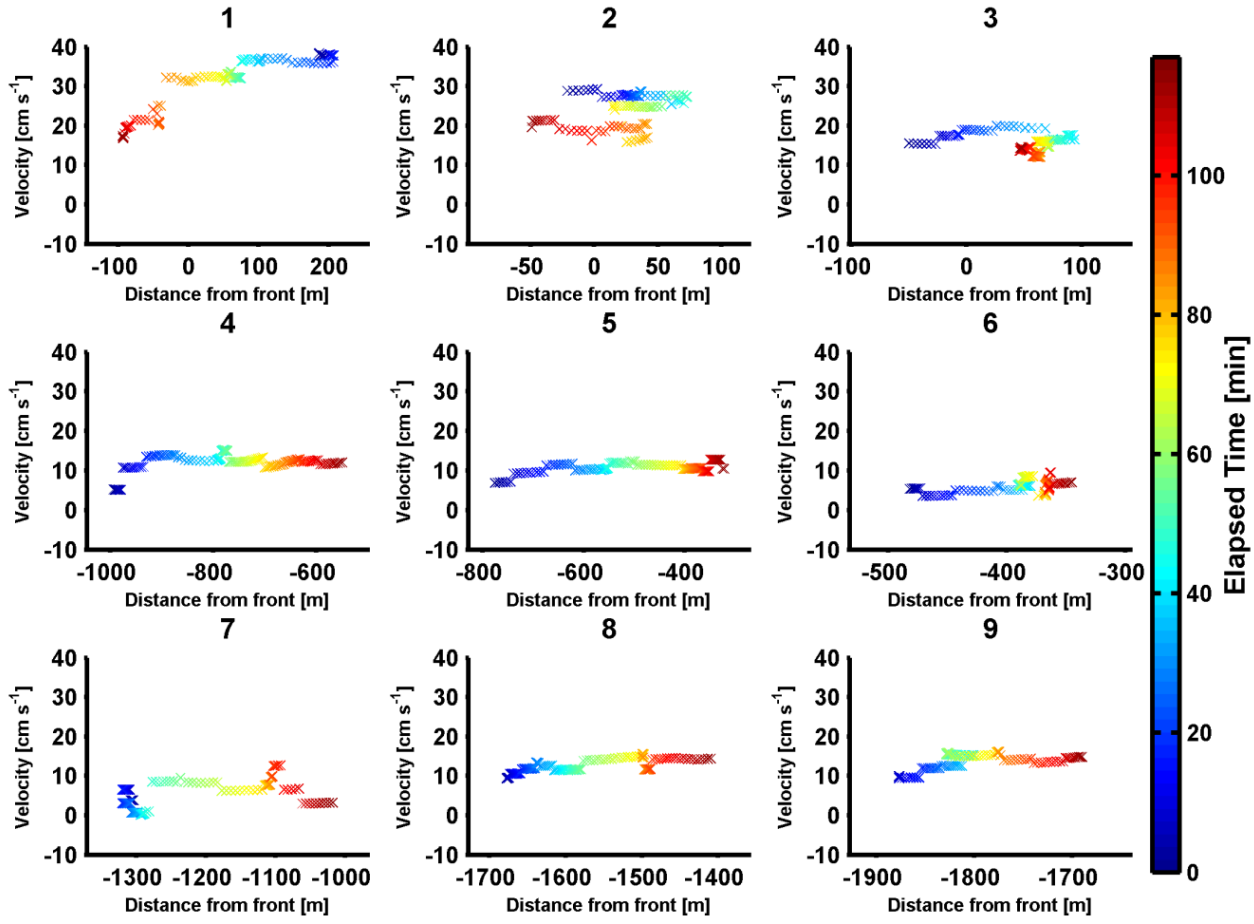

Figure 5.13: Along-front motion of the 9 deployed *Drifters*. The number of each sub image is the drifter number (fig. 5.9 A). The colorbar indicates the total elapsed time from deployment (bounded by the SST image times). The *x* axis is orthogonal distance to the front (*MDL*) and the *y* axis is the along-front velocity (cm s^{-1}).

The along-front velocities confirm the presence of the frontal jet. The mean velocity of drifters 1-3 is 24 ± 2 cm s^{-1}, relative to the background deformation flow (4-9) at 10 ± 2 cm s^{-1}. Drifter 1 indicates that the jet extends to both sides of the frontal interface and is stronger on the warm side. The jet extends from 200 m on the warm side to 100-300 m into the cold side. The maximum distance boundary for the jet on the cold side is 300 m, as drifter 6 does not show any elevated along-front velocities relative to the background deformation field. In addition, as

drifter 1 moves away from the strong SST front on the cold side, the along-front velocity decreases rapidly with increasing distance. The jet may extend past 200 m on the warm side, but no drifter data exists.

The true extent of the jet is not well captured by the low resolution drifter field, or mapping error of order 50 m. Drifters 2 and 3 reside at a distance from the interpolated front position that is within the mapping error. Consequently, they do not validate the horizontal extent of the frontal jet, but they do provide accurate velocities.

The along-front circulation of the cold crescent may also be captured by the along-front circulation of the primary front due to the cold crescent orientation (fig. 5.9 for cold crescent and fig. 5.13 for along-front velocity). The velocity of drifter 1 decreases at the end of the time vector (fig 5.13) when it is located at the cold crescent (fig 5.9 Panel I). Meanwhile the cold crescent along-front acceleration of drifters 6 and 7 is oriented such that the along-front velocity relative to the primary front should decrease. The cold crescent has weaker temperature gradients and therefore weaker associated circulations if any degree of thermal wind balance exists (eq 1.13 and 1.14).

Drifter along-front velocities depend on drifter position accuracy and to a minimal degree on front position. The front position is used for angle calculations to project the absolute drifter velocities to the along-front direction (normal to the *MDL*). During analysis, it was noticed that angle calculations have large errors when the distance approaches zero. Near the frontal interface, the *MDL* becomes increasingly parallel (i.e. the angle of intersection shallows) to the frontal slope if the front position resolution is poor.

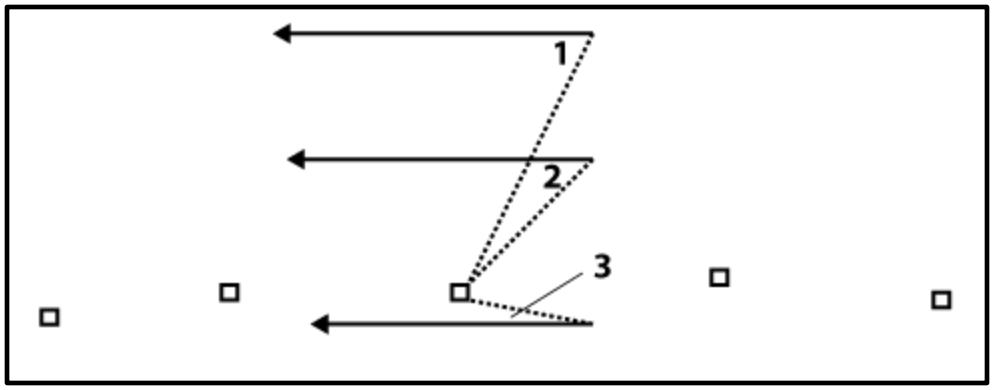

Figure 5.14: Solid lines are the velocity vectors with the measurement position at the tail of the vector. Squares are the front positions and the dashed lines are *MDLs*. Numbers 1-3 are the angle of intersection between the drifter velocity vector and *MDL*. The angle decreases as the drifter approaches the front.

The azimuthal heading of any drifter with strong along-front motion is now aligned with the *MDL* and the angle difference is zero. From the above definition, along-front motion is perpendicular to the *MDL*, so the projected velocity is forced to 0 cm s^{-1} when taking cosine of 90°. This can be circumnavigated by increasing front resolution. Tests indicated that large increases in resolution reduced the error, but at high computational costs. Considering only a few points exhibit this error, a secondary routine can be established when the drifter to front distance crosses a threshold value (< 100 m).

In the secondary routine the *MDL* is neglected. Instead, the difference between the drifter heading and mean frontal slope (in degrees) taken where the *MDL* would intersect the front is computed. The drifter velocity is then projected to the mean frontal slope. This would provide a more robust projection of the drifter velocity in standard coordinates to the front coordinates. This method will work best when the front exhibits weak curvature and infrequent, or subtle intrusions. Further investigation of the secondary method is necessary. Tests were not conducted because it is not relevant to the *SubEx* front.

Aside from the projection error, the maximum velocity error is then ± 2 cm s^{-1} as it was in standard coordinates.

5.5.2 Across-front Velocities Derived From Drifter Data

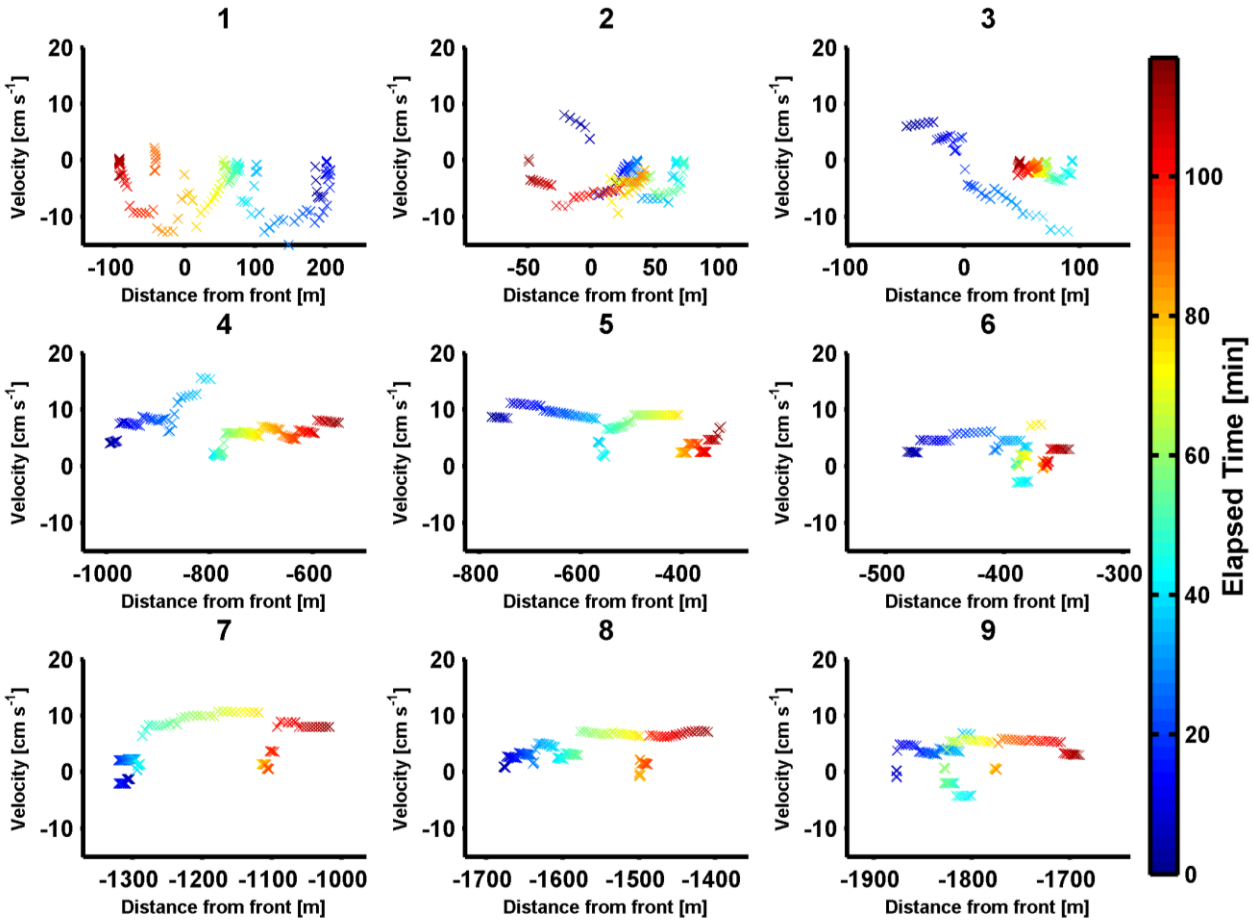

Figure 5.15: Across-front motion of the 9 deployed *Drifters*. The corresponding numbers of each sub image is the drifter number (fig. 5.9 A). The colorbar indicates the total elapsed time from deployment (bounded by the SST image times). The *x* axis is orthogonal distance to the front (*MDL*) and the *y* axis is the along-front velocity (cm s^{-1}).

Unlike the along-front velocities, the across-front velocities are more susceptible to errors in the front position because the across-front velocities are calculated from *MDL* length changes in the first difference method.

$$u = MDL_{t_o} - MDL_{t_o+\Delta t} \tag{5.2}$$

The across-front velocity (u) is the difference in the length of the *MDL* at time now (MDL_{t_o}) and the length of the *MDL* at the next time in the future ($MDL_{t_o+\Delta t}$), where the time increment (Δt) is 1 minute.

The across-front velocity error is primarily from the interpolation of the 4 front positions. To overcome occurrences of sharp and unnatural movements of the front resulting from interpolation, the 4 front latitude positions were plotted as a function of time (longitude positions are constant values between images – fig.5.3) and a second order polynomial was fitted to the data. The results of the fit were then interpolated to the 1 minute interval time vector. This was an attempt to provide a more "robust" front position. The results smoothed the transition between front positions, but the results poorly represented the observed front positions because the polynomial was not forced to pass through the start and end points. Forcing the polynomial to pass through the start and end points also yielded equally poor results. The error is not in the coordinate system, but due to the low frequency mapping of the front. Recommendations to increase temporal coverage of front are discussed in section 6.1.

Another error in across-front velocity results from an artificial rotation of the front during aerial measurements. The northward advection of the front is of *O*(10) cm s^{-1} as derived from drifter velocities (and CODAR). In an IR SST mapping that begins at the west end of Catalina Island, the western portion of the front is mapped approximately 30-35 minutes later. In this time, the western portion has been advected roughly 100-200 m. This rotation occurs each measurement. Fortunately, the "back and forth" method of mapping, in which flight paths intersect the front (not along it) in an S-shaped pattern were conducted in the same manner for

each SST map. With the exception of the first SST map (fig. 5.3 A), the first image of each map occurred at the tip of Catalina Island and the last image at the western edge of the front. Therefore, the artificial rotation of the front that arises from assuming the front image represents a single time and then interpolating to a higher resolution time vector is nullified - i.e. since the rotation is consistent, it does not induce large error in the across-front velocity.

The main error is then attributed to the *MDL* length error, which is directly related to front position error of *O*(25-50) m. This results in a ± 5 cm s^{-1} across-front velocity error. The interpolation produced error is evident in figure 5.15 (drifter 1), noted by the rapid decelerations from ≈ 10 cm s^{-1} to 0 cm s^{-1}. Methods to reduce this error will be discussed in the conclusion section. In light of these errors, a brief analysis of across-front velocities will be made.

The motion of drifters 4-9 is still consistent with a background deformation flow. Drifter 1 has a negative mean velocity, consistent with down gradient motion from warm to cold side towards the cold crescent. Drifters 2 and 3 are once again within the domain of the mapping error and it is unlikely that they travel from the cold side of the front to the warm side, as they never reside on the warm side in figure 5.9.

5.6 Geostrophic Velocities

The along-front current direction and elevated velocity is consistent with gradient wind balance. Therefore, geostrophic theory and thermal wind balance were used to calculate the subsurface currents using the IR SST and surface drifter data. The surface drifter data provided a level of known motion for the integration of vertical shear of horizontal velocity. This is similar to the standard procedure of integrating upward from a depth at which a "level of *no* motion" is defined.

The smoothed 2D *in situ* temperature field was converted to buoyancy (*b*, from eq. 2.5) and equated to the vertical shear of horizontal velocity ($\frac{\partial v_g}{\partial z}$) (see section 1.1 for thermal wind equations), where $\frac{\partial b}{\partial x}$ is the horizontal buoyancy gradient and *f* is the Coriolis force.

$$\frac{\partial v_g}{\partial z} = -\frac{\partial b}{\partial x}/f \tag{5.3}$$

The buoyancy fields were made orthogonal to the front and interpolated to a common distance vector. The vertical shear of horizontal velocity (eq. 5.3) field on the common distance vector was then interpolated to the high resolution surface drifter field and integrated from the surface down. The subsurface integrated velocities were projected to the along-front direction in the same fashion as the surface drifters.

Due to incomplete filtering of the internal gravity waves by the low pass Gaussian filters, horizontal density anomalies remain that lead to currents when geostrophic balance is assumed. Since the remnants of internal gravity waves are not fully removed, these currents are considered "artifact".

Between transects, the locations of the artifact currents and center to center distance (independent of vessel rate or heading) vary, therefore supporting that feature is a propagating signal. Referring to section 3, the isopycnal displacement from internal gravity waves change the density distribution resulting in subsurface currents from the integration of vertical shear of horizontal velocity (eq. 1.13 and 1.14).

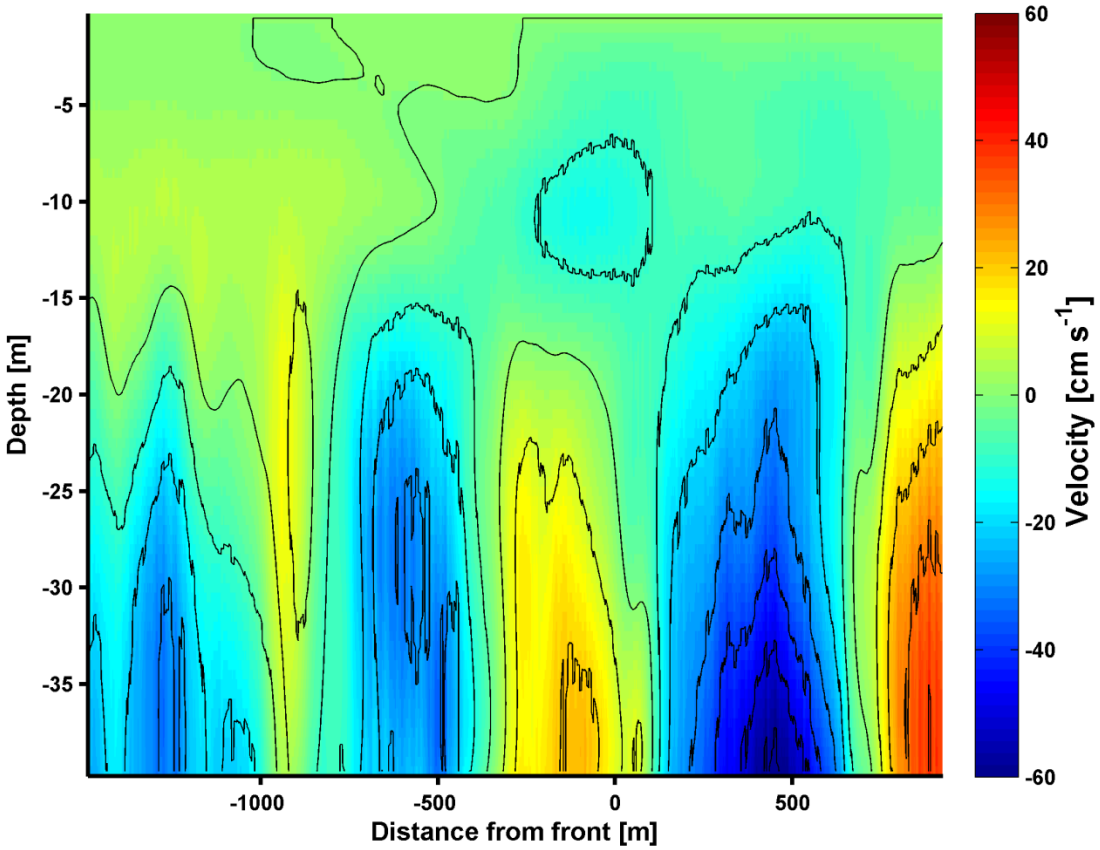

Figure 5.16: Typical example of internal gravity wave artifact in the geostrophic velocity field. The integration is performed from the surface down without the surface drifter velocities to emphasize the magnitude of the current artifact. Between 0 and 500 m (warm side) the larger velocities are attributed to a combination of internal gravity waves and the front. Contours are at 10 cm s^{-1} intervals.

Figure 5.16 is a typical example of the geostrophic currents after integration. To emphasize the magnitude of internal gravity waves on geostrophic currents, the integration of the vertical shear of horizontal velocity is performed without the surface drifter velocities (fig. 5.16). At positions away from the front, where temperatures are more constant (without the front influencing the temperature field), the internal gravity waves present a false current that is approximately 30 ± 10 cm s^{-1}.

All transect geostrophic calculations showed a strong internal gravity wave signature manifested as artifact in the geostrophic currents.

5.7 Internal Gravity Waves

The presence of internal gravity waves conceals the frontal dynamics that result from the density gradients independent of the internal gravity waves. This does not mean that the internal gravity waves are not dynamically relevant for submesoscale fronts. However, with respect to geostrophic current calculations the wave signal must be removed.

The high variability of the internal gravity wave signal suggests the field is polychromatic - i.e. composed of waves with different wavelengths and emanating from different sources. Due to our measurement technique, it will be extremely hard, if not impossible to fully discretize the internal gravity wave field and filter them out. Understanding the internal gravity wave field would take 3 sufficiently separated static measurements at a common time, which were not made during *SubEx* [*Defant*, 1950].

We have already seen that the gravity waves contribute significantly to artifact in geostrophic currents (fig. 5.16), but to assess the degree of impact from the internal gravity waves per depth level the variance of the temperature field in time was calculated. The variance of the temperature field is synonymous with density variance in our mean salinity case.

The variance (s'^2) of the data at a constant depth level is given by

$$s'^2 = \frac{1}{n}\sum_{i=1}^{n}(x_i - \bar{x})^2 \tag{5.4}$$

where the variance is the cumulative sum of the squared difference of each individual measurement (x_i) and the mean of the population ($\bar{x}$). In this case, the population constitutes the combination of individual measurements contributed from each transect at a specified (x,z) position.

The temperature variance would be affected by both internal gravity waves and the front if the variance was not taken as a function of time. By computing the variance in time for fixed positions, we eliminate the front's contribution to variance because the coordinate system has fixed the front's position in time. The front will increase the variance to a minor degree due to:

1. Changing physical properties of the front, such as temperature and frontal slope due to the front's evolution resulting from circulation (ex. confluent deformation flow, and/or ageostrophic circulation) and external forcings (ex. wind forcing, and/or heating by the atmosphere).

2. Averaging transects separated in space. Different positions along the front may have different characteristics. The variance contribution of this factor is indistinguishable from factor 1.

3. Position errors of the front that result when converting transect data to be orthogonal to the front.

These 3 factors will elevate the variance only in the vicinity of the front (i.e. horizontal distances from $x = -100$ m to the horizontal extent of the front on the warm side and at depths less than 10 m).

Conversely, the variance associated with internal gravity waves will not be eliminated because the waves vary in space and time relative to the front as they propagate at different speeds and directions than the front. The internal gravity wave perturbations should be of similar magnitude per depth level because they depend on the stratification (section 3). The thermocline will always have the largest variance because the internal gravity waves are propagating in a region of elevated vertical temperature gradient and will therefore have the largest affect.

The temperature variance in time was calculated at each depth level at horizontal distances from 800 m on the cold side to 100 m on the warm side in 100 m increments.

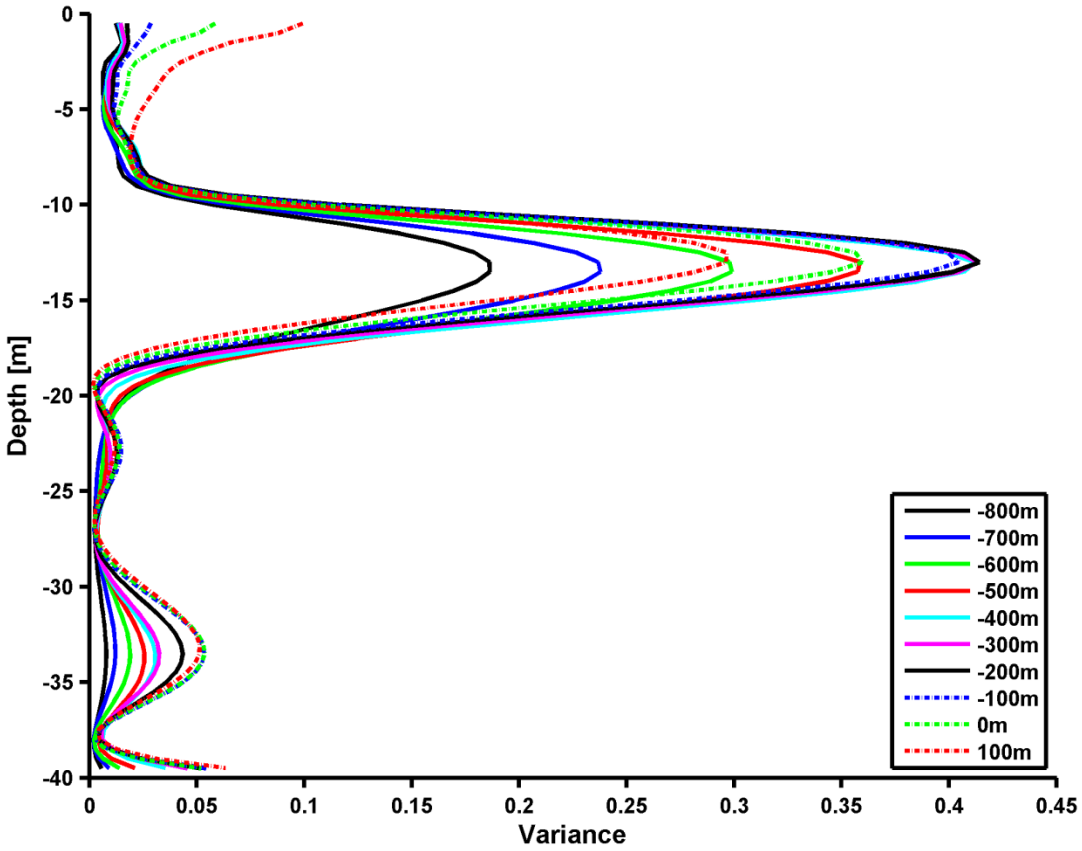

Figure 5.17: Temperature variance in time per horizontal distance at each depth.

The results (fig. 5.17) show the largest variance between 11-16 m depth with a maximum at 14 m depth for all distances. This is consistent with the maximum perturbations expected at the thermocline (fig. 5.7 and 5.18). We note that the variance at 10-15 m depth near the front is similar to positions far away from the front (fig. 5.17 green and dashed red lines corresponding to -600 m and 100 m respectively) and is therefore independent of the front. Near the surface, the highest variance values are associated with -100, 0, and 100 m. Clearly there is some contribution of the front to the variance in this region. As per above points 1-3, we are unable to determine which factor is contributing to the variance.

Since the internal gravity wave signal is strong below 10 m depth, all geostrophic velocity calculations will be limited to the upper 10 m of the water column. Unfortunately, the variance attributed to the front will also need to be reduced to improve geostrophic calculations.

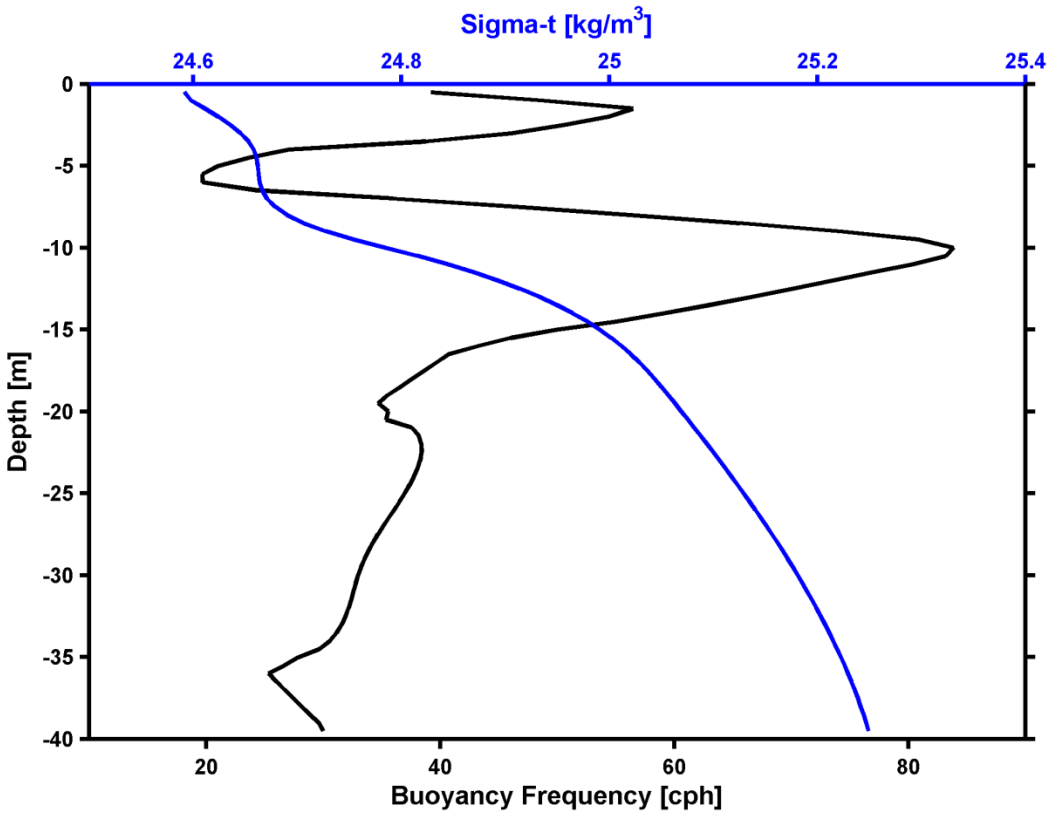

Figure 5.18: buoyancy frequency and density per depth level.

Figure 5.18 confirms the presence of the thermocline (pycnocline) at 8-10 m depth. The highest frequency waves also exist where the buoyancy frequency peaks at 10 m depth (fig 5.17, section 3 for *N*).

Since the waves are randomly distributed in space with respect to the front, we hypothesize that averaging should result in a decrease of the internal gravity wave signature. The averaging will reduce the front associated velocities to a lesser degree because the coordinate system has fixed the front in space and the general shape of the front is similar among transects. Also, approaching the surface where the front is the strongest, the internal gravity wave perturbations go to zero, since the surface displacement is minimal [*Hautala et al*., 2005]. The weaker temperature gradient (relative to the thermocline) also means that internal gravity wave

perturbations have a smaller effect on the redistribution of temperature. These two characteristics compound the weakening of the internal gravity wave signal and produce a dominant SST front signal near 0 m in *x* and at depths < 10 m.

The reduction in variance of the internal gravity waves when averaging transects together should follow a $\frac{1}{\sqrt{n}}$ scaling as detailed in equations 5.5-5.8 below. When taking the sum of *n* number of measurements (eq. 5.5), the associated error (*errx*) increases by $\sqrt{n}$ (eq. 5.6) [*Wolfram Research*, accessed 2012].

$$\sum_{1}^{n} x = x_1 + x_2 + \cdots x_{n-1} + x_n \tag{5.5}$$

$$\Delta\left(\sum x\right) = \sqrt{errx_1^2 + errx_2^2 + \cdots + errx_{n-1}^2 + errx_n^2} = \sqrt{n} * errx \tag{5.6}$$

This assumes that the error of each measurement is consistent. From figure 5.17, our internal gravity wave associated error is dependent on location. In the limit that the number of transects goes to infinity (or some realistic value of observations to develop a better statistical set), the variance in time (fig. 5.17) would be independent of horizontal distance and approach a constant value.

It then follows that

$$\frac{\Delta\bar{x}}{\bar{x}} = \frac{\Delta(\sum x)}{\sum x} \rightarrow \Delta\bar{x} = \frac{errx}{\sqrt{n}} \tag{5.7}$$

where the mean ($\bar{x}$) is

$$\bar{x} = \frac{\sum x}{n} \tag{5.8}$$

The solution to equation 5.7 is known as the standard error of the sample mean ($\Delta\bar{x}$), which in our case is from the internal gravity waves [*Wolfram Research*, accessed 2012].

The minimal overlap of transects when plotted as a function of distance from the front (and interpolated to a common distance vector) and the reduction in length due to the filter width, resulted in 4 usable transects for averaging. At most, the internal gravity wave signal can be reduced by an estimated 50%. From the false geostrophic currents displayed in figure 5.16, a 50% reduction would still have residual artifact currents of $O(15 \pm 5)$ cm s^{-1}. A 50% reduction is also improbable, albeit theoretically possible, due to the small statistical set. No plots are included because the 4 transects minimal overlap with the drifter field further reduced the available data to average and integrate from the surface down. Little can be said with respect to internal gravity wave reduction. We do note that similar to figure 5.16, in all transects (before averaging) at distances between 0 and 500 m on the warm side there are stronger geostrophic velocities due to the combination of internal gravity waves and the front. Hopefully after averaging (assuming better data overlap during the next experiment), the front will be the dominant signal contributing to geostrophic currents.

The implementation of transect averaging is a likely candidate for reduction in the internal gravity wave signal, but the method hinges on a more regimented sampling method. Our results do not show its full potential. Recommendations for improving overall efficiency and producing more usable transects are detailed in section 6.1.

CHAPTER 6

Conclusions

The measurement technique detailed in this thesis successfully detected several submesoscale features including straight fronts, cold/warm core eddies, and filaments. The spatial-temporal resolution of aerial images are of O(25-50) m and O(30) minutes per 150 km^2 respectively. The *in situ* horizontal and vertical resolutions are of O(5) m and of O(< 7) m respectively with a sampling frequency of 1 Hz.

The two orbiting aircraft guided research vessels to a strong SST front on April 14, 2011. The aircraft provided reliable georeferenced maps that allowed for the vessels to measure the front as it was advected at rates of O(10) cm s^{-1}. The location and temperature change across the front as determined by the IR cameras and *in situ* temperature sensors is well correlated. The approach also succeeds where conventional observational platforms do not. Frontal dynamics were extracted even with the complicated, if not "contaminated" signal due to the presence of internal gravity waves. In total, there were 4 complete SST maps covering 600 km^2, 19 *in situ* transects for a total distance of 38 km at 3.8 m s^{-1}, and the deployment of 14 drifters directly in the vicinity of the front within a 2.5 hour time span.

The measured submesoscale SST front is weakly curved and occupies a 6.5x1.97 km domain to the west and north of Catalina Island's West End. Cold, dense water is to the south of the frontal interface. The dense water undercuts the lighter water with a slope of 0.0146. The maximum of the surface horizontal temperature gradient is 0.0031℃. The maximum of the

vertical temperature gradient is 0.282°C at 10 m depth indicating a thermocline (fig. 5.7 and 5.18).

The front is undergoing frontogenesis in the presence of a confluent background deformation field confirmed by the drifters. The surface confluence zone has a cold side bias - i.e. the confluent zone does not reside directly over the maximum of the horizontal temperature gradient (see Appendix C) . There is an along-front jet oriented in the down-front direction on both sides of the frontal interface with larger velocities on the warm side. The mean jet velocity is 23 ± 2 cm s^{-1}. There is also a secondary cold front that develops in the presence of the primary front. The data was inconclusive with respect to geostrophic velocities at the secondary front, but the movement of the drifters suggest that it may be a localized convergence zone. The origin of the feature is unknown, but as a localized cold region, it is probable that there are vertical velocities either (1) downwelling and deepening the mixed layer, or (2) upwelling and introducing cold subsurface waters. Both conditions would require more atmospheric heating, hence the persistent cold signature.

The subsurface dynamics were contaminated by internal gravity waves. The strongest internal gravity waves exist at the thermocline as theory predicts (fig. 5.17). It is here that they have the strongest perturbation amplitude of O(0.2-0.4)°C. There is not enough overlapping data to sufficiently reduce the internal gravity waves and comment on subsurface dynamics. At most, the internal gravity wave artifact can be reduced by 50% with the available data, but general spatial overlap is poor.

The approach detailed in this thesis represents one stage in the evolution of a promising technique that can measure sharp, small scale density features. With small changes to

deployment procedure, the full capabilities of the method will be realized. The improved efficiency will provide a better spatial-temporal overlap of data sets to aid in the reduction of internal gravity wave artifact and allow for 2-3 deployments per day to more thoroughly measure a submesoscale feature through its generation and development.

6.1 Recommendations

The analysis was limited by the lack of data overlap. Each individual platform performed well, but to develop an overall understanding of submesoscale circulations and overcome individual platform limitations, a synergistic combination of the data sets is required. For example, of the 19 transects, only 10 crossed the front and only 7 during the time that there was IR SST data. There were only 4 usable transects when integrating the velocity shear from the surface velocity profile obtained by the drifters. Most of the weaknesses were previously mentioned throughout the results section and will only be summarized in the recommendations. The recommendations provided here do not include the unsophisticated addition of more resources, but describe new methods using the available infrastructure.

Here I propose a method to better sample a submesoscale front with weak curvature. Adaptations and improvements of this method are encouraged and necessary for the method to evolve and be used in other circumstances, such as eddies and curved fronts.

The main point is specificity. All resources must be tasked with measuring a specific feature (ex. the surface density front) and even a specific set of dynamics (ex. high resolution for the frontal jet and low resolution for the deformation field). For each platform, I suggest the following:

6.1.1 Aerial Measurements

The aircraft will continue to play a vital role in locating the front and transmitting images to the vessels. The aircraft images can be supplemented by MODIS SST and chlorophyll, but we have seen that these two sources are not reliable and care should be taken in evaluating what dynamics are present (mesoscale deformation and frontogenesis, or Ekman coastal upwelling). MODIS also provides 250 m and 500 m resolution images in the visible light spectrum. Although not all density features will be visually identifiable, some features may due to accumulation of surfactants, or other material. For example, the cold region bounded by box 2 in figure 6.2 has a visible signature in the MODIS 250-500 m resolution visible spectrum images. Plumes developing from runoff, or industrial outflow may have also have cues in the visible light spectrum. As such, MODIS visible light spectrum images should be included in pre-measurement planning.

The front position spatial accuracy and mapping frequency must also be improved. Although the IR SST images are accurate to 25-50 m, more error is introduced due to the slow update frequency. Current flight patterns update front position every 35 minutes for a 125-150 km^2 map when < 30 km^2 are needed to overlap the other data. Decreasing the mapping area, while still adequately mapping the front can be accomplished by mapping along the front, rather than in the "back and forth" method currently employed. A 6.5 km long front mapped along the front will take < 5 minutes (at the current cruising speed). This is a 7 fold increase in temporal resolution compared to current mapping intervals. The spatial resolution will remain constant, but a 2.6 km swath provides adequate coverage of the front with 1.3 km of mapped SST per side. The

increased temporal resolution will significantly decrease the artificial rotation of the front and more importantly, decrease the error associated with interpolating the front position.

Decreasing measurement altitude is not recommended because more flight tracks will be required to provide a description of the area in the vicinity of the front where the vessel is making transects (lower altitudes will require 2-3 along-front flights to map a sufficient area, thereby increasing the time upwards of 10-15 minutes per map).

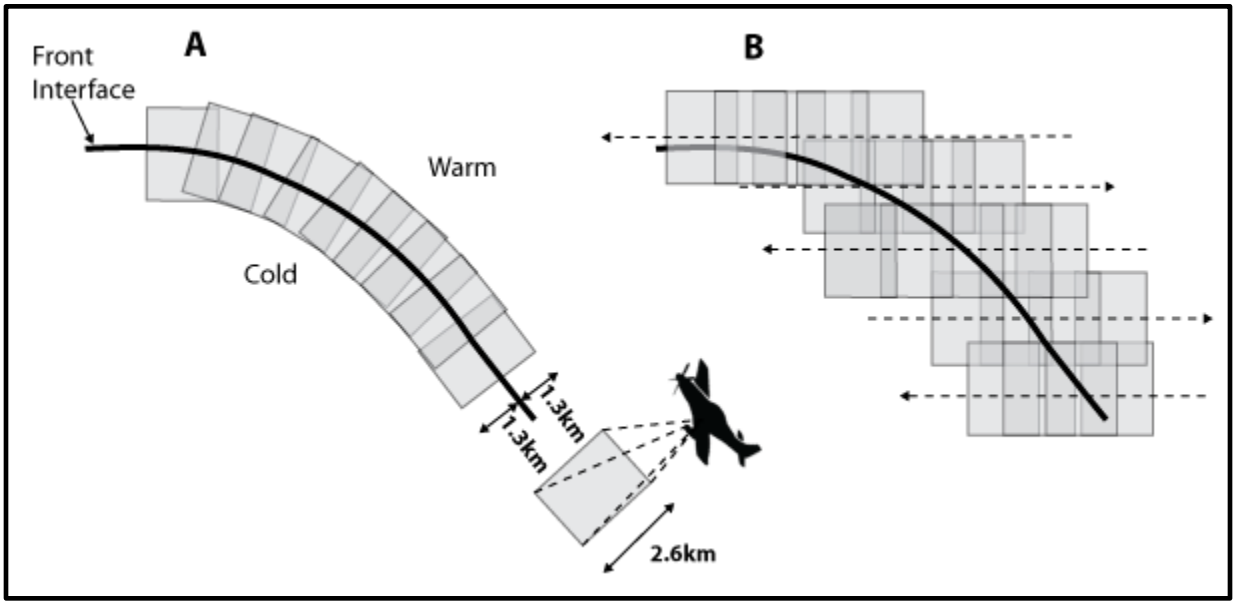

Figure 6.1: A) New method of mapping along the front. B) Current mapping method of "back and forth" flight tracks (dashed lines).

Also, camera tests should be performed to determine how images are affected by changes in orientation of the aircraft. Orientation changes affect the magnetic field that the MTiG uses for inertial measurements and the varying sun angles cause differential heating of the camera lens. These errors are not random variance, but of consistent amplitude and bias (fig. 6.2, box 1).

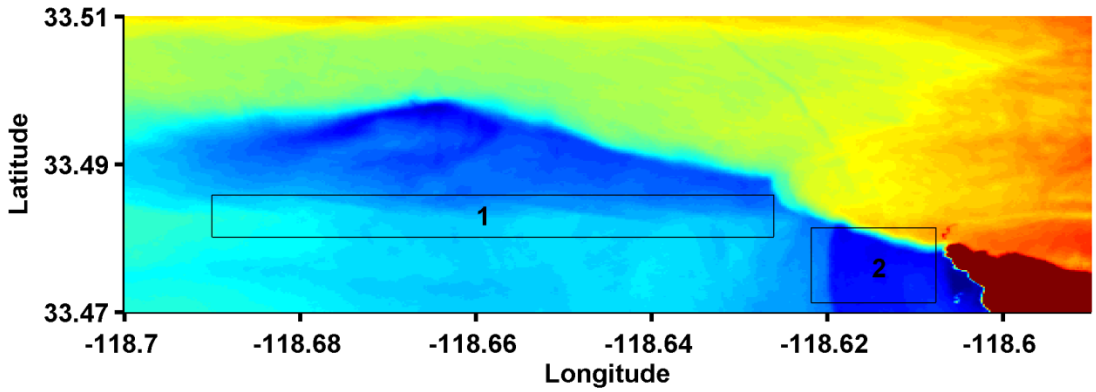

Figure 6.2: The area labeled 1 is error associated with the camera and mapping. In the region bounded by box 1, two tracks of different headings are overlaid, creating an artificial gradient. The region bounded by box 2 is not error (confirmed by MODIS visible light images) [MODIS image available at *http://www.rapidfire.sci.gsfc.nasa.gov*].

Following these increases to temporal resolution, surface current velocities should be determined using Particle Image Velocimetry (PIV). PIV compares kernels between images and computes the location on the second image that most resembles the kernel from the first image. The displacement of the kernel is the surface velocity vector. Previous PIV solutions produced erratic velocity vectors due to poor correlation values that arose from large amounts of distortion between images with large time jumps. PIV toolboxes are available add-ons to MATLAB.

6.1.2 *In situ* measurements

Drifters: Paramount to understanding the surface velocity fields near the front is drifter deployment. Drifters *must* be deployed on both sides of the front. Results indicate that the frontal jet is concentrated near the front and the remainder of the mapped area represents a background deformation field (section 5.4 and 5.5). Therefore, drifters can be deployed closer to the front with smaller grid spacing in the across-front direction to determine the extent of the jet. The box grid deployment does well to capture both the frontal jet and background deformation

field. The drifter containing the ADCP should be placed directly at the frontal interface. Here it will record the location of vertical velocities. If a cold side bias exists, the ADCP drifter will be present in the surface convergence zone and confirm that downwelling exists on the cold side of the maximum of the temperature gradient. ADCP data will also be affected by internal gravity waves, but they will be reduced by averaging in time.

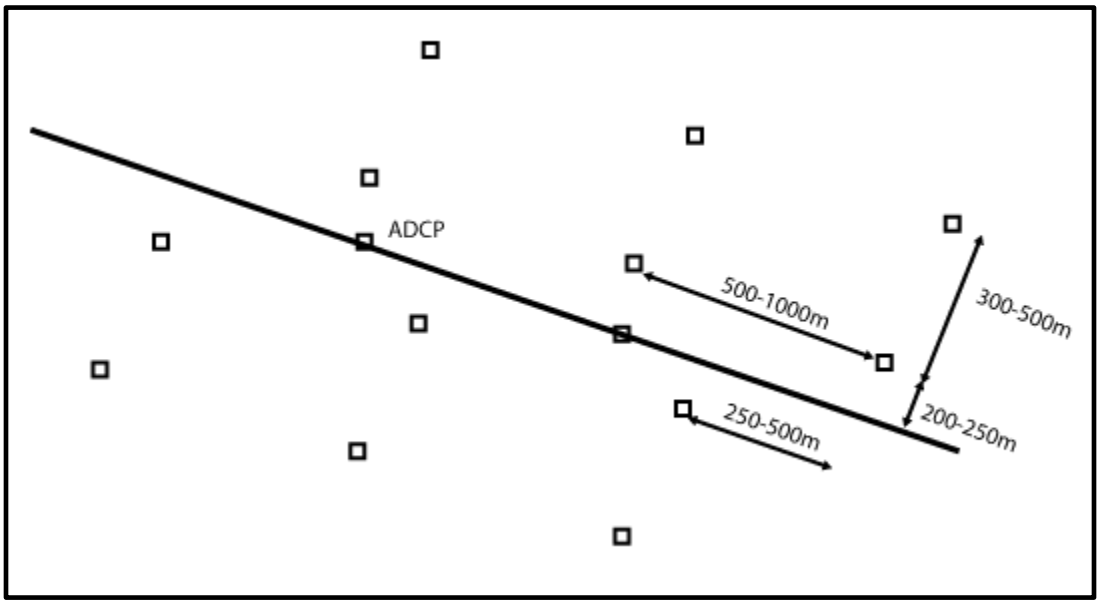

Figure 6.3: Drifter configuration for measuring a straight/weakly curved front. 14 drifters are deployed in a staggered box grid configuration. The ADCP should be deployed at the frontal interface. Drifter spacing are subject to change depending on size/orientation of the feature.

The drifters should be placed in two offset boxes on either side of the front. The 2 remaining drifters should be placed directly at the frontal interface (one being the ADCP drifter). The offset will increase the along-front distance of measurements. The spacing should be based on the transect spacing as discussed below, but with similar distances as in figure 6.3.

Other deployment methods include a straight line oriented in the across-front direction. This is devised for precise measurements of the frontal jet, but will yield poor results in terms of a

comprehensive measurement of the jet strength along the front and the background deformation field.

TIA/transects: The current method of orthogonal transects to the front should be repeated. Improvements can be made to have a more structured routine. This will be aided by the increased temporal resolution of the IR SST maps. Assuming a single vessel with a TIA, the vessel should make orthogonal transects of the front with maximal orthogonal displacements relative to the front of 1.3 km, but no less than 800 m. This will overlap the IR SST 2.6 km swath and the extent of the drifter domain. After applying the Gaussian filters which force the removal of 250 m of data from each end of the transect due to the filter width, there will be roughly 1.1 km of filtered data.

A single transect will take the vessel 11.4 minutes to travel 2.6 km at the current mean tow speed of 3.8 m s^{-1}. Accounting for a vessel turn (1-2 minutes) and 500 m (2.2 minutes) displacement down the front (parallel to the front), and entire "L-shaped" transect will take approximately 15 minutes. In this time, aircraft will have supplied the vessel with a new IR SST map to make an accurate second transect.

The rate of sampling has not increased, only the efficiency. The 500 m along-front travel should be based on the actual drifter spacing. If the drifter spacing in the along-front direction is small, then the vessel along-front displacement should be decreased proportionally to remain within the drifter field for the maximum possible duration.

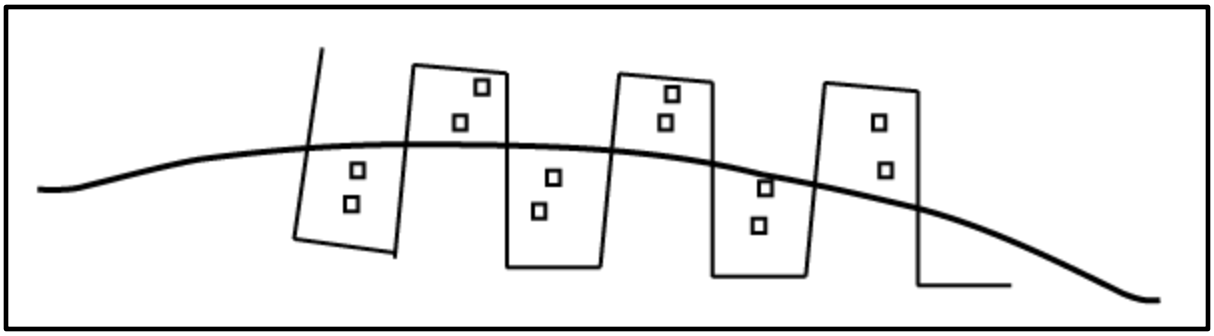

Figure 6.4: *In situ* "L shaped" transects. With proper coordination, the drifter field will be bounded by the IR SST and *in situ* data.

If the along-front drifter spacing is 1000 m, with the second grid being displaced by 500 m (relative to the opposing grid), then the along-front distance covered by drifters is 2.5 km. The vessel would require 5 "L shaped" transects to cover this distance in approximately 75 minutes. After completing the survey of the drifter domain, the vessel can either repeat the same procedure from the initial start location (except shifted for drifter movement), or retrace its track. This will result in 8-10 transects within a similar 2 hour period as the data analyzed in this report. Eight transects at 500 m along-front displacement will sample 20.8 orthogonal kilometers along 4 km (or 2 km if back and forth) of the front. Reducing the 500 m along-front displacement will increase the number of transects made and increase the spatial resolution within the drifter field at the cost of sampling less of the along-front distance. The goal here is to maximize the overlapping of the TIA measurements within the drifter field.

The vessel with the *TIA* should also be equipped with an ADCP to measure vertical velocity along the transects to compare with the 2D temperature/density fields. The TIA and ADCP data can then be used in conjunction to "calibrate" the measured, or calculated currents.

To supplement the *UCLA Zodiac in situ* measurements, the second research vessel deploying drifters (*Never Satisfied*) should be equipped with a surface temperature sampler (at minimum).

The surface sampler will passively record and significantly increase the spatial coverage of the surface temperature field without any additional resources. Ideally there would be a second TIA that could be deployed after the drifters were released, but this includes a significant increase in resources presently not in stock. The doubling of transects to be upwards of 15 would reduce the internal gravity waves by ≈ 75% and may be necessary if the above suggestions do not significantly reduce the internal gravity wave artifact in future deployments.

6.1.3 Communication

Communication throughout *SubEx* was excellent. The communication between the *UCLA Aircraft* and the *UCLA Zodiac* should be the basis for all communication –i.e. both marine radio and internet radio communications for voice transmission and real time data transfer (IR SST images). The second research vessel must have the same capabilities. The drifter deployment was hindered during *SubEx* because the *Never Satisfied* only received front position updates from the *UCLA Zodiac* by voice communication, not georeferenced maps.

As the communication network improves, a software package should be developed that parses all instrument outputs together and displays the data on a common graphical user interface (GUI). All scientists used some version of an in-house MATLAB program to record/plot data from the instruments during *SubEx*. The components of the infrastructure exist, but must be compiled.

This program can be installed on all computers used in *SubEx* and run passively in the background. The primary functions should be the uploading and downloading of data through the internet radio communication link to be visually displayed on a map with coordinate

information of all instruments and research platforms. The data can be transmitted through a series of network synced folders. The syncing must be automatic.

These recommendations will increase the efficiency of the experimental method. Since the data is contaminated by internal gravity waves, it is necessary to follow a more structured measurement technique that emphasizes the overlap of data in space and time at the expense of increasing the resolution of some measurements. The temporal resolution will be greatly enhanced, which is fundamental to reducing many of the large errors of the experiment due to interpolation and poor temporal evolution of the front.

I hope that my development of a usable infrastructure, data analysis, and recommendations presented here under the tutelage of Burkard Baschek and Jeroen Molemaker provide a strong platform to those that continue the research of *in situ* observations of submesoscale density features.

APPENDIX A

Transect *in situ* data. A) Interpolated 2D temperature field with black lines indicating instrument pressure (depth). The white line is the CTD depth. B) Temperature at 0.2 m and ≈ 10.3 m depth in black and blue respectively. Distance is a function of transect heading with 0 m indicating the point at which the vessel crosses the front. Negative values indicate the cold side of the front.

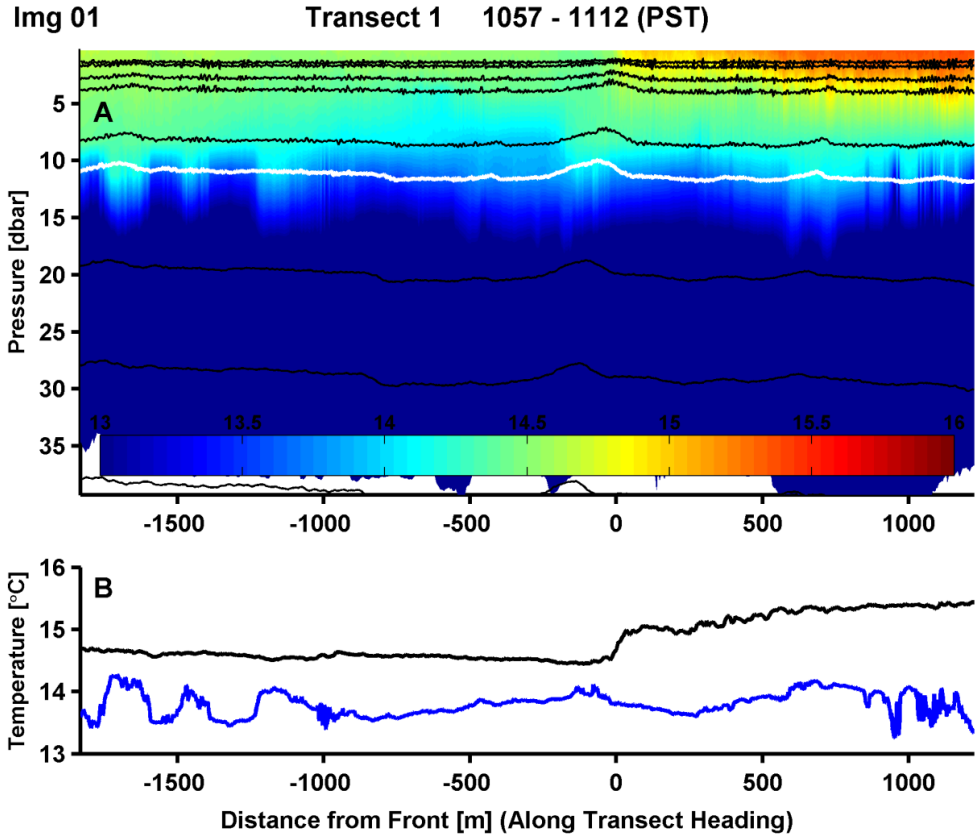

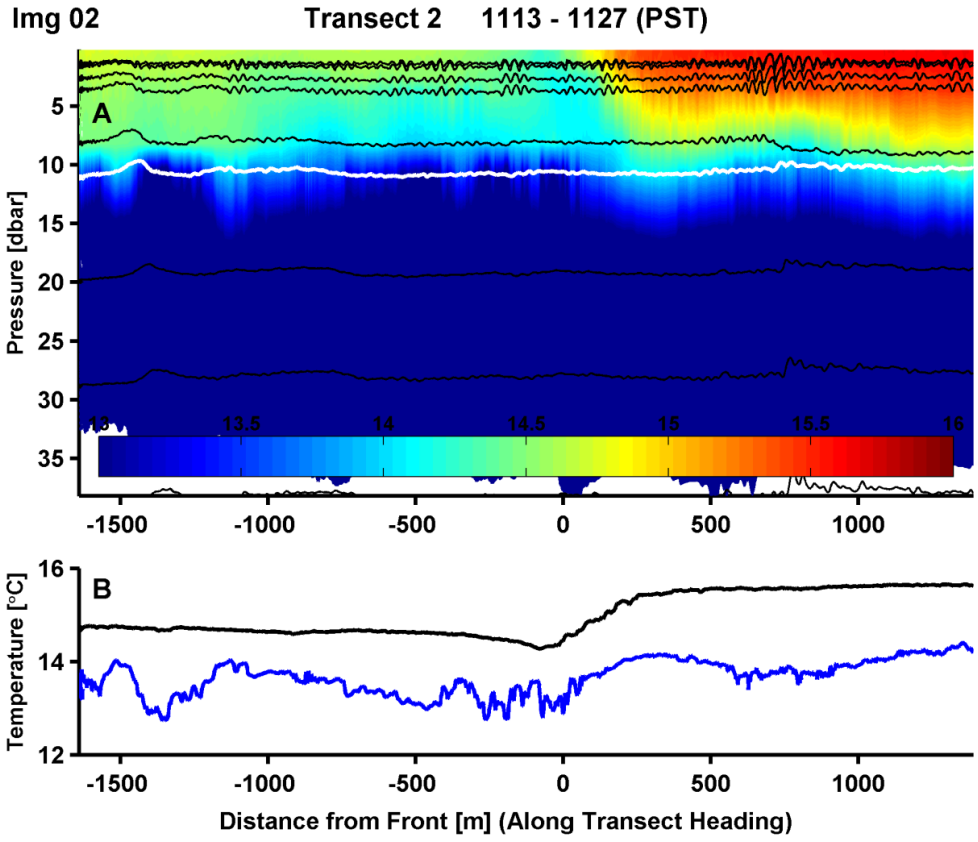
Img 02
Transect 2 1113 - 1127 (PST)
A
Pressure [dbar]
5
10
15
20
25
30
35
13
13.5
14
14.5
15
15.5
16
-1500
-1000
-500
0
500
1000
B
Temperature [°C]
16
14
12
-1500
-1000
-500
0
500
1000
Distance from Front [m] (Along Transect Heading)

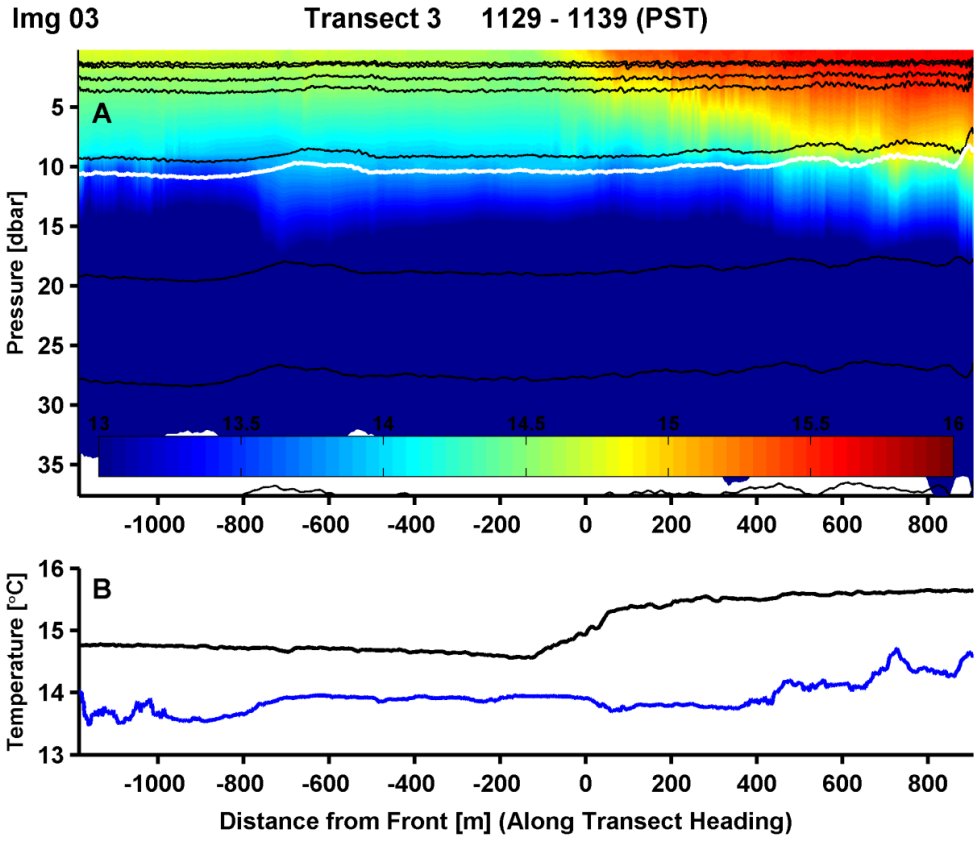
Img 03
Transect 3 1129 - 1139 (PST)
A
Pressure [dbar]
5
10
15
20
25
30
35
13
13.5
14
14.5
15
15.5
16
-1000
-800
-600
-400
-200
0
200
400
600
800
B
Temperature [°C]
16
15
14
13
-1000
-800
-600
-400
-200
0
200
400
600
800
Distance from Front [m] (Along Transect Heading)

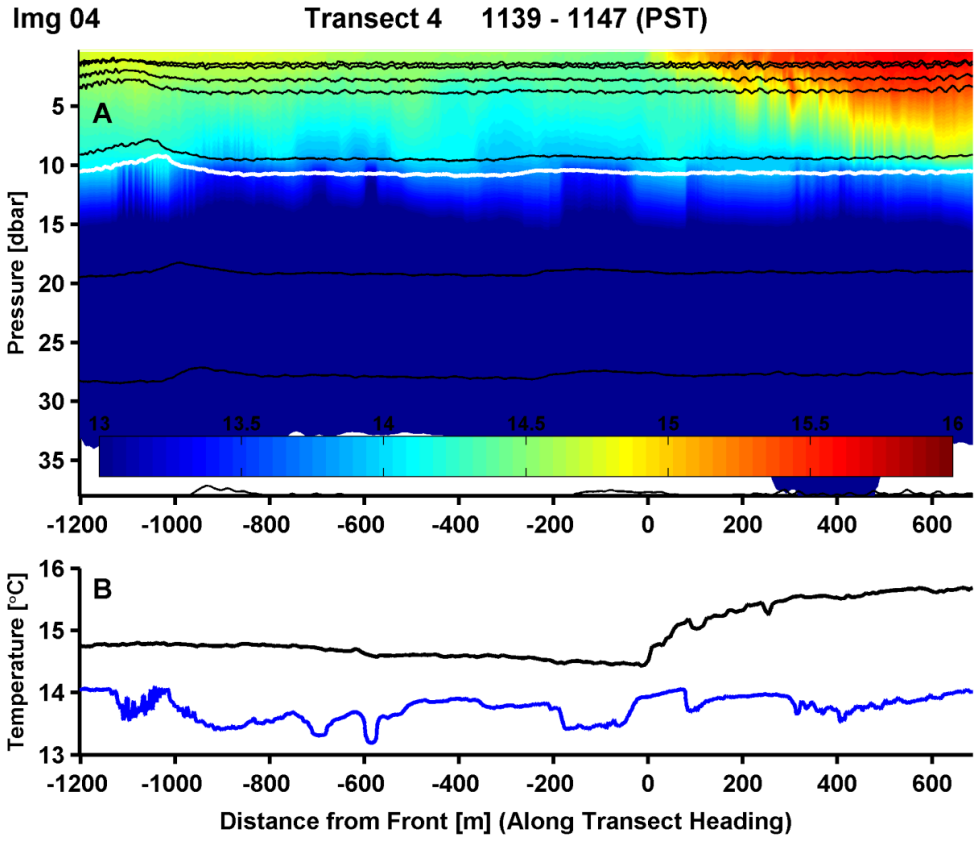
Img 04
Transect 4 1139 - 1147 (PST)
A
B
Pressure [dbar]
Temperature [°C]
Distance from Front [m] (Along Transect Heading)

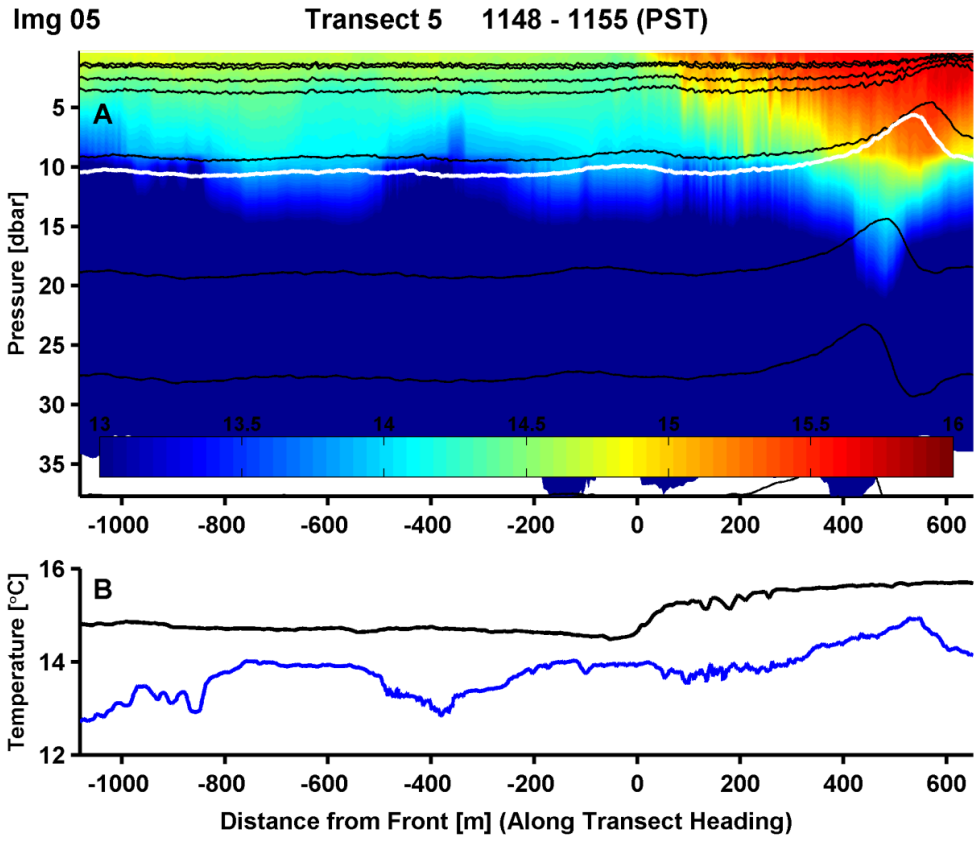
Img 05
Transect 5 1148 - 1155 (PST)
A
B
Pressure [dbar]
Temperature [°C]
Distance from Front [m] (Along Transect Heading)

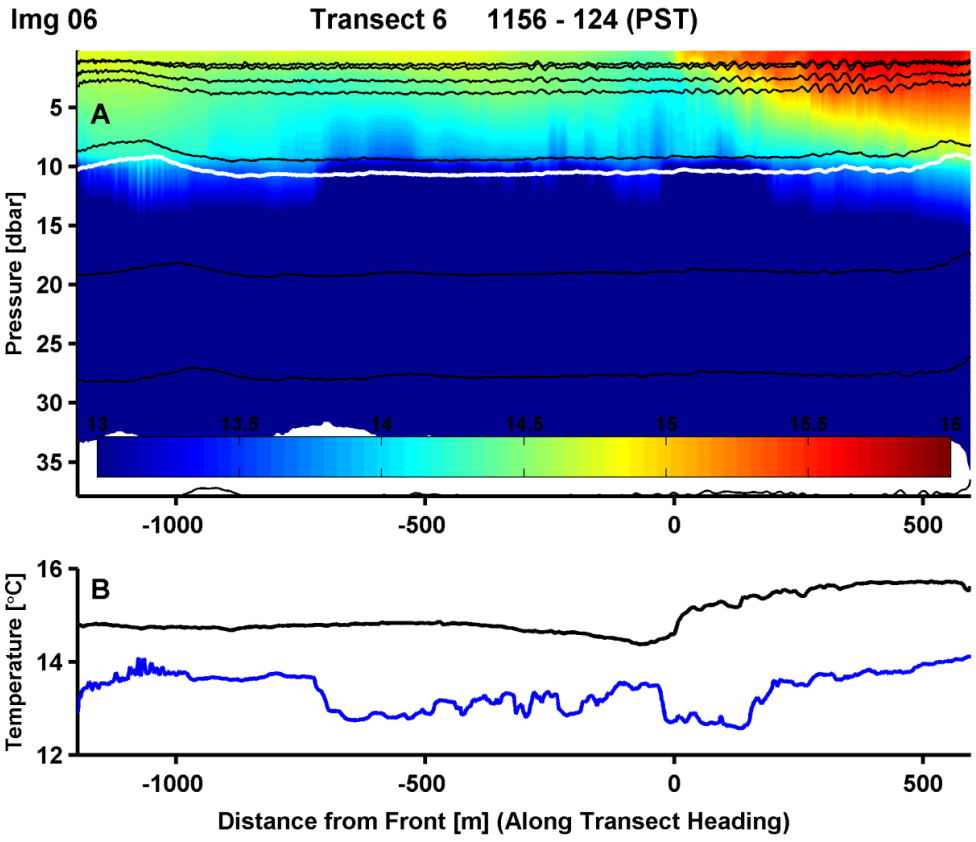
Img 06
Transect 6 1156 - 124 (PST)
A
B
Pressure [dbar]
Temperature [°C]
Distance from Front [m] (Along Transect Heading)

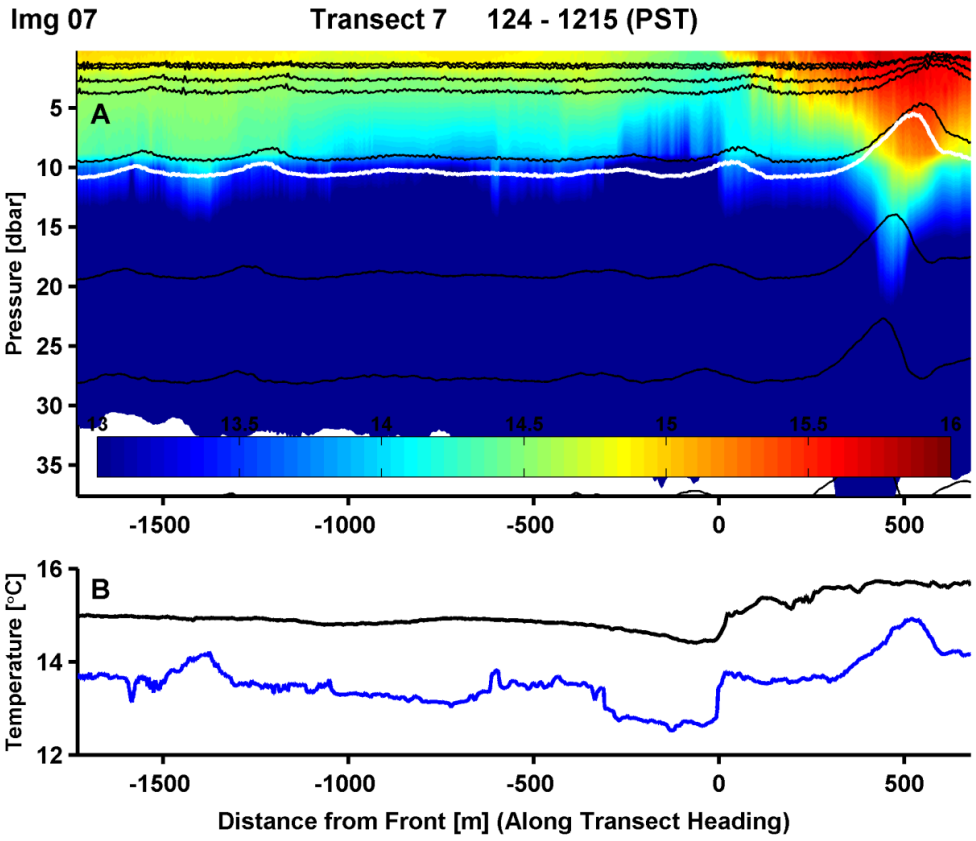
Img 07
Transect 7 124 - 1215 (PST)
A
B
Pressure [dbar]
Temperature [°C]
Distance from Front [m] (Along Transect Heading)

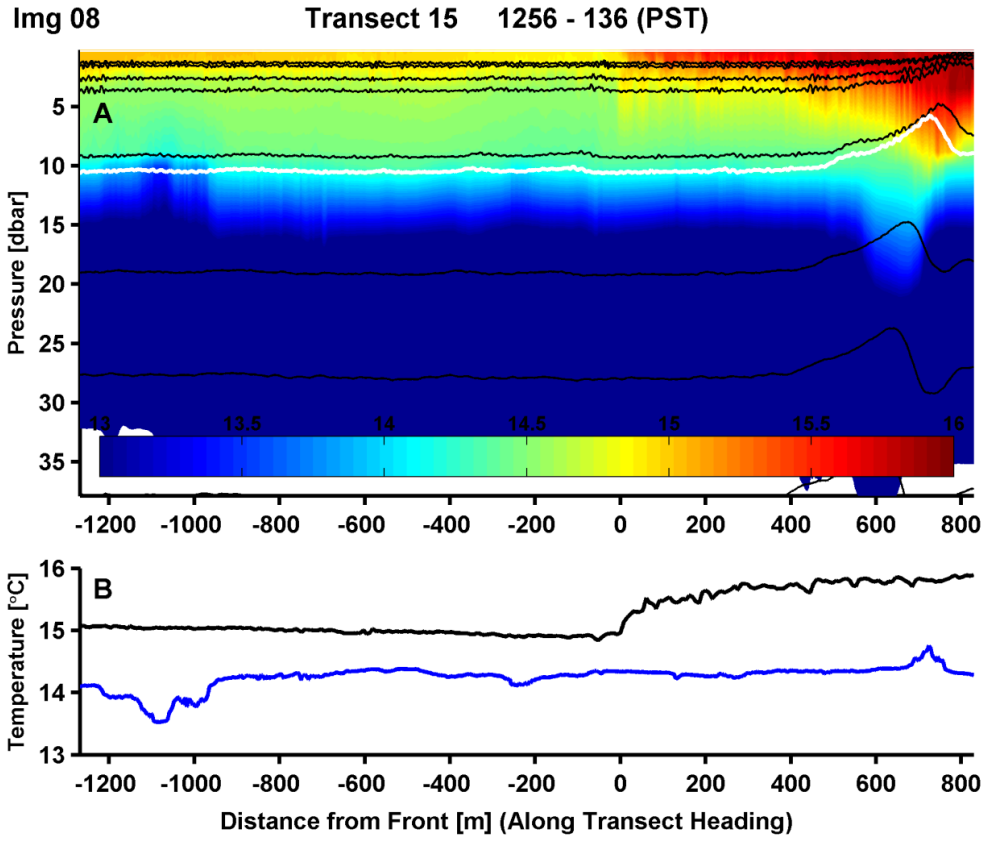
Img 08
Transect 15 1256 - 136 (PST)
A
B
Pressure [dbar]
Temperature [°C]
Distance from Front [m] (Along Transect Heading)

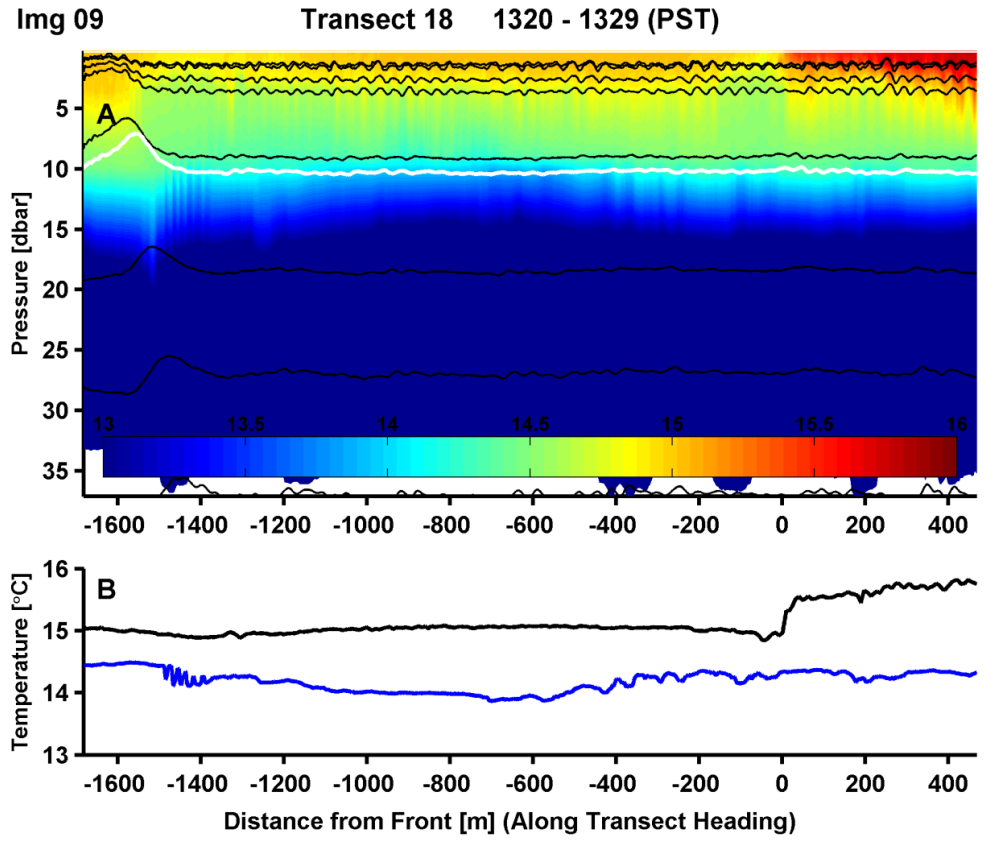
Img 09
Transect 18 1320 - 1329 (PST)
A
B
Pressure [dbar]
Temperature [°C]
Distance from Front [m] (Along Transect Heading)

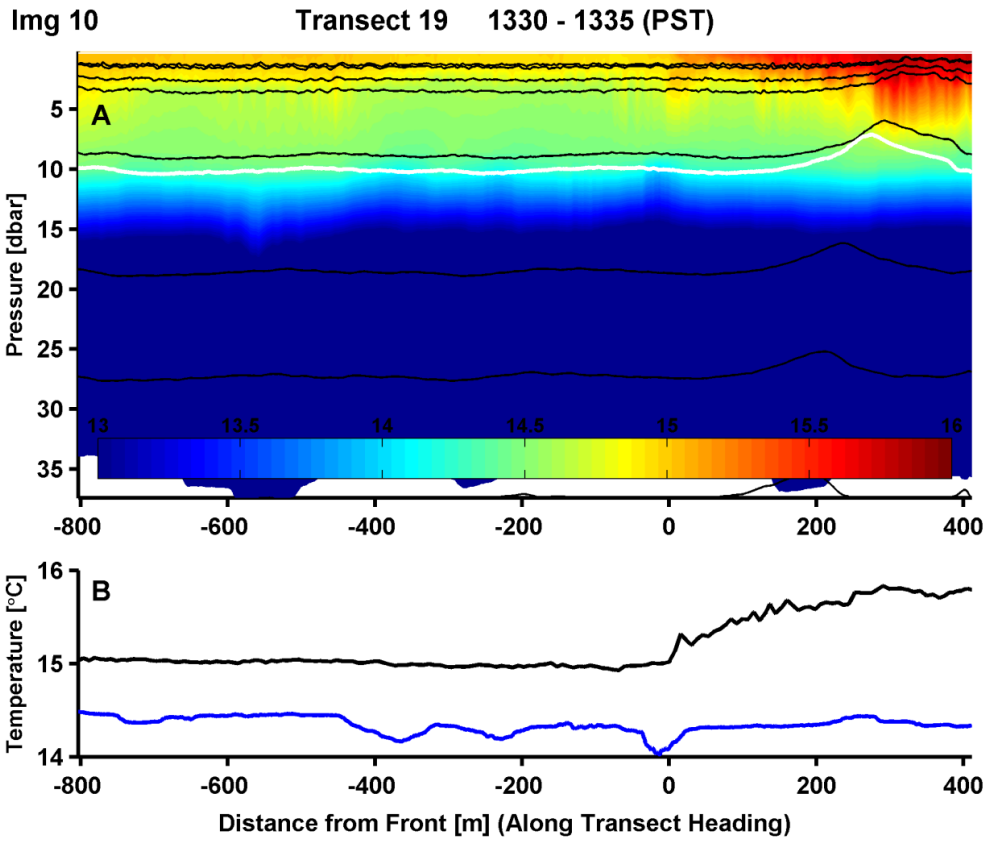
Img 10
Transect 19 1330 - 1335 (PST)
A
B
Pressure [dbar]
Temperature [°C]
Distance from Front [m] (Along Transect Heading)

APPENDIX B

A) Time constrained *in situ* transects overlaid on IR SST image. B) Dashed lines are *in situ* temperature and solid lines are IR SST. The line colors are consistent between image A and B.

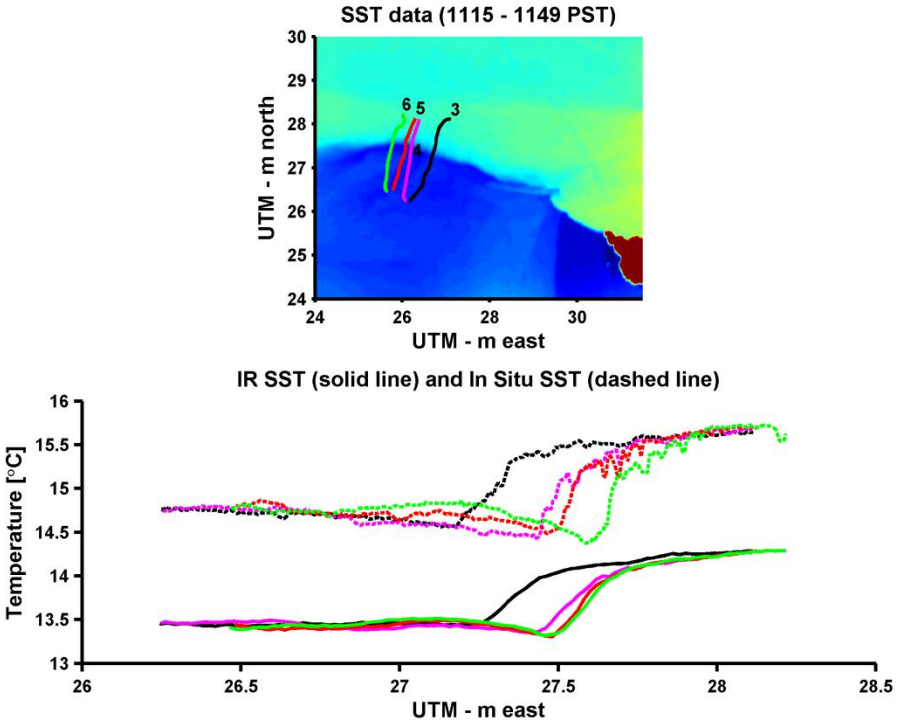

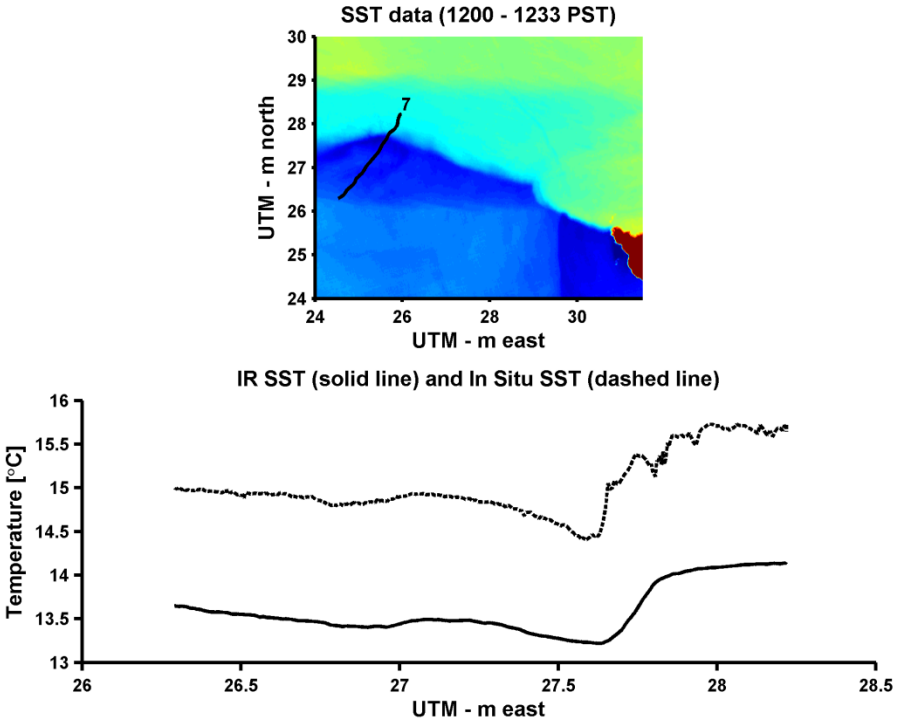
SST data (1200 - 1233 PST)
UTM - m north
UTM - m east
7
IR SST (solid line) and In Situ SST (dashed line)
Temperature [°C]
UTM - m east

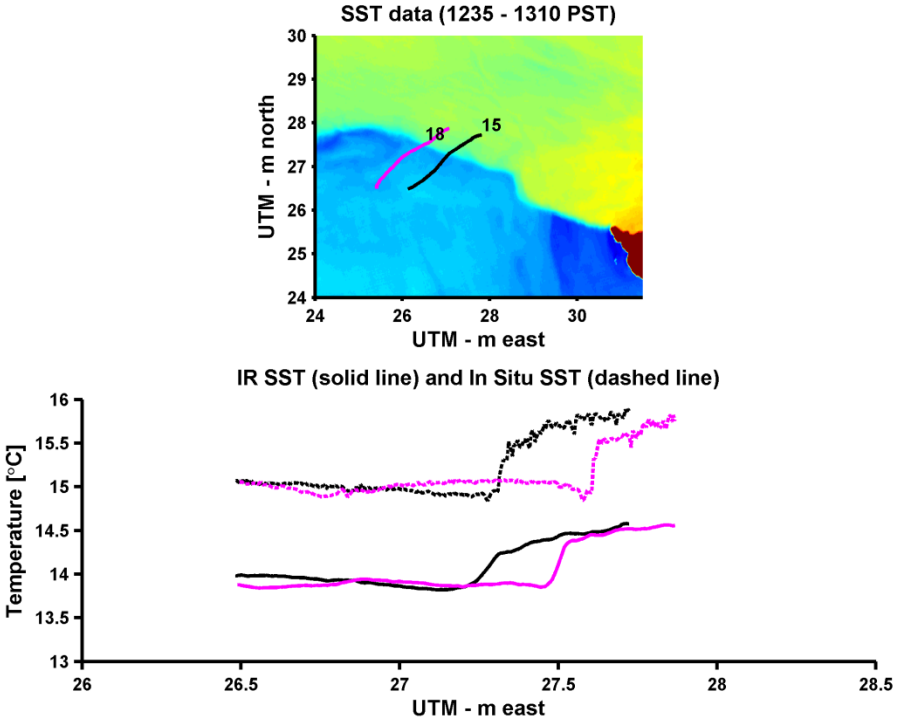
SST data (1235 - 1310 PST)
UTM - m north
UTM - m east
18
15
IR SST (solid line) and In Situ SST (dashed line)
Temperature [°C]
UTM - m east

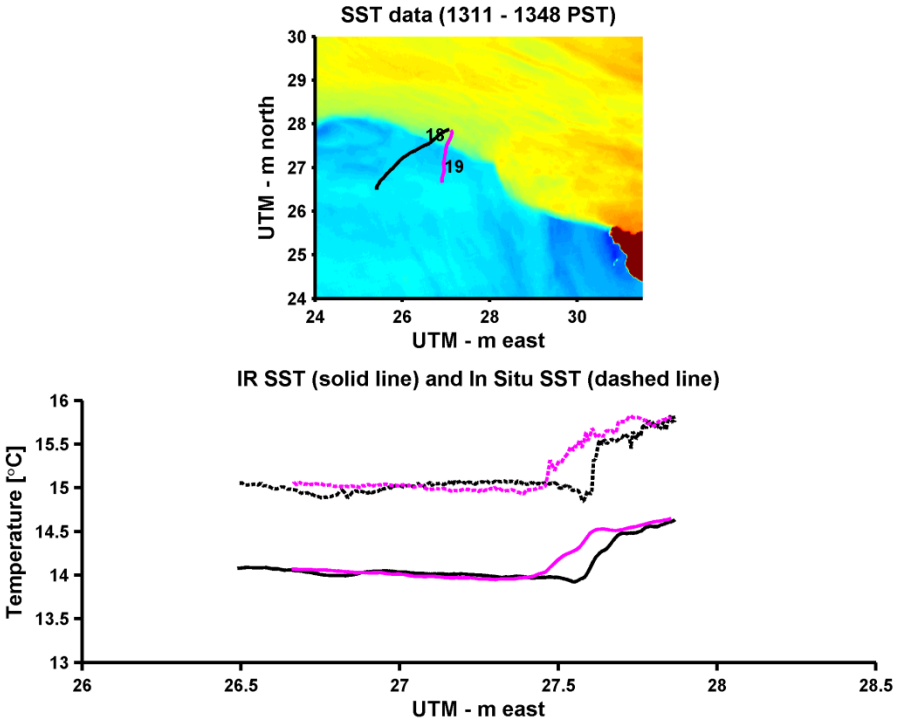
SST data (1311 - 1348 PST)
UTM - m north
UTM - m east
18
19
IR SST (solid line) and In Situ SST (dashed line)
Temperature [°C]
UTM - m east

APPENDIX C

Cold side bias - Drifter position and IR SST image have the same times. The IR SST raw images mosaiced outside of the drifter domain are provided to complete the image, but they are at different times. In image 1 the drifters are just deployed and approaching the front. Image 3 is the first instance of the cold side bias of all three drifters near the front.

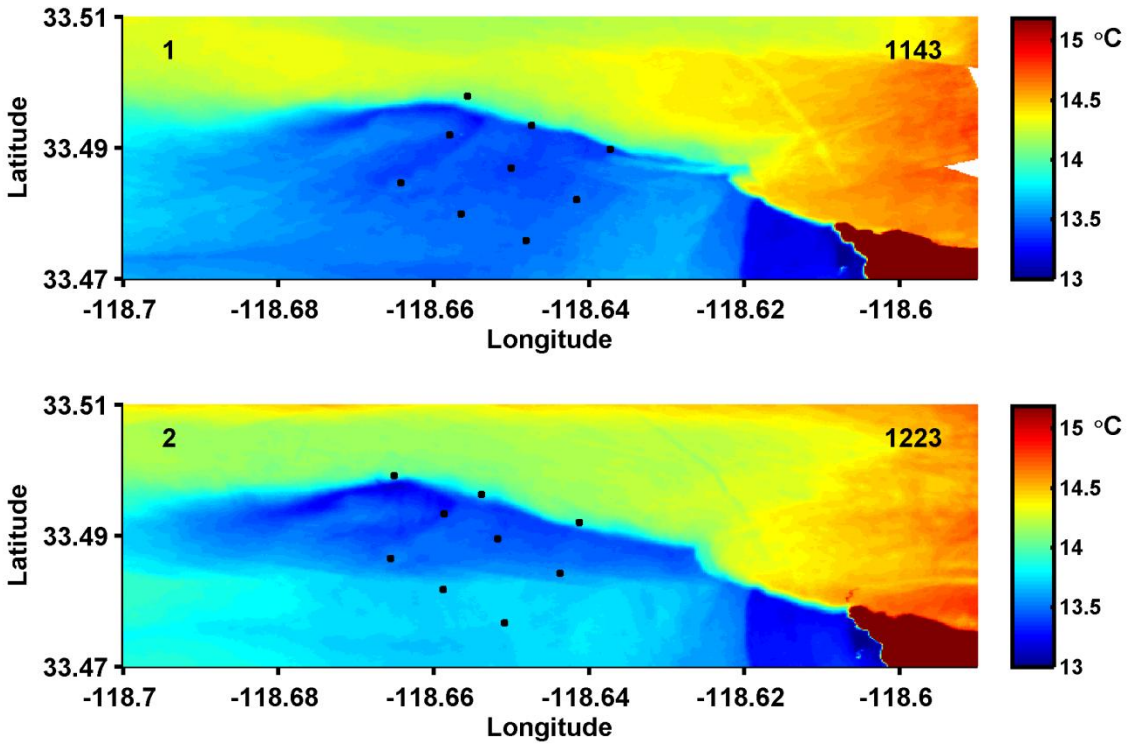

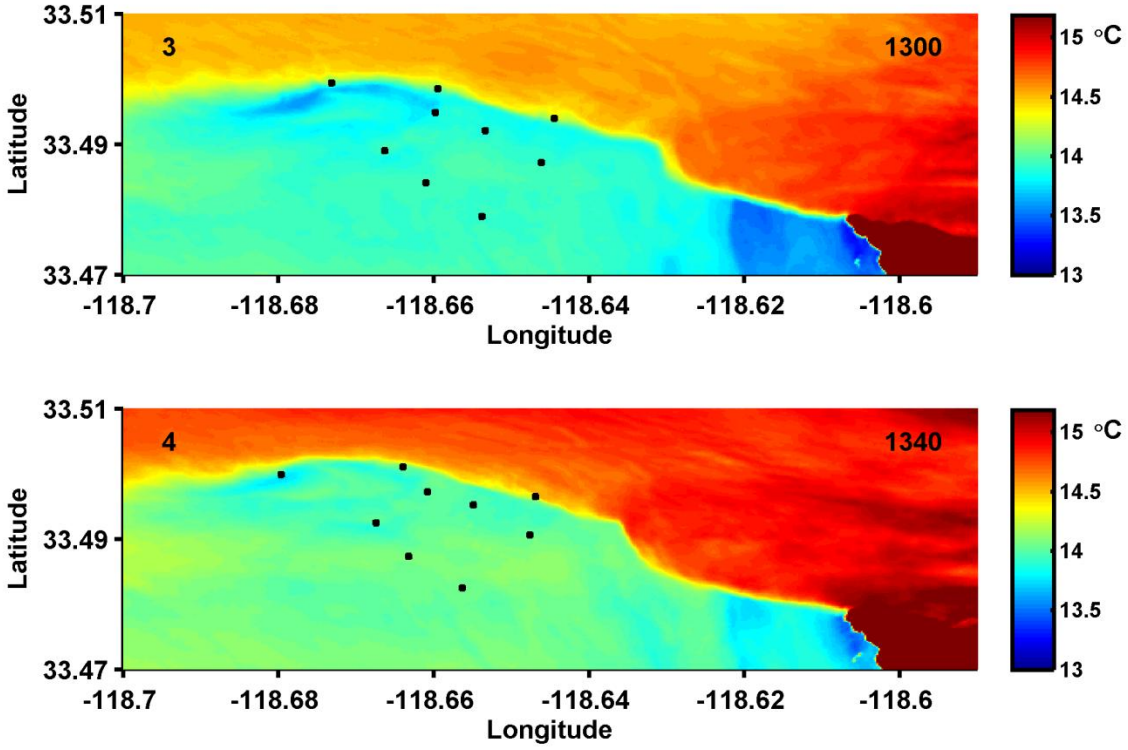
3
1300
4
1340
33.51
33.49
33.47
Latitude
-118.7
-118.68
-118.66
-118.64
-118.62
-118.6
Longitude
15 °C
14.5
14
13.5
13

REFERENCES

Bleck, R., Onken, R., and Woods, J.D. 1988. A two-dimensional model of mesoscale frontogenesis in the ocean. *Quart. J. Roy. Meteor. Soc.* 114: 347–371.

Capet, X., Klein, P., Bach, L.H., Lapeyre, G., and McWilliams, J.C. 2008. Surface kinetic energy transfer in surface quasi-geostrophic flows. *J. Fluid Mech*. 604: 165–174.

Capet, X., McWilliams, J.C., Molemaker, M., and Shchepetkin, A. 2008a. Mesoscale to submesoscale transition in the California current system. Part 1: Flow structure, eddy flux and observational tests. *J. Phys. Oceanogr.* 38: 29–43.

Capet, X., McWilliams, J.C., Molemaker, M., and Shchepetkin, A. 2008b. Mesoscale to submesoscale transition in the California current system. Part II: Frontal processes. *J. Phys. Oceanogr*. 38: 44–69.

Capet, X., McWilliams, J.C., Molemaker, M., and Shchepetkin, A. 2008c. Mesoscale to submesoscale transition in the California current system. Part III: Energy balance and flux. *J. Phys. Oceanogr*. 38: 2256–2269.

Charney, J. 1971. Geostrophic Turbulence. *J. Atmos. Sci*. 28: 1087–1095.

Defant, A. 1950. Reality and illusion in oceanographic survey. *J. Marine Res*. 9: 120-138

DiGiacomo, P., and Holt, B. 2001. Satellite observations of small coastal ocean eddies in the Southern California Bight. *J. Geophys. Res.* 106: 521–544.

Fedorov, K. 1987. *The Physical Nature and Structure of Ocean Fronts*. Springer-Verlag, NY.

Glover, D., Doney, S., Nelson, N., and Wallis, A. 2008. *Submesoscale anisotropy (fronts, eddies, and filaments) as observed near Bermuda with ocean color data*. Presented at Ocean Sci. Meet. Orlando. 03-04-2008.

Haine, T.W., and Marshall, J. 1998. Gravitational, symmetric, and baroclinic instability of the ocean mixed layer. *J. Phys. Oceanogr*. 28:634-58.

Hickey, B.M. 1992. Circulation over the Santa Monica-San Pedro Basin and shelf. *Progress in Oceanography*. 30:37-115.

Holt, B. 2004. SAR imaging of the ocean surface. In *Synthetic Aperture Radar (SAR) Marine User's Manual*. edited by Jackson, C.R., and Apel, J.R. NOAA NESDIS Office of Research and Applications. Washington DC. pp. 25-79.

Hoskins, B.J. 1975. The geostrophic momentum approximation and the semi-geostrophic equations. *J. Atmos. Sci*. 32: 233-242.

Hoskins, B.J. 1982. The mathematical theory of frontogenesis. *Annu. Rev. Fluid Mech*. 14: 131–151.

Hoskins, B.J., and Bretherton, F.P. 1972. Atmospheric frontogenesis models: Mathematical formulation and solution. *J. Atmos. Sci.* 29: 11–37.

Hautala, S., Thompson, L., and Kelly, K. 2005. University of Washington Ocean 420 Class Notes: *Internal Gravity Waves*. Accessed 1 November 2012. <http://faculty.washington.edu/luanne/pages/ocean420/>.

Klein, P., Hua, BL., Lapeyre, G., Capet, X., Le Gentil, S., and Sasaki, H. 2008. Upper ocean turbulence from high 3-D resolution simulations. *J. Phys. Oceanogr.* 38:1748–63.

Klein, P., and Lapeyre, G. 2009. The oceanic vertical pump induced by mesoscale and submesoscale turbulence. *Annu. Rev. Mar. Sci*. 1: 351-375.

Lapeyre, G., and Klein, P. 2006a. Dynamics of the upper oceanic layers in terms of surface quasigeostrophy theory. *J. Phys. Oceanogr.* 36: 165–76.

Lapeyre, G., and Klein, P. 2006b. Impact of the small-scale elongated filaments on the oceanic vertical pump. *J. Mar. Res.* 64: 835–51.

Le Traon, PY., Klein, P., Hua, B., and Dibarboure, G. 2008. Do altimeter wavenumber spectra agree with the interior or surface quasi-geostrophic theory? *J Phys. Oceanogr*. 38: 1137-42.

Lévy, M., Klein, P., and Tréguier, A.M. 2001. Impact of submesoscale physics on production and subduction of phytoplankton in an oligotrophic regime. *J. Mar. Res.* 59:535–65.

Mahadevan, A., and Archer, D. 2000. Modeling the impact of fronts and mesoscale circulation on the nutrient supply and biogeochemistry of the upper ocean. *J. Geophys. Res*. 105 (C1): 1209-1225.

Mahadevan, A., and Tandon, A. 2006. An analysis of mechanisms for submesoscale vertical motion at ocean fronts. *Ocean Modelling*. 14: 241–256.

Marmorino, G., Holt, B., Molemaker, M., DiGiacomo, P., and Sletten, M. 2010. Airborne synthetic aperture radar observations of 'spiral eddy' slick patterns in the Southern California Bight, *J. Geophys. Res. Oceans*. 115: C05010

McGillicuddy, D., Anderson, L., Bates, N., Bibby, T., Buesseler, KO., et al. 2007. Eddy/wind interactions stimulate extraordinary mid-ocean plankton blooms. *Science*. 316:1021-1026.

McGillicuddy, D., Anderson, L., Doney, S., and Maltrud, M.E. 2003. Eddy-driven sources and sinks of nutrients in the upper ocean: result from a 0.1° resolution model of the North Atlantic. *Glob. Geochem. Cycles* 17:1035.

McWilliams, J.C. 2006. *Geophysical Fluid Dynamics: Fundamentals*. Cambridge, UK: Cambridge Univ. Press. 249 pp.

McWilliams, J.C. 2010. A perspective on submesoscale geophysical turbulence. *IUTAM Symposium on Turbulence in the Atmosphere and Oceans*. 28: 131-141.

McWilliams, J.C. and Molemaker, M. 2004. Ageostrophic anticyclonic instability of a geostrophic barotropic boundary current. Phys. Fluids. 16: 3720-3725

Muller, P., McWilliams, J.C., and Molemaker, M. 2005. Routes to dissipation in the ocean: the 2d/3d turbulence conundrum. *In Marine Turbulence: Theories, Observations and Models* (ed. H. Baumert, J. Simpson & J. Sundermann). Cambridge University Press. pp. 397–405.

Nagai, T., Tandon, A., and Rudnick, D.L. 2006. Two-dimensional ageostrophic secondary circulation at ocean fronts due to vertical mixing and large-scale deformation. *J. Geophys. Res*. 111: C09038. Doi:10.1029/2005JC002964

National Aeronautics and Space Administration. *Near Real Time (Orbit Swath) Images*. Accessed 1 December 2012.<http://rapidfire.sci.gsfc.nasa.gov/cgi-bin/imagery/realtime.cgi>.

Niiler, P.P., Sybrandy, A.S., Bi, K.N., Poulain, P.M. and Bitterman, D. 1995. Measurements of the water-following capability of the holey-sock and tri-star drifters. *Deep-Sea Res*. 42: 1951-1960.

Ohlmann, J.C., and Sybrandy, A.L. 2002 A catch-and-release Lagrangian drifter for near-shore ocean circulation research. *Proceedings, California and the World Ocean* (in press).

Ohlmann, J.C., White, P.F., Sybrandy, A.L., and Niiler, P.P. 2005. GPS-cellular technology for coastal ocean observing systems. *J. Atmos and Oceanic Tech*. 22: 1381:1388.

Pedlosky, J. 1987. *Geophysical Fluid Dynamics*. New York: Springer-Verlag. 728 pp.

Pollard, R.T. and Regier, L.A. 1990. Large variations in potential vorticity at small spatial scales in the upper ocean. *Nature*. 348: 227-29.

Pollard, R.T. and Regier, L.A. 1992. Vorticity and vertical circulation at an ocean front. *J Phys. Oceanogr*. 22: 609-625.

Thomas, L.N., Tandon, A., and Mahadevan, A. 2007. Submesoscale processes and dynamics. *Ocean Modeling in an Eddying Regime. Geophys. Monograph Series 177*. 10.1029/177GM05.

Tomczak, M., and Godfrey, J.S. 2003. *Regional Oceanography: an Introduction*. Delhi: Daya. 390 pp.

Southern California Coastal Ocean Observing System. 2012. *Data, products, and modeling*. Accessed 1 April 2011. <http://www.sccoos.org>.

Spall, M. 1995. Frontogenesis, subduction, and cross-front exchange at upper ocean fronts. *J. Geophys. Res*. 100: 2543– 2557.

Stewart, R. 2008. *Introduction to Physical Oceanography*. Accessed 1 August 2012. <http://oceanworld.tamu.edu/resources/ocng_textbook/conttents.html>

Veron, F., Melville, W.K., and Lenain, L. 2008. Infrared techniques for measuring ocean surface processes. *American Meteorological Soc*. 25: 307-326.

Wang, D.P. 1993. Model of frontogenesis: subduction and upwelling. *J. of Marine Res*. 51: 497-513.

Wolfram Research. *Experimental Data Analyst Documentation*. Accessed 21 November 2012. <http://reference.wolfram.com/applications/eda/ExperimentalErrorsAndErrorAnalysis.html>.